DEVELOPMENT OF A HEMODYNAMIC SIMULATION MODEL FOR ASSISTING LIVER TRANSARTERIAL EMBOLOTHERAPY

A DISSERTATION
SUBMITTED TO THE FACULTY OF
UNIVERSITY OF MINNESOTA
BY

JINGYING LIN

IN PARTIAL FULFILLMENT OF THE REQUIREMENTS
FOR THE DEGREE OF
DOCTOR OF PHILOSOPHY

ADVISORS: JAFAR GOLZARIAN, E. RUSSELL RITENOUR

JUNE 2020

Acknowledgements

I would like to express my sincere gratitude to my advisors Dr. Jafar Golzarian and Dr. E. Russell Ritenour for their patience and invaluable instruction.

I would like to thank the rest of my thesis committee, Dr. Bruce Gerbi and Dr. John Broadhurst, for their insightful comments.

I appreciate the Allied Scientist Training Grant from Society of Interventional Radiology Foundation that enabled the animal experiments to be conducted.

My sincere thanks also go to Dr. Sanjay Gupta and his lab at MD Anderson Cancer Center where the cancerous animal models were built.

I thank Laura Pook at NAMSA, Amanda Talan and Joanne Johnson at Imaging Center for the animal experiments and micro-CT acquisition.

I thank all my amazing friends for their countless encouragements.

I would like to thank my parents for their constant support and unconditional love. My special thanks go to my younger cousin for her spiritual support.

Dedication

To my parents, who encourage me to dream big and never give up.

Abstract

Embolotherapy is an effective interventional therapy for patients with intermediate-stage hepatocellular carcinoma. Taking advantage of hypervascular characteristics from hepatocellular carcinoma, the embolic agents injected into hepatic arteries via a catheter block the tumor-feeding arteries. The degree of targeted embolization depends on how successfully the embolic agents are transported to the tumor-feeding arteries and lodged near the tumors. In addition, being able to minimize and detect non-targeted embolization is also a major concern for radiologists. Due to limitations on the ability to monitor blood dynamics, the influence of local hemodynamics near a tumor during embolization is not well understood. Since blood flow is the only propulsive force on the embolic agents after they are released into the hepatic arteries, hemodynamic changes caused by the interaction between embolic agents and blood flow is crucial to the success of embolotherapy. Understanding the hemodynamic effects of various factors and how they interact is the key to linking this complex situation to treatment outcomes and could assist radiologists in improving their practice.

So far, the factors that influence the hemodynamics have been investigated through pre-clinical experiments and clinical case studies, such as catheter placement, and microsphere characteristics (size, quantity, and type), catheter type, microsphere injection techniques (injection timing, velocity, and interval). Utilizing computational analysis and simulation on particle-hemodynamics inside hepatic vascular models has

been an effective preclinical approach to investigate the interaction among hemodynamic factors. One of the key components for reliable hemodynamic simulation is a geometric domain in which physiological boundary conditions can be applied to match the simulation-specified flow conditions. A geometric domain - also called geometric configuration, computational domain, or mathematical model - is defined as a three-dimensional (3D) vascular geometry. Currently, hepatic vascular geometries used for studying computational hemodynamic simulation are rare, have limited or truncated vasculature, and often lack the vasculature that microspheres are targeting. Existing imaging technology cannot provide a process for transmitting emboli. However, visualization of emboli transmission can be achieved through simulation models. In this dissertation, a set of procedures was developed to construct a visualized embolization simulation model based on detailed and coherent anatomic vascular structures.

Aiming at the limitations of the existing vascular models, we built a vascular network model based on a real vascular structure with details and continuity to form the geometric domain necessary for the simulation model. First, tissue samples filled with contrast were established by selecting a commonly used preclinical animal model to ensure faithful vascular structure, and the samples were processed to meet the requirements of a detailed and coherent vascular network. Due to limitations of the imaging system, multi-resolution micro-CT images were used to model the microvasculature by modeling the vasculature in each individual liver lobe and registering them back to the entire liver to achieve fidelity and detailed spatial

vasculature under physiological conditions. Finally, the vascular modeling method, including vascular segmentation and vascular centerline extraction, was used to automatically generate the vascular network.

The ability of an imaging system to faithfully reproduce an image of an object is described by the modulation transfer function (MTF). The MTF of an imaging system is a measure of how well sine waves of various frequencies that describe the spatial distribution transmission of X- rays through an object are represented faithfully in the image. An ideal MTF is a horizontal straight line, which means that no matter how an object's size varies, the imaging system would modulate and deliver a faithful profile of the object onto the image. However, the MTF of the micro-CT scanner reflects a Gaussian blurring function. This blurring function convolves with the object's true cross-sectional profile, resulting in the blurred output: as the object becomes smaller, the intensity peak of the object is reduced significantly, with a broadened full width at half maximum (FWHM). In our reconstructed vascular model, the over-estimation of radii on smaller vessels was corrected by the Gaussian correction function. To evaluate the accuracy of the correction, registration of partial microvasculature from higher-resolution micro-CT to the individual lobes were studied to quantify the comparison of the vessel segment radius between the corrected size and the measurements from high resolution images.

Because liver tumors have hypervascularity features, modeling the cancerous vasculature is particularly important. The purpose of this study is to investigate the

feasibility of modeling the vascular network for a tumor vascular model that can be used for blood flow simulation to aid embolization.

To visualize the real-time trajectories of embolic agents as they are transported inside arteries, a computer model based upon micro-CT images of hepatic microvasculature in a rabbit was constructed. Under the effect of simulated blood flow, a particle-based simulation model that provides embolic agents' transportation within the constructed model was then developed. In the final model, the simulated transmission of emboli is visualized by a web-based application. This application can be used not only to directly visualize the transmission of emboli but also to analyze hemodynamics in different situations, providing a reference for actual clinical operations. The work presented here is intended to provide a basis for building visual simulation models for individual human patient's unique vascular structures at some point in the future.

Table of Contents

Acknowledgements i

Dedication ii

Abstract iii

List of Tables vii

List of Figures vii

CHAPTER 1 INTRODUCTION 1

1 Liver Cancer 1
2 Embolotherapy for Liver Cancer 4
3 Hemodynamic Impact Factors during the Transarterial Procedure 6
3.1 Effects of Flow Dynamics under Non-targeting 7
3.2 Prophylactic Embolization 8
3.3 Flow-controlled Catheters 8
3.4 Particulate Embolic Agents 14
3.5 Direct Intraprocedural Imaging Monitoring 19
4 Indirect Hemodynamic Studies 23
4.1 Pre-evaluation on Flow Distribution 23
4.2 Values on Images 24
5 Clinical Concern and Gaps 25
6 Specific Aims 26
7 Outline of the Thesis 28

CHAPTER 2 ANIMAL EXPERIMENTS AND MICRO-CT ACQUISITIONS 30

1 Background 30
2 Materials and Methods 32
2.1 Normal Liver Model 32
2.2 VX2 Rabbit Liver Model 35

3 Results 38
4 Discussion 46
CHAPTER 3 THREE-DIMENSIONAL MODELING OF HEPATIC MICROVASCULATURE NETWORK BASED ON MICRO-CT IMAGES 49
1 Background 49
2 Materials and Methods 53
2.1 Segmentation 54
2.2 Center Point Extraction 56
3 Results 60
4 Discussion 69
CHAPTER 4 ACCURACY ANALYSIS OF RECONSTRUCTED MICROVASCULATURE 75
1 Background 75
2 Materials and Methods 76
2.1 Vessel Registration among Multi-resolution Micro-CT Volumes 77
2.2 Paired Center Points' Radius Measurements 78
2.3 Gaussian Blurring Correction 78
2.4 Correction Validation under Multi-resolution Micro-CT Volumes 79
2.5 Quantitative Comparison on Dimension Accuracy 79
3 Results 80
4 Discussion 93
CHAPTER 5 HEPATIC TUMOR MICROVASCULATURE 97
1 Background 97
2 Materials and Methods 98
2.1 VX2 Liver Sample and Micro-CT Acquisition 98
2.2 3D Modeling 98
2.3 3D Volume Rendering 98

3 Results 100
4 Discussion 103
CHAPTER 6 VISUALIZATION MODEL OF EMBOLIZATION SIMULATION 105
1 Background 105
2 Methods 106
2.1 Boundaries of Vascular Model 106
2.2 Microsphere Modeling 107
2.3 Particle-based Simulation 107
3 Results 109
4 Discussion 113
CHAPTER 7 CONCLUSION 116
REFERENCES 118
APPENDIX A PREPARATION OF TUMOR FOR FROZEN STORAGE 133
APPENDIX B PREPARATION OF TUMOR INOCULATION FROM FROZEN STOCK 134
APPENDIX C PREPARATION OF TUMOR INOCULATION 137

List of Tables

Table 1. Summary of the characteristics of current embolic particles in the market used for TAE, TACE and DEB-TACE 16

Table 2. Summary of the characteristics of current embolic particles in the market used for TARE 18

Table 3. Summary of sample size, micro-CT resolution and data size..... 94

Table 4. Summary of two VX2 tumor capsules on mass volume, feeding arterioles and their size 101

List of Figures

Figure 1. Hemodynamic changes during multistep hepatocarcinogenesis 3

Figure 2. Schematic flow while injecting under various types of microcatheters 11

Figure 3. Schematic diagram of blood flow at catheter downstream 12

Figure 4. An illustration of liver perfusion set-up 34

Figure 5. The surface appearance of a liver while perfused by Microfil® 39

Figure 6. Demonstration of the harvested liver samples..... 39

Figure 7. Illustration of the lobe's dissection plan for tiered resolution micro-CT scans 40

Figure 8. Illustration of the dissection plan on the individual lobe for high resolution micro-CT scans 40

Figure 9. 3D volume visualization of three liver samples. 41

Figure 10. Maximum intensity projection views on the entire liver sample from 195 μm micro-CT images and on left and right individual lobes from 57.6 μm micro-CT images 42

Figure 11. The VX2 liver surface appearance during Microfil® perfusion 44

Figure 12. A collection of 3D volume rendered views on local tumor microvasculature 45

Figure 13. Microfil® working time plots on the volume percentage of MV-Curing Agent in the mixture 48

Figure 14. Flowchart of the development processes of the vascular model 59

Figure 15. Illustration of the proposed adaptive segmentation. 62

Figure 16. Illustration of the distance-to-boundary function and the wave time function 63

Figure 17. Illustration of the extracted centerlines superimposed on the MIP views from micro-CT volume 64

Figure 18. Intensity plots of the extracted center points and the corresponding radii in pixels 65

Figure 19. Illustration on registration of left and right lobes to the whole liver 66

Figure 20. 3D vascular reconstruction based on the centerlines from Figure 17 using a unit radius 67

Figure 21. Visualization of the reconstructed subtrees with detailed structure in a unit radius for display 67

Figure 22. Color mapping on the extracted vessel radii superimposed on the MIP view of the liver lobes. 68

Figure 23. Plots of vessel cross-section profile with the decreased peak intensities as the vessel size decreases 76

Figure 24. Schematic diagram of vessel registration among multi-resolution micro-CT volumes 77

Figure 25. The probability plots of vessel radii extracted from 195.8 μm and 57.6 μm resolution micro-CT images. 80

Figure 26. Radii comparison between segmentation and FWHM from 57.6 μm micro-CT images 82

Figure 27. Bland-Altman comparison on the radii derived from segmentation and FWHM 82

Figure 28. Radii comparison between segmentation and FWHM from 57.6 μm micro-CT images on vessel segment radii less than 4 pixels 83
Figure 29. Bland-Altman comparison on the radii derived from segmentation and FWHM on vessel segment radii less than 4 pixels..... 83
Figure 30. Registration of 19 μm micro-CT volume to 57.6 μm micro-CT volume via featured bifurcation points 84
Figure 31. FWHM Radius comparison from 57.6 μm and 19 μm micro-CT images 85
Figure 32. Bland-Altman comparison on the FWHM Radius from 57.6 μm and 19 μm micro-CT images 85
Figure 33. Regression plots for vessel segments radii from Gaussian correction 57.6 μm micro-CT images and FWHM on 19 μm micro-CT images..... 86
Figure 34. Bland-Altman comparison on the Gaussian corrected radii from 57.6 μm micro-CT images and the FWHM radii from 19 μm micro-CT images..... 86
Figure 35. Intensity plots of center points with the Gaussian corrected radii from 57.6 μm micro-CT images 87
Figure 36. Illustration of the extracted centerlines overlaid MIP view and 3D surface rendering subtree with segmented radii less than 8 pixels from 57.6 μm micro-CT volume 88
Figure 37. Plots of segment counts on the length and radius extracted from the selected subtree in Figure 36 89

Figure 38. Plots of vessel segment radii measured from FWHM and Gaussian correction for the selected subtree in Figure 36 89
Figure 39. 3D surface rendered subtree with unit radius 90
Figure 40. 3D surface rendered subtree with color mapping on the segmented radii, and color mapping on the Gaussian corrected radii 91
Figure 41. 3D surface rendered liver with color mapping on the Gaussian corrected radii 92
Figure 42. Schematic diagram of 3D volume rendering. 99
Figure 43. 3D visualization on the VX2 implanted rabbit liver lobe 100
Figure 44. 3D volume rendered views on local tumor microvasculature with color mapping of measured distance-to-boundary values 102
Figure 45. The pseudo code of smoothed particle hydrodynamics simulation 108
Figure 46. Surface mesh on a reconstructed vascular model. 110
Figure 47. The demonstration of microsphere simulation via the web application interface 111

CHAPTER 1 INTRODUCTION

Embolotherapy is an effective interventional therapy for patients with intermediate-stage hepatocellular carcinoma. Taking advantage of hypervascular characteristics from hepatocellular carcinoma, the embolic agents injected into hepatic arteries via a catheter block the tumor-feeding arteries. The degree of targeted embolization depends on how successfully the embolic agents are transported to the tumor-feeding arteries and lodged near the tumors. In addition, being able to minimize and detect non-targeted embolization is a major concern for radiologists. Since blood flow is the only propulsive force on the embolic agents after they are released into the hepatic arteries, hemodynamic changes caused by the interaction between embolic agents and blood flow is crucial to the success of embolotherapy. This chapter summarizes the key aspects of embolotherapy and the factors that influence its hemodynamics, as well as reviews current clinical monitoring techniques to provide an overview for further study on how they interact to assist radiologists in improving their practice.

1 Liver Cancer

As of 2018, liver cancer is the fourth leading cause of cancer-related deaths worldwide and the second leading cause of cancer death among men in 20 countries [1]. There were gradual increases in both incident cases and deaths annually with nearly

8.2% mortality. Hepatocellular carcinoma, also called HCC, is the most prominent malignancy of the liver, representing about 80% of all primary liver cancers.

According to the Barcelona Clinic Liver Cancer (BCLC) staging system, which links the disease stage to a specific treatment strategy [2], patients are classified into early, intermediate, and advanced stages. At an early stage, patients with a single nodule of less than 3 cm in diameter or no more than three nodules with less than 3 cm in diameter are eligible for curative treatments like surgical resection, liver transplantation, or ablation. Patients are considered at the intermediate stage when the condition exceeds the early stage, but the patient is free of cancer-related symptoms. Patients having cancer-related symptoms, vascular invasion and extrahepatic cancers, are classified as advanced stage. Due to the late presence of signs and symptoms, most patients are diagnosed at an intermediate or advanced stage that renders them ineligible for curative therapies and thus receive only palliative or conservative treatment [3].

The liver has a unique dual vascular supply receiving blood from the hepatic artery and the portal vein [4]. It receives approximately 25% of its blood supply from the hepatic artery and ~75% from the portal vein. The hepatic artery obtains blood from the aorta and transfers oxygenated blood to the liver to support its normal function, while the portal vein collects partially deoxygenated blood from the veins of the gastrointestinal tract, gallbladder, pancreas and spleen that contain nutrients and toxins absorbed from digested materials. Briefly, the blood mixture passes through sinusoids, which are the cavities between plates of hepatocytes, and then converges into the hepatic vein where the deoxygenated blood subsequently leaves the liver into the inferior vena cava and

eventually flows back to the heart to complete the circulation. At histological scope, the liver is made of millions of lobules, the functional units. Each lobule consists of portal triads, sinusoids, and a central vein. A hepatic arteriole, a portal venule, together with a bile duct constitute a portal triad. Visually, a hexagonally-shaped lobule has portal triads at each corner, one central vein at the center, and sinusoids in between. Blood mixtures from hepatic arterioles and portal venules converge into sinusoids and then converge into the central veins.

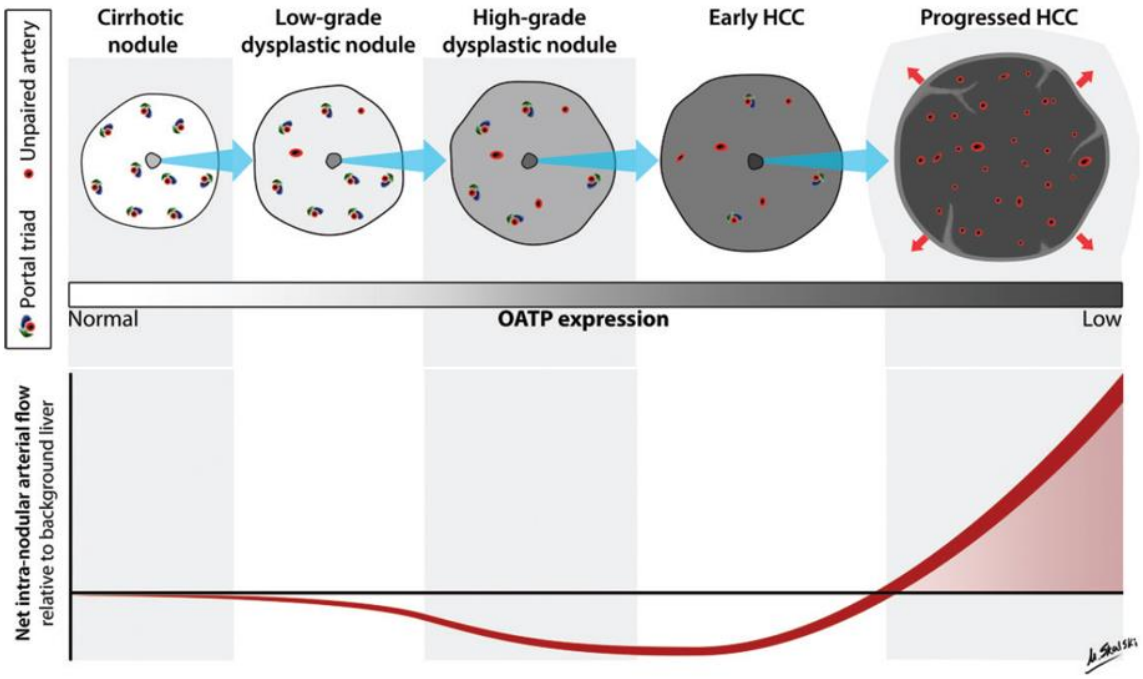

Figure 1. Hemodynamic changes during multistep hepatocarcinogenesis. (Reprinted, with permission, from *Radiology* 2014;272:635-654. Illustration by Matt Skalski, MD. © RSNA) [5] As normal portal triads are replaced by unpaired arteries in an increased number, the net hepatic arterial flow increases in progressed HCCs. This hypervascularity feature is displayed as hyperenhancement in the arterial phase of CT and MR imaging with extracellular agents.

For early HCC nodules, isolated arteries present with missing portal veins and/or bile ducts, while the number of normal portal triads gradually decrease. At a pathophysiological level, the blood flow to early HCC nodules decreases with the gradual decrease in the number of the normal portal triads. For advanced HCC nodules, the number and size of the abnormal arteries increase while the portal triads are practically absent, as illustrated in Figure 1. Due to the formation of isolated arteries, these HCC nodules have increased intranodular arterial supply accompanied with reduced or absent portal venous flow [5]. In other words, blood from arteries is almost the only supply source for progressed HCC nodules. The hallmark diagnostic feature of HCC is that most progressed HCCs display arterial hypervascularity with hyperenhancement in the arterial phase of CT and MR imaging with extracellular agents.

2 Embolotherapy for Liver Cancer

Taking advantage of the vascularity feature on progressed HCCs, transcatheter arterial embolotherapy has been widely recommended as one of the main supportive treatments for non-surgical resection of liver cancer, especially for HCC patients in intermediate-advanced stage. Embolotherapy, introduced in the 1970s, requires placing a catheter into the hepatic artery via a femoral artery puncture and navigating the catheter into its branches guided by conventional digital subtraction angiography (DSA) with continuous contrast administration. The embolic agent is released in a feeding arterial branch proximal to the tumor, with the intent of landing in the distal arterioles of the

tumor. The specific arterial branch is chosen based on antegrade flow to the tumor. Most regimens implement the injection of the embolic agents until the complete stasis of antegrade blood flow to the tumor as visualized under DSA.

Embolotherapy supports liver cancer treatment using two basic mechanisms. First, the embolic agents occlude the arteries supplying the tumor and prevents nutrients and oxygen to reach the tumor. Second, when the embolic agents are lodged near the tumor, any therapeutic drug that was previously injected and restrained by the embolic agents, or was loaded in the embolic agent, can be utilized to inhibit tumor cell function locally.

There are several different types of embolization procedures which differ by the choice of embolic agents, therapeutic drugs, and the delivery of the drug. Transarterial bland embolization (TAE) is the procedure of introducing only the embolic agents to block the tumor blood supply while conventional transarterial chemoembolization (c-TACE), drug-eluting beads transarterial chemoembolization (DEB-TACE), and transarterial radioembolization (TARE) additionally involve the delivery of chemoagents or radioactive agents. C-TACE consists of injection of a combination of a cytotoxic drug with poppyseed oil (lipiodol) then followed by an embolic agent to seal the blood supply. DEB-TACE and TARE use a similar strategy whereby the embolic agents, along with their embolization effect, are also carriers of either chemotherapeutic drugs or radioactive material: after the embolic agents flow under physiologic pressures to tumor sites, they can continuously release the therapeutic components locally.

Embolotherapy, though it may not completely eliminate the tumor, has been a prevalent approach for patients with intermediate-stage HCC. Embolization therapies for most patients with HCC who are unsuitable for resection show promising efficacy, safety, and tumor control. However, there is no consensus on the best therapy because there is no consistent evidence to indicate any treatment is superior to the others [6]. Globally, there are statistically significant differences between countries in transarterial embolotherapy practice patterns in the use of chemo-drugs, embolic agents, type of procedures, and the choice of imaging follow-up [7,8].

3 Hemodynamic Impact Factors during the Transarterial Procedure

The ultimate goal of embolotherapy is to guarantee high accumulation of therapeutic drugs and embolic agents into or near the liver tumor. Therefore, embolotherapy should maximize the targeted administration and minimize the non-targeted delivery of drug and embolic agents.

Patients undergoing embolotherapy should be carefully selected based on their performance status, tumor conditions, liver functions, and response to treatment [9, 10, 11]. During the procedure, an unintended delivery of embolic agents and drugs is a big concern because it can cause ischemic infarction on the affected normal organ including liver, gallbladder, spleen infarction, gastrointestinal mucosal delivery [12]. Regardless of the patient's physical conditions and therapeutic drugs used, vascular

variations and physiological parameters influencing blood pressure and local flow should be considered to achieve the optimal embolotherapy.

3.1 Effects of Flow Dynamics under Non-targeting

The heart maintains the blood pressure by continuously pumping blood. This pumping creates pressure that propels blood to the peripheral organs and tissue. Locally, the flow is generated by blood being pushed from a vessel with greater pressure to vessels with lower pressure. While embolization occurs locally, the blood pressure changes and affects the corresponding local blood flow and blood distribution as well.

Under normal systemic blood pressure, any cross-section inside the vascular network divides the vessel segment into (1) the upstream feeding compartment with higher relative pressure and (2) the downstream vascular territory with lower relative pressure. This flow based on the decrease of systematic blood pressure is called antegrade flow.

Non-targeted administration may be caused by the therapeutic materials and/or embolic agents being distributed into normal tissue in two ways: (1) antegrade flow into the downstream distal, and/or (2) retrograde reflux into upstream arterial branches.

Due to vascular variations and/or catheter caliber limitations, there is a potential downstream non-targeting if the placement of the catheter is restricted to upstream of the tumor feeding vessel and the downstream vascular territory of the catheter tip involves normal tissue.

The circumstances that would lead to retrograde reflux may be (1) the downstream occlusion being too close to the tip of the catheter, (2) the resistance to downstream flow being high, or (3) the injection rate exceeding the arterial acceptance.

3.2 Prophylactic Embolization

If angiography detects that extrahepatic organs are supplied by the hepatic artery, or if a non-hepatic artery is also the feeding vessel of the tumor, super-selective embolization should be performed. Arteries often considered for prophylactic embolization to prevent extrahepatic non-targeting are the gastroduodenal artery, the right gastric artery, and other arteries depending on the patient's vascular variation. Coil embolization of the relevant arterial branches is the standard practice for protecting extrahepatic and/or hepatic non-targeting arteries. It enables flow redistribution by maintaining flow to the hepatic artery while restraining flow to the non-targeting organs and/or subsegmental normal liver [13]. It is a very effective way to prevent non-target embolization and to enable the introduction of therapeutic drugs and embolic materials from a single injection site [14]. After being occluded by prophylactic embolization, the affected areas are supplied by the rich collateral of distal vessels either in the upper abdomen or inside the liver.

3.3 Flow-controlled Catheters

Reflux does not occur in all circumstances. The degree of reflux may depend on the injection speed, the resistance downstream of the catheter, the blood pressure, the downstream anatomical structures. Instead of permanent occlusion in the arteries, which potentially is affected by the reflux of embolic agents, a temporary control on blood flow to avoid reflux during the procedure is desirable. Physically blocking the embolic agents from going upstream during the injection with a flow-controlled catheter is an efficient way to achieve targeting embolization and reduce the occurrence of reflux as well.

3.3.1 Forward Flow Arrested Microcatheter

Use of a balloon-occluded catheter with an expandable tip has been demonstrated to be a safer and more practical way to prevent retrograde reflux during the embolization procedure. It has a balloon tip that can be inflated manually to fill the tumor feeding artery that directly and temporarily blocks the blood flow in the artery, eliminates the possibility of the embolic agents' retrograde reflux and avoids the loss of embolic agents (Figure 2b). The downstream vascular territory of a balloon-occluded catheter will lose antegrade blood flow when the balloon tip is fully expanded.

3.3.2 Low Flow Microcatheter

Compared to a catheter with a balloon-shaped tip, an anti-reflux microcatheter with a pliant braided polymer cone-shaped tip (Surefire Infusion System [SIS]; Surefire

Medical, Inc., Westminster, CO) was also introduced to prevent non-targeting from retrograde reflux. With the self-expandable tip, the SIS catheter creates dynamic occlusion during the cardiac cycle. Three states of SIS catheter were observed under fluoroscopy and angiography: antegrade systolic flow (tip is collapsed significantly), antegrade diastolic flow (tip is collapsed only slightly) and arrested retrograde flow (tip is fully sealed to the vessel wall) [13]. The catheter tip of the anti-reflux Surefire catheter is affected by cardiac cycle blood pressure and the injection pressure and speed. When injecting, the cone-shaped tip is fully expanded to arrest the antegrade blood flow and retrograde reflux as well. After injecting, the tip collapses to allow antegrade flow and it expands and contracts due to the blood pressure fluctuation caused by the cardiac cycle. (Figure 2c). In general, the intermittent low antegrade flow is still maintained.

3.3.3 Reflux Reduction Microcatheter

Unlike the previous two types of catheters, the SeQure® microcatheter (Guerbet, Roissy CdG, France) does not have a mechanical occlusion component. Its distal tip has side slits designed to filter out fluid only, and to allow outflow of the suspension fluid without passage of embolization beads [15,16]. During the injection of the contrast-embolic agents' suspension, the turbulence formed by the contrast media crossing through the side slits becomes an external fluid barrier which reduces the reflux of the embolic agents that are expelled through the tip to prevent non-target embolization (Figure 2d). Normal blood flow is preserved after the injection.

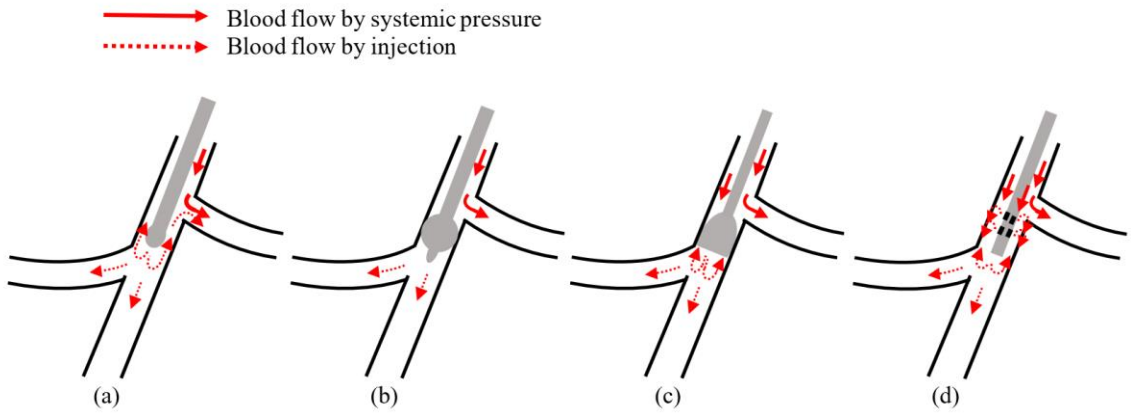

Figure 2. Schematic flow while injecting under various types of micocatheters: (a) standard end-hole microcatheter: reflux occurs while injecting; (b) Forward flow arrested microcatheter: Balloon-occluded catheter with an inflated balloon tip filled in the tumor feeding artery directly and temporarily blocks the blood flow in the artery, completely eliminating the possibility of the embolic agents' retrograde; (c) Low flow microcatheter: SIS cone-shape tip catheter with fully self-expanded tip caused by the injection flow acts as a balloon-occluded catheter while the tip is inflated to arrest blood flow temporarily; after the injection, the antegrade blood flow recovers through the collapsed tip that expands and contracts following the cardiac cycle; (d) Reflux reduction microcatheter: SeQure® microcatheter has side slits on the distal tip which form an external fluid barrier by the contrast media passing through, which reduces the reflux of the embolic agents that are expelled through the tip to prevent non-target embolization.

3.3.4 Clinical Findings

The flow-controlled catheters were primarily designed to prevent the retrograde reflux of embolic agents during the embolization procedure. However, it has been found that the occlusion of antegrade flow by the catheter tip also promotes targeting and antegrade protection by altering the downstream hemodynamics [17,22,23]. The pressure downstream of the catheter tip in both forward flow arrested and low flow microcatheters has been documented to be decreased compared to the pressure at other places [13,18,19,20,21,22,23,24]. This decrease in pressure can enable reversal of flow

in downstream normal arteries (Figure 3) to direct the embolic agents to the target tumor resulting in better HCC local accumulation of therapeutic materials [22] and increased the targeting and non-targeting ratio [19].

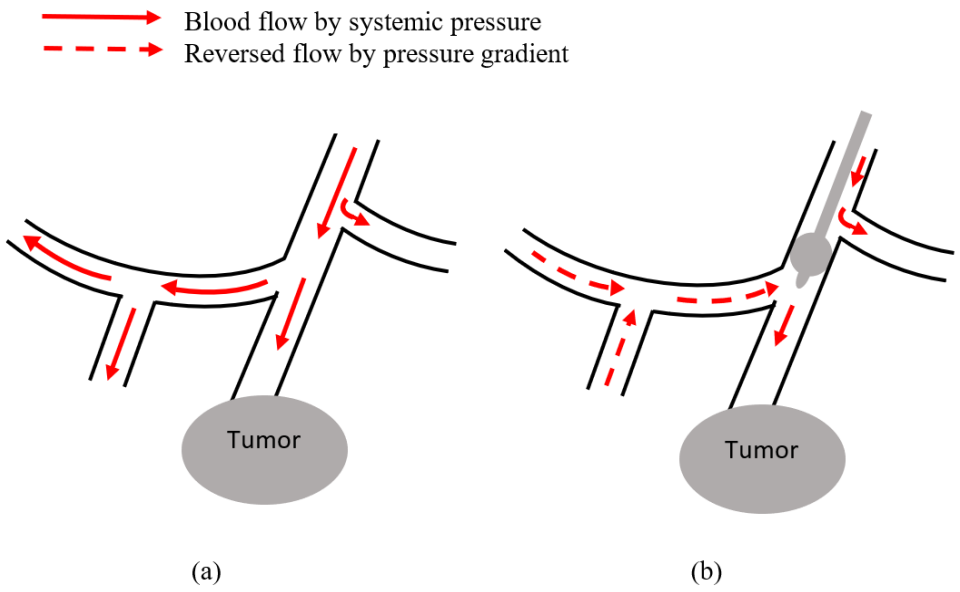

Figure 3. Schematic diagram of blood flow at catheter downstream: (a) blood flow caused by systemic pressure; (b) a decreased pressure at catheter downstream of the inflated balloon tip causes the flow in non-targeting downstream territory to reverse and then go to the tumor.

Certainly, such increased targeting with flow-controlled catheters does not occur in all cases. It was mentioned by Irie et al. [22] that some patients had no significant downstream pressure decrease with no dense accumulation in HCC. Asayama et al. [25] deduced that the feeding artery below the catheter occlusion was reconstructed by collateral vessels, which enable inflow to downstream initially due to the pressure gradient caused by decrease downstream blood pressure then quickly balance the pressure difference. The extent of reduction on BOASP may be an indicator of the distal

arterial blood flow. A quantitative standard on BOASP is given as 64 mmHg or less as a good reference for B-TACE to achieve better HCC local accumulation of therapeutic materials [20,22].

Hatanaka et al. [26] further illustrated the hemodynamic changes of the balloon-occluded transcatheter arterial chemoembolization procedure. After the balloon catheter was inserted into the tumor-feeding artery and inflated to occlude the antegrade flow, the intrahepatic collateral arteries (ICAs) were immediately formed to maintain distal arterial blood flow. The vascular patterns observed under computed tomography hepatic arteriography (CTHA) can be explained by the different circumstances of ICAs below the balloon occlusion, which was also reflected on the changes of the BOASP measured by balloon-occluded catheters [26]: (1) Increased tumor stain under an inflated catheter tip reflects the possible existence of thin downstream ICAs, because the contrast medium could flow back to downstream under the pressure gradient through ICAs and create more contrast concentration; (2) A decreased tumor stain compared to when the catheter head is deflate implies the possibility of thick downstream ICAs, because blood could also flow back downstream through the ICAs and thereby dilute the contrast medium.

No clinical studies were found that evaluated the changes in the downstream pressure using the SeQure® microcatheter, since it was launched recently. A case review of prostate artery embolization for a patient with benign prostatic hyperplasia reported the contrast was observed exiting through the side hole at the distal segment of the catheter from fluoroscopy, creating the protective pressure gradient and reducing reflux resulting in a thorough embolization of prostate suggested in the cone-beam CT images [27].

One thing that needs to be mentioned is that fluoroscopic evidence of stasis or reflux is usually an important indication for physicians to stop the procedure. With the reserved normal blood flow, the SeQure® microcatheter may have the same endpoint as the standard microcatheter. However, for the other two flow-controlled catheters, the angiographic endpoint of embolization is not directly attainable due to the occlusion control of antegrade flow. Kakuta et al. [21] investigated the optimized injection duration of balloon occlusion to maximize the therapeutic materials accumulation inside the HCC nodules and suggested 70 mmHg as a possible indicator of the endpoint for arterial injection.

The ideal case that a catheter can be placed in the tumor-supplying vessel is rarely present. On the other hand, one study showed that, under histopathologic examination of resected HCC tissue, tumor cells are detectable in the parenchyma in the vicinity of the tumor even if the tissue does not have conspicuous hypervascular structure. In this case, the optimal release position of the embolic agents cannot be determined solely based on macroscopic indicators. More factors should be considered before performing the transarterial procedure including the downstream vascular territory coverage.

3.4 Particulate Embolic Agents

Many considerations have been engaged in the fabrication of the embolic agents in order to improve the clinical effectiveness of embolotherapy [28]. The current embolic agents on the market have addressed considerations of appearance, shape, capability of

drug loading, and biodegradability. Whether embolic agents are shaped spherically or irregularly, they are considered microparticles because their size is in the micron range. Embolic agents with a spherical shape are also called microspheres or beads. As discussed above, during routine transarterial procedures related to embolization for treating HCC, the embolic agents can act to occlude the blood vessels, to seal the therapeutic chemo-drugs in the vicinity of the tumor, or to directly work as a drug carrier possessing the capability of loading therapeutic materials and releasing them into the blood near the target. Drug-loaded microspheres or beads can sustain the local drug release to achieve both the therapeutic effect and the occlusion of the blood supply. The biodegradation feature of embolic agents enables hepatic recanalization and repeated embolization. Table 1 and Table 2 summarize the characteristics of current embolic particles as an embolizing agent and/or carrier for embolotherapy.

The ideal embolic agent should be inert, biocompatible, safe and effective to occlude the blood flow completely from peripheral to proximal arteries, simple to administer without clogging the catheter and accumulating near the catheter, easy to fabricate and sterilize, biodegradable [29,30], imaging detectable, and capable of loading drugs. Additionally, the drug carrier should also be capable of achieving high drug loading, be able to load both hydrophilic and hydrophobic drugs, allow controlled and sustained drug release to increase the exposure time of the tumor to chemotherapy, and minimize the systemic plasma concentration and any subsequent undesirable adverse effects and toxicity to normal tissues [31,32].

Table 1. Summary of the characteristics of current embolic particles in the market used for TAE, TACE and DEB-TACE (*: DEB-TACE is not approved in US)

Name	Company, Territory	Volume/Pack	Color	Available Calibrated size (μm)	Properties	Designed for*
Callisphere®	Jiangsu Hengrui Medicine, China	2 ml / Vial	Blue	100-300; 300-500; 500-700;700-900; 900-1,200	Spherical, non-aggregating, biocompatible, compressible, drug loadable	TAE; TACE; DEB-TACE
DC Bead™	Boston Scientific, UK	2 ml / Vial	Blue	100-300; 300-500; 500-700	Spherical, non-aggregating, biocompatible, compressible, drug loadable	TAE; TACE; DEB-TACE
DC Bead LUMI™	Boston Scientific, UK	2 ml / Vial	Yellow	70-150; 100-300	Spherical, non-aggregating, biocompatible, compressible, drug loadable, X-ray imagable	TAE; TACE; DEB-TACE
LC Bead®	Boston Scientific, USA	1 ml or 2 ml/ Vail	Blue	100-300; 300-500; 500-700; 700-900; 900-1,200	Spherical, non-aggregating, biocompatible, compressible, drug loadable	TAE; TACE; DEB-TACE
LC Bead LUMI™	Boston Scientific, USA	2 ml / Vial	Blue	70-150	Spherical, non-aggregating, biocompatible, compressible, drug loadable, X-ray imagable	TAE; TACE; DEB-TACE
LifePearl®	Terumo European Interventional Systems, Belgium	2 ml / Syringe	Green	100±25; 200±50; 400±50	Spherical, non-aggregating, biocompatible, compressible, drug loadable	TAE; TACE; DEB-TACE
QuadraSphere®/ HepaSphere™	Merit Medical, USA / Canada	Vial packaged dry	Natural	20-40 (US only); 30-60; 50-100; 100-150; 150-200	Spherical, absorbable, degradable, non-aggregating, biocompatible, compressible, drug loadable	TAE; TACE; DEB-TACE
Oncozene™/ Tandem™	Varian, USA/EU	2 ml or 3 ml / Syringe	Various	40±10; 75±15; 100±25	Spherical, biocompatible, compressible, drug loadable	TAE; TACE; DEB-TACE
Bead Block®	Boston Scientific, USA	20 ml / Syringe	Blue	100-300; 300-500; 500-700; 700-900; 900-1,200	Spherical, non-aggregating, biocompatible, compressible	TAE

Table 1. (Cont) Summary of the characteristics of current embolic particles in the market used for TAE, TACE and DEB-TACE (*: DEB-TACE is not approved in US)

Name	Company, Territory	Volume/Pack	Color	Available Calibrated size (µm)	Properties	Designed for*
Ekobi™ 500	ImbioTechnologies, Canada	20 ml / Vial	Natural	40-100; 150-180; 180-212; 212-300; 300-425; 500-800	Spherical, absorbable, degradable, non-aggregating, biocompatible, Ultrasound Imagable	TAE; TACE
Embozene™	Varian, USA	2 ml / Syringe	Various	40, 75, 100, 250, 400, 500, 700, 900, 1,100, 1,300	Spherical, absorbable, degradable, biocompatible, compressible	TAE; TACE
EmboSphere®	Merit Medical, USA	2 ml / Syringe	White	40-120; 50-100; 100-300; 300-500; 500-700; 700-900; 900-1,200	Spherical, non-aggregating, biocompatible, compressible	TAE; TACE
HydroPearl®	Terumo European Interventional Systems, Belgium	2 ml / Syringe	Various	75±30; 200±75; 400±75; 600±75; 800±75; 1,100±75	Spherical, non-aggregating, biocompatible, compressible	TAE; TACE
OptiSphere™ (formerly Gel-Bead™)	Medtronic, USA	20 ml / Syringe	Yellow	100–300; 300–500; 500–700; 700–1,000	Spherical, absorbable, degradable, non-aggregating, biocompatible, compressible	TAE; TACE
X-Spheres™	Interface Biomaterials, Netherlands	20 ml / Syringe	Yellow	400-600; 600-710; 710-850	Spherical, biocompatible, X-ray imagable	TAE for uterine
Bearing nsPVA®	Merit Medical, USA	Vial	White	45-150; 150-250; 250-355; 355-500; 500-710; 710-1,000; 1000-1,180	Non-aggregating, biocompatible, compressible	TAE; TACE
Contour SE™	Boston Scientific, USA	3 ml / Vial	White	45-150; 150-250; 250-355; 355-500; 500-710; 710-1,000; 1,000-1,180	Non-aggregating, biocompatible, compressible	TAE; TACE

Table 2. Summary of the characteristics of current embolic particles in the market used for TARE

Name	**Company**	**Territory**	**Available Calibrated size (µm)**	**Capable of radionuclide loading**	**Imaging visible**	**Designed for**
SIR-Spheres®	Sirtex Medical Limited	Australia	20-60	Yttrium-90 resin microspheres	MRI/SPECT	TARE
TheraSpheres®	Boston Scientific	USA	20-30	Yttrium-90 glass microspheres	MRI/SPECT	TARE
QuiremSpheres®	Terumo European Interventional Systems	Belgium	15-60	Holmium-166 microspheres	MRI/SPECT	TARE
QuiremScout®	Terumo European Interventional Systems	Belgium	15-60	dual isotope (166Ho/99mTc-colloid)	MRI/SPECT	TARE

3.5 Direct Intraprocedural Imaging Monitoring

Monitoring the hepatic arterial blood flow and microsphere distribution is important because it gives physicians insight into the procedure's progress so they can predict the therapeutic effect. As mentioned before, the blood pressure measured at the tip of the catheter can provide dynamic monitoring of the embolization procedure and indirectly reflect the downstream occlusion level. Besides, clinical imaging techniques play a vital role not only in the diagnosis of HCC [36] but also in monitoring the embolization procedure. The most common modalities used for monitoring intraprocedural embolization are digital subtraction angiography (DSA), fluoroscopy, angiography, and computed tomography (CT). In the course of embolotherapy, the use of a contrast medium, in conjunction with fluoroscopy and DSA, allows guiding the catheter to the appropriate location and to find the tumor-supplying blood vessels. In this process, the contrast agent needs to be intermittently administered to counterbalance the dilution by the blood flow to continuously monitor the change in blood flow.

3.5.1 Lipiodol

Lipiodol, also known as ethiodized oil, is an important medium used in the chemoembolization procedure. It is an oily, injectable fluid with iodine content that is radiopaque and able to be visualized under radiographic imaging. It has the capability of carrying chemotherapeutic agents to form lipiodol emulsion (LE), is used as a surrogate marker to estimate the spatial distribution of chemotherapeutic agents inside the vessels

and is also a tumor-seeking agent [37]. Lipiodol, as a liquid vehicle, does not form the complete arterial occlusion. During chemoembolization, an embolic agent is needed to seal the feeding artery of the tumor right after LE is injected via a catheter. LE that accumulates near the tumor can clearly reflect the size and contour of the tumor and is a good indicator for the surveillance of HCC nodules by CT scans. Studies [20,21,22] indicate that there is a correlation between the LE accumulation in the tumor and the therapeutic effect. If LE is accumulated, a better therapeutic effect can be expected, assuming LE indicates presence of therapeutic agents. In an investigation on the accuracy of Lipiodol as an imaging marker of chemotherapy drug delivery after liver tumor chemoembolization from an animal model of HCC, Garcia et al. [38] found that the Lipiodol content is a poor quantitative predictor of local doxorubicin concentration after liver tumor chemoembolization.

3.5.2 Imaging Visible Microspheres

Even though Lipiodol can be detected under X-ray based imaging modalities due to its radiopaque iodinated component, the majority of microspheres currently on the market are not directly imaged. The microspheres need to be mixed with contrast when being administered to allow monitoring with the assistance of imaging techniques. The dynamic distribution of the embolic agents can be indirectly reflected through a serial angiogram showing a gradual decrease of the contrast from the peripheral to the proximal

end of the catheter tip. Tracking the trajectories of the microspheres and their final location in the vessels below the flow interruption is still desirable.

Loading radiopaque contrast into commercially available microspheres is an efficient means to render the microspheres imageable under X-ray based imaging modalities. Lipiodol loaded into lyophilized PVA-hydrogel DC/LC beads has been successfully visualized under intraprocedural fluoroscopy and computed tomography (CT) imaging during transcatheter embolization [39,40,41]. In the studies of loading Lipiodol and doxorubicin into drug-eluting beads [40,41], it has been found that the doxorubicin-Lipiodol-loaded radiopaque beads have larger size and more homogeneous concentration of Lipiodol than solely doxorubincin-loaded and Lipiodol-loaded beads. Less surface area to volume ratio of the radiopaque beads explains the fact that their doxorubicin elution was slightly slower than nonradiopaque beads. Due to Lipiodol loading, the radiopaque beads resulted in more rapid settling and required frequent mixing during catheter delivery.

DC Bead LUMI™ /LC Bead LUMI™ (Boston Scientific USA), radiopaque drug-eluting beads, have been developed based on the DC/LC Bead™ platform in which the blue tinting step was replaced by an alternative reaction to couple the radiopaque compound (tri-iodinated benzyl) to the polymer backbone [42]. It has been shown that DC/LC Bead LUMI™ are visible after their accumulation in hepatic arterial branches after embolization on all X-ray based modalities and offer intra-procedural benefits on endpoint determination, discovery of regions of under-treatment and identification of non-target embolization [43,44]. However, in terms of intra-procedural monitoring, the

beads were not visible when leaving the catheter tip with real-time fluoroscopy. In a study [45] comparing different imaging protocols of CBCT images on DC/LC Bead LUMI ™ distribution, with decreasing kVp the distribution under CBCT demonstrated a significantly better correlation to micro-CT images. To visualize a more detailed distribution of radiopaque beads inside tissue and retain the anatomic structure on images, the tradeoff between x-ray penetration and attenuation is not negligible and is worthy of consideration.

3.5.5 Endpoint Stasis

The complete stasis embolic endpoint during embolization can achieve complete tumor necrosis induced through the hypoxia by embolization-induced ischemia, while increasing the dwell time of injected or loaded cytotoxic agents. The optimal embolic endpoint for embolization has not been elucidated. Jin et al. [46] studied the effect of a sub-stasis endpoint during embolization on survival among 105 HCC patients showing a survival improvement compared with a stasis endpoint. Although incomplete embolization during embolization may inadequately treat targeted tumors, excessive embolization may increase hepatotoxicity induced by hypoxia and necrosis and stimulate angiogenesis by the expression of angiogenic growth factors secreted by tumor cells, which may increase the risk of accelerating liver decompensation and enhance the likelihood of tumor recurrence.

4 Indirect Hemodynamic Studies

Imaging technologies are often utilized for evaluating tumor-targeting after treatment, but they cannot provide flow dynamics and distribution information during the treatment process, nor can they monitor the embolic agents that have gone elsewhere. With the limitations of monitoring blood dynamics, the indirect hemodynamic studies which are used to understand the hemodynamics become the auxiliary means for achieving optimal results.

4.1 Pre-evaluation on Flow Distribution

Radionuclide loaded, radiolabelled microspheres used in TARE can be imaged via radionuclide-based imaging techniques to acquire functional and molecular information about the tumors. Common radionuclide imaging techniques include positron emission tomography (PET) and single photon emission computed tomography (SPECT), since these techniques are highly sensitive and quantitative. However, radionuclide-based imaging modalities have relatively poor spatial resolution and are usually done alongside anatomical imaging techniques such as CT and MRI.

Technetium 99m-labeled macroaggregates of albumin (Tc99m-MAA) are used prior to Yttrium 90-microsphere embolization to pre-delineate the accumulation in a target liver site through SPECT, which provides prospective embolic agents perfusion on later embolization [47]. However, Ilhan et al. [47] found a low correlation between Tc99m-MAA and Yttrium 90-microspheres by discovering that some lesions with high

uptake of Yttrium 90-microspheres showed even lower pre-therapeutical uptake of Tc99m-MAA than healthy liver tissue.

4.2 Values on Images

Wang et al. [48] suggested that two parameters derived from transcatheter intraarterial first-pass perfusion (TRIP) MR images after each iterative administration of embolic agents could monitor the blood flow reduction in tumor perfusion: area under the intensity curve (AUC) and maximum upslope of the curve (MUS). These two parameters obtained from the images on tumors could semi-quantitatively provide information on the embolic stage and track the optimal endpoints. Three-dimensional conventional angiography facilitates finding the optimal catheter placement locations in complex vascular networks compared to traditional DSA, thereby reducing radiation and contract injection since dynamically tracking down the embolic agents is impossible for either DSA or angiography due to the invisibility of embolic agents.

Studies have investigated the capabilities of pretreatment functional imaging for the prediction of treatment response to embolization. The arterial perfusion rate from computed tomography (CT) perfusion can predict tumor morphologic response 4 months after TARE and 1-year survival after radioembolization [49]. Furthermore, Reiner et al. [50] were trying to predict the therapy response on tumor heterogeneity, one of the important prognostic factors in tumor treatment, by voxel-based histogram analysis through CT perfusion imaging. However, the histogram analysis of arterial perfusion

(AP) values only indicated differences among responders and non-responders at a certain cutoff. Although the arterial perfusion rate can potentially provide evidence on patient selection, CT perfusion is not reliable due to no standard protocol, is hard to evaluate, and is not routine before treatment.

5 Clinical Concern and Gaps

So far, various factors affecting hemodynamics have been studied, such as catheter placement, microsphere characteristics (size, quantity, and type), catheter type, and microsphere injection techniques (injection timing, velocity, and interval). In clinical settings, the placement of a catheter to release microspheres is the first consideration. The preferential location of a catheter is as close as possible to the tumor-feeding vessel(s). If there exists more than one tumor-feeding vessel, multiple locations to the tumor-feeding vessels are selected to release microspheres via a catheter. The secondary consideration is the size of microspheres, which range from 40 μm to 300 μm in diameter depending on the caliber of the tumor-feeding vessels and the dimension of the tumor. However, TARE often adopts smaller microspheres around 20-60 μm. Injection technique subdivides into injection speed, injection timing, and injection interval. In principle, an injection needs abide by the vessel affordability that is the vessel size and the flow rate. That is a slower injection for smaller vessels with a lower flow rate, vice versa for larger vessels. The closest location to the tumor-feeding vessel is the most preferred. The catheter-tip position in relation to a vessel's lumen when injecting is rarely noticed and difficult to

know without an angiogram but is an open area to explore. Skill in maneuvering the microcatheters is another factor from the physicians' side since the microcatheters from different manufacturers have their inherent characteristics. The type of microspheres is determined according to the chosen embolotherapy on whether it is necessary to carry the therapeutic drug or material.

Utilizing computational analysis and simulation on particle-hemodynamics inside hepatic vascular models has been an effective preclinical approach to investigate the interaction among hemodynamic factors. One of the key components for reliable hemodynamic simulation is a geometric domain in which physiological boundary conditions can be applied to match the simulation-specified flow conditions. A geometric domain - also called geometric configuration, computational domain, or mathematical model - is defined as a three-dimensional (3D) vascular geometry. Currently, hepatic vascular geometries used for studying computational hemodynamic simulation are rare, have limited or truncated vasculature, and often lack the vasculature that microspheres are targeting. Existing imaging technology cannot provide a process for transmitting emboli. However, visualization of emboli transmission can be achieved through simulation models.

6 Specific Aims

In the work presented here, I have attempted to develop a set of procedures to construct a visualized embolization simulation model based on detailed and coherent anatomic vascular structures aiming to assisting embolotherapy.

In order to build the visualized embolization simulation model, a vascular model based on real hepatic anatomy with details and continuity is necessary. To ensure faithful vascular structures, a rabbit liver model was selected due to the similar dual hepatic blood system and well-developed cancerous VX2 model. To remain the details and continuity of microvasculature, tissue samples filled with contrast were kept intact to the maximum possible extent and scanned under micro-CT at multi resolution levels. The vascular model was reconstructed from the finer micro-CT images of each individual liver lobe and later registered them back to the entire liver structures derived from the coarser, whole-liver micro-CT images to achieve fidelity and detailed spatial vasculature under physiological conditions. The vascular modeling method, including vascular segmentation and vascular centerline extraction, was used to automatically generate the vascular network.

To overcome the modulation transfer function of micro-CT imaging system and faithfully reproduce objects reaching the imaging system limit, higher resolution micro-CT scans were performed on local tissue lumps. The dimension of microstructure extracted from the high-resolution micro-CT images were used as a benchmark to evaluate the accuracy of the vessels' radii on the reconstructed vascular model. In our reconstructed vascular model, the over-estimation of radii on smaller vessels was corrected by the Gaussian correction function. Registrations of partial microvasculature

from higher-resolution micro-CT images to individual lobes were performed to quantify comparison of vessel segment radii between the corrected size and the measurements from high-resolution micro-CT images.

Because liver tumors have hypervascularity features, modeling the cancerous vasculature is particularly important. We investigated a single liver tumor nodule to study the feasibility of tumor model for embolization simulation.

To achieve visualizing the real-time trajectories on how embolic agents are transported inside arteries, a hemodynamic model based on the reconstructed anatomical model was developed to simulate the dynamic flow changes. Under the effect of simulated blood flow, a particle-based simulation model, which was implemented through a web-based application, was developed to provide embolic agents' transportation within the reconstructed model.

7 Outline of the Thesis

In this dissertation, Chapter 2 introduces methods for obtaining animal liver samples which preserved vascular structures with anatomical details and continuity, and acquisition methods for micro-CT images. Chapter 3 presents the 3D reconstruction of an anatomic vascular network model based on the micro-CT images from the overall hepatic vascular structure and individual hepatic lobes vascular details. Chapter 4 studies the accuracy of the radius parameter in the vascular network model using high-resolution micro-CT images on partial microvasculature. Chapter 5 presents the 3D reconstruction

of VX2 liver tumor model. Chapter 6 presents an embolization visualization based on blood flow simulation from real blood vessel structures. Chapter 7 summarizes the results of this thesis.

CHAPTER 2 ANIMAL EXPERIMENTS AND MICRO-CT ACQUISITIONS

1 Background

Animal vascular models have been the primary means for preclinical research [51,52,53]. First, an animal model is of a moderately sized liver sample with scaled vascular anatomy. Second, it can provide a verification path for the simulation results of the computational models [54]. Embolization techniques have been performed in different animals to accumulate basic data before a clinical trial. Commonly used research animals for trans-arterial embolization include rabbit [55], canine [56], and mouse [57] models. A rabbit model is used because our research focuses on building the hepatic vascular network model for simulating the embolization on HCC. In a rabbit's hepatic circulation, blood is supplied by a dual system consisting of the hepatic artery and portal vein, the liver drains to the inferior vena cava by the hepatic vein, and bile juice drains to the duodenum through the bile duct, making it more similar to the human hepatic system and therefore preferable to other lab animals such as rats and mice. Furthermore, in normal conditions the anatomic structure and physiological parameters of the rabbit liver can be scaled to that of the human liver. Rabbit is also the candidate animal for building the VX2 liver model because the VX2 model has similar characteristics to human HCC and the method to introduce VX2 into rabbit liver is well-established [58].

The traditional methods of reconstructing microvasculature are concentrated in using histological sections that are slow and labor intensive. However, this process introduces structure distortion [59] and information loss [60]. In the past decade, in order to obtain intact vasculature, most of the studies [61-63] on vasculature are based on contrast-loaded corrosion casting samples that are processed by separating the tissue from the solidified in-vessel contrast. In addition, development of the imaging technologies [64-65] has made the reconstruction of the vasculature and microvasculature structure possible, which accelerates the study of vasculature modeling methods. Based on the geometric parameters extracted from the imaging data such as the vessel diameter at each segment, the spatial location of the vessel path and the relation among the vessel segments, a 3D model of the vasculature structure can be generated.

Micro-CT which provides high resolution images for 3D reconstruction with intact vasculature conservation has been used for the microvasculature studies [66-71]. Though it has the capability to capture more anatomic details, micro-CT still has the same limitation as the clinical anatomic imaging modalities. That is, the resolution of the images is limited by the scanner field of view (FOV). Traditional vascular corrosion casting restricts the image acquisition that can be used because the sample can't be dissected to scan the details. In addition, the vessel branches are easily lost on the microvasculature due to the fragile nature of the casting material [63]. In order to obtain accurate anatomic microvasculature continuously covering the arteries, arterioles, and precapillary from the images for reconstruction, a method which balances the sample size and the resolution needs to be developed. Furthermore, casting vasculature samples only

retaining the vasculature without tissue with has the drawbacks of fragility, absent distal portion, and are non-dissectible.

Aiming to build detailed and coherent anatomic vascular structures, we selected a commonly used preclinical animal model to ensure accurate vascular structure. The liver samples were processed with the remaining tissue that supports the contrast filled vasculature in order to preserve the detailed and coherent vascular network. Multi-resolution micro-CT imaging was performed on the whole livers, individual lobes, and several partial lumps from lobes for future studies of 3D reconstruction on the microvasculature and accuracy studies.

2 Materials and Methods

2.1 Normal Liver Model

Three female New Zealand White rabbits, with weight of 3.1 – 3.3 kg and with age of 112-121 days were used to conduct the perfusion on normal livers for micro-CT imaging. The study was approved and performed by the Institutional Animal Care and Use Committee at NAMSA (North American Science Associates, Inc., Minnesota).

2.1.1 Animal Handling

All the study animals were housed and quarantined from other study animals for at least one night prior to beginning the acute study. Housing for all animals followed the

test facility SOP 30-043 (Animal Care, Feeding and Housing of Rabbits). Animals were verified to be in good health through a physical exam performed by test facility veterinary care staff at the time of arrival and/or within two days prior to surgery. Before the anesthetization procedure, the animals were provided with food and water and not fasted. Animals were sedated and anesthetized by an intramuscular (IM) injection of ketamine (45 – 49 mg/kg) and xylazine (3 – 4 mg/kg). Upon sedation, a catheter was placed within the auricular vein. An endotracheal tube or respiratory mask was placed to ensure proper ventilation and the animal was maintained under general anesthesia with inhalant isoflurane (1.5 – 2.0 %). The surgical sites (abdomen and thorax) were shaved before the animal was transferred to the procedure room. Vital signs including body temperature, pulse oximetry, ECG, heart rate, and respiration were monitored during the surgery. The animal's body temperature was maintained by a heating pad. The animal was anesthetized to remain under general anesthesia during pre-surgery setup and transfer to the procedure room. On the day of surgery, the hepatic system of the rabbit was isolated using one of two cannulation techniques.

2.1.2 Microfil Perfusion

For the first study animal, the femoral artery was accessed, a vessel introducer was placed, and the animal was heparinized. Under fluoroscopic guidance, a guide catheter was advanced to the level of the celiac truck/common hepatic artery. Angiography was performed to evaluate the hepatic vasculature and to guide cannulation. A surgical laparotomy was performed to expose the hepatic vasculature. The hepatic

artery and portal vein were cannulated and ligatures were placed behind the cannulas to prevent retrograde perfusion. The animal was euthanized and dual perfusion of the hepatic artery and portal vein was performed.

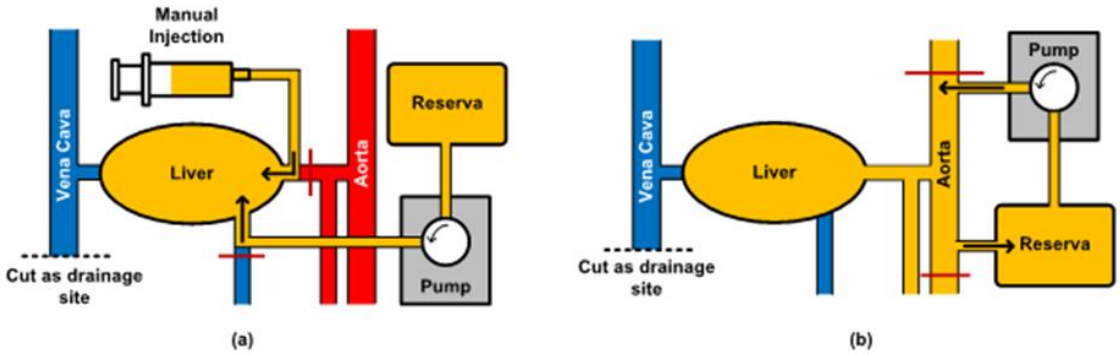

Figure 4. An illustration of liver perfusion set-up: (a) Two-ways perfusion through hepatic artery by syringe injection and portal vein by perfusion pump with constant flow rate; (b) one-way perfusion through aorta using perfusion pump with constant flow rate. A red line denotes that the vessel was clamped. Arrows represent the flow directions.

In the subsequent study animals, the aortic arch (distal to the left subclavian branch) and abdominal aorta (distal to the celiac branch) were cannulated. Ligatures were placed behind the cannulas (see Figure 4 red lines) to prevent retrograde and/or lower abdominal perfusion. The animals were heparinized, euthanized, and the perfusate was delivered via the thoracic aorta cannula and collected via the abdominal aorta cannula to create a flow “loop”.

2.1.3 Post-perfusion Sample Handling

All animals were humanely euthanized with an intravenous overdose of barbiturate-based euthanasia solution. Perfusion began with administration of a saline/heparin/lidocaine/albumin to clear blood from the organ and to prevent

vasoconstriction. The rate of perfusion depended on the size of the animal and the site of cannulation. During the perfusion procedure, the lower ascending vena cava was partially transected to allow for blood draining. Perfusion continued approximately 10-20 minutes until blanching of the liver and clear perfuse from the venous draining site were observed. Following blood clearance with the saline solution, Microfil® was perfused approximately 10 minutes until the Microfil® could be visualized within the microvasculature throughout the surface of the liver. The rate of perfusion depended on the size of the animal. Upon completion of the perfusion procedure, a vascular clamp was placed on the hepatic vein to prevent Microfil® from leaking from the liver. The animal was then placed in a cooler approximately 1 – 6 °C for up to 4 hours to allow the Microfil® cast to set. The liver was then excised, fixed in 10% neutral buffered formalin (NBF). The specimens were ready for micro-CT scan after the tissue was fixed.

2.2 VX2 Rabbit Liver Model

This study was approved by the Institutional Animal Care and Use Committee. The VX2 rabbit liver models were built by MD Anderson Cancer Center. The preparation of tumor for frozen storage is described in Appendix A. The preparation of tumor inoculation from frozen stock is described in Appendix B. The preparation of tumor inoculation is described in Appendix C.

2.2.1 VX2 Implantation on Donor Rabbit Thigh

For serial passage of tumor to obtain enough tumor inoculum for experimental animals, the VX2 tumor can only be propagated in live animals. It is not a cell line. While physically restraining the donor rabbit for no longer than 1 min, 0.3 to 0.5 ml of freshly thawed or freshly harvested from a donor rabbit and prepared (slurry) VX2 tumor fragments (approximately 3-4 mm3) are injected intramuscularly at a single site in both thighs through an 18 gauge needle attached to a 1-ml syringe. The slurry of prepared VX2 tumor fragments will not pass through a smaller gauge needle.

Two weeks after inoculation (tumor diameter approximately 1.5 cm), the donor rabbit is physically restrained for no longer than 1 min while anesthesia is induced by inhalation of 5% isoflurane/oxygen (1.5L/minute). After localizing each tumor by palpation, the animal is euthanized with an overdose of Beuthanasia (1.0 ml/10 lbs) or other commercially available euthanasia solution administered via a marginal ear vein. Each tumor is excised and fragments are prepared for transplantation.

2.2.2 VX2 Implantation on Receiver Rabbit Liver

The abdomen was shaved and prepared for aseptic surgery using alcohol and chlorhexidine. A small midline incision was made, and the left lateral lobe of the liver was exteriorized and inoculated at a single site with either 0.3 ml of freshly harvested and prepared VX2 tumor slurry or a single chunk (approximately 3-4 mm^3). The fragments were placed in the liver through an 18-gauge needle attached to a 1-ml syringe or a small incision in the liver lobe which was cauterized. The lobe will be replaced in the abdomen and the incision closed in layers with 4-0 Vicryl (the skin will be closed using a

subcuticular suture pattern). The animal was allowed to recover. Total time of anesthesia should be no longer than 60 minutes.

Tumors were allowed to grow for 5 to 14 days prior to a procedure depending on the size of tumor required for the procedure. Based on 30 years of experience with the growth of VX2 tumors in the liver, we know that the tumors should reach a size of ~1 to 1.5 cm 10 to 14 days after inoculation which in most cases is the optimal size for treatment. CT scans were utilized to monitor the growth rate and size of the tumors.

2.2.3 Microfil Perfusion and Sample Handling

When the implanted VX2 tumors grew to the desired sizes, Microfil®, a yellow-color radiopaque compound, was perfused through the aorta at a constant perfusion rate. The liver appearance was recorded at consecutive time points and was considered complete when Microfil® could be visualized throughout the surface of the liver. The animals were euthanized then placed in a refrigerator for 4 hours to allow the Microfil® to solidify. The livers were excised and fixed in buffered formalin.

2.2.4 Micro-CT Acquisition

Specimens were scanned intact using a Siemens Inveon micro-CT scanner on the whole livers. Multiple resolution scans were designed to produce accurate microvasculature by extending the detained vasculature from the tiered micro-CT volumes.

3 Results

Figure 5 (a) shows the liver lobe has an evenly pale appearance. The blood inside the liver lobes was flushed out by a warmed normal saline mixture solution. The solution is a mixture of heparin, lidocaine and albumin which prevents blood clotting and vessel contraction and maintains the blood pressure and keeps the pathway open. Figure 5 (b) indicates the appearance of the same liver from Figure 5 (a) after switching the perfusate to Microfil® (MV-122, Flow Tech Inc). It shows the Microfil® is evenly distributed on the liver surface indicating the contrast media has been well perfused through the hepatic arteries and filled in the arterioles successfully. Microfil® perfusion has been performed on three rabbit livers which were harvested entirely shown in Figure 6. From the liver appearance on these three liver samples in Figure 6, Microfil® exuding out of vessels is clearly observed in the sample of Figure 6 (c).

To solve the conflict between micro-CT FOV and resolution, we cut the liver apart into lobes as shown in Figure 7 (b) for median-high resolution micro-CT scans. Small portions from the margin shown in Figure 7 (c) and surface shown in Figure 8 of the lobes are cut off for high resolution micro-CT scans.

The whole liver sample was scanned under 195.8 μm resolution in order to visualize the whole geometric vasculature. Figure 9 displays the 3D volume visualization of three liver samples. The left column of Figure 9 shows the 3D volume rendering of the liver samples with more liver tissue information; the right column shows 3D visualization of the vascular network structures.

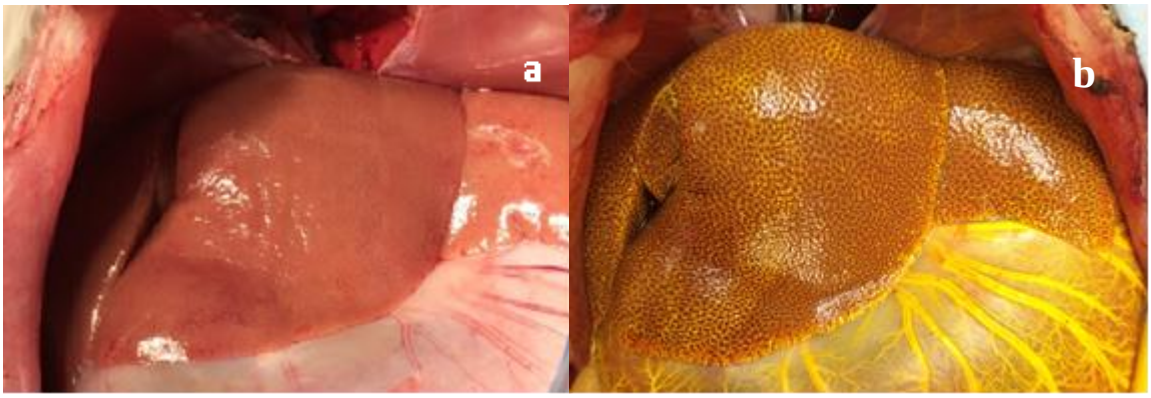

Figure 5. The surface appearance of a liver while perfused by Microfil®: (a) The blood was well flushed out and the liver appeared pale including the marginal regions which are ready for Microfil® perfusion; (b) The surface appearance of the Microfil® perfused liver in which Microfil® is evenly distributed.

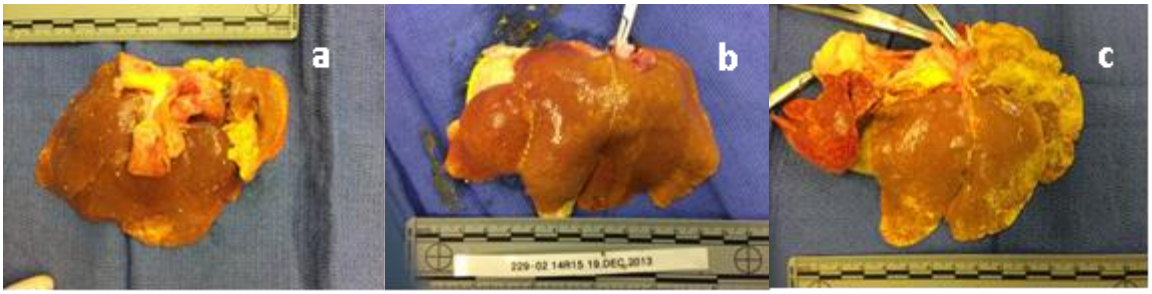

Figure 6. Demonstration of the harvested liver samples: (a) Liver sample 1 with Microfil® portal vein perfused (b) liver sample 2 with Microfil® hepatic artery perfused, and (c) liver sample 3 with Microfil® hepatic artery perfused

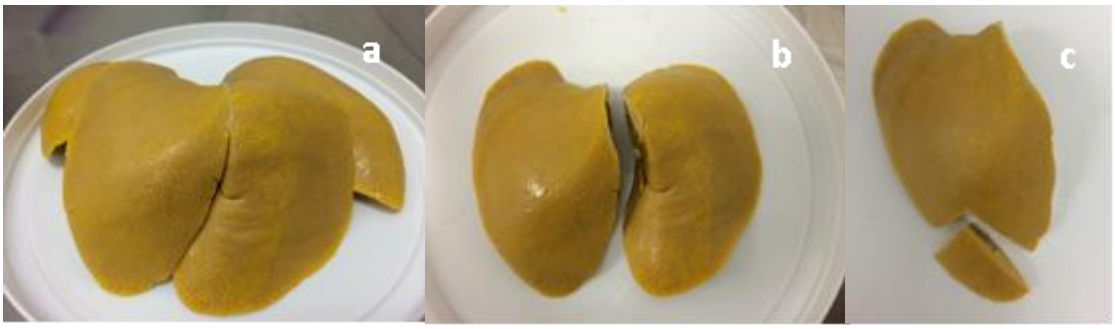

Figure 7. Illustration of the lobe's dissection pan for tiered resolution micro-CT scan: (a) Liver sample 2 appearance after fixed by Formalin (b) lobe dissection for tiered resolution Micro-CT scans, and (c) marginal block dissection for high resolution Micro-CT scan in order to accommodate the FOV restriction

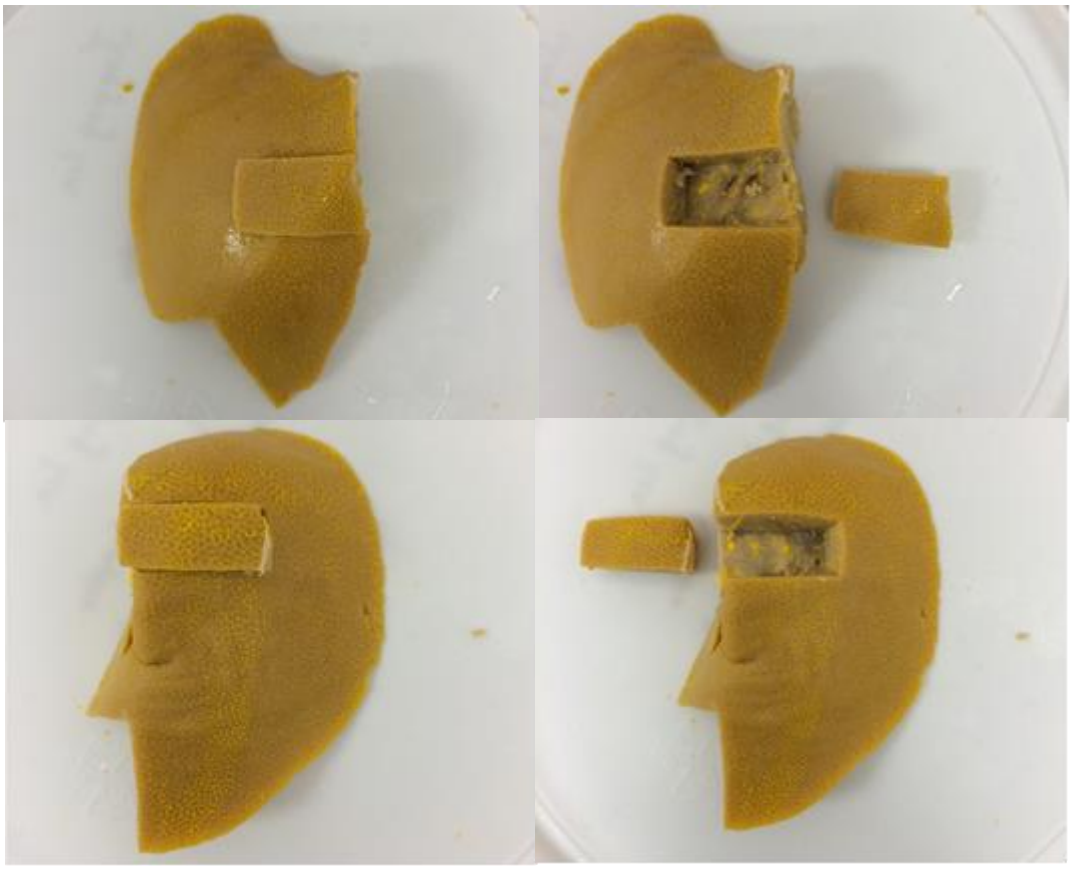

Figure 8. Illustration of the dissection plan on the individual lobe for high resolution micro-CT scans

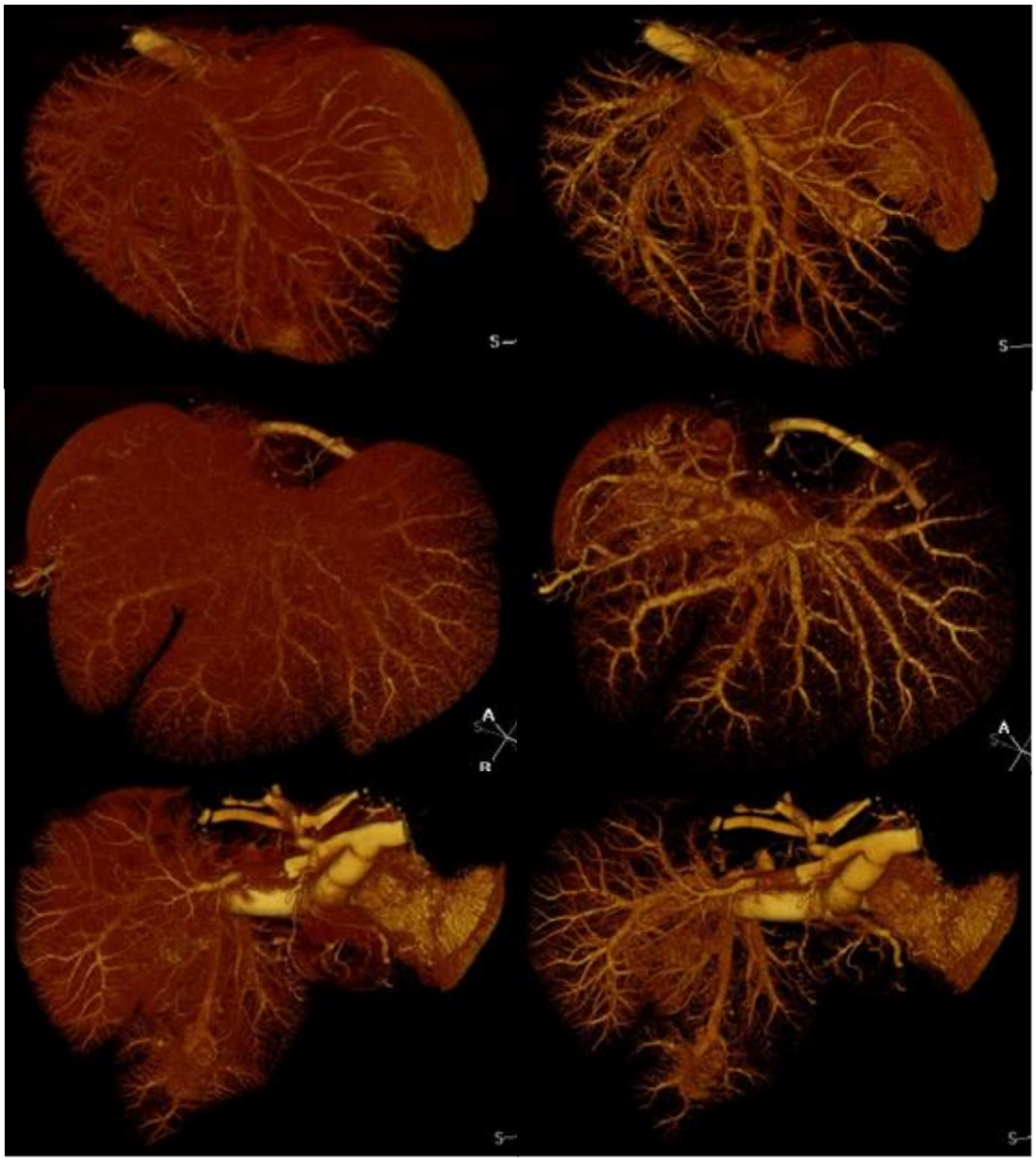

Figure 9. 3D volume visualization of three liver samples: column 1 shows the 3D volume rendering of the liver samples with more liver tissue information; column 2 shows 3D visualization of the vascular network structures.

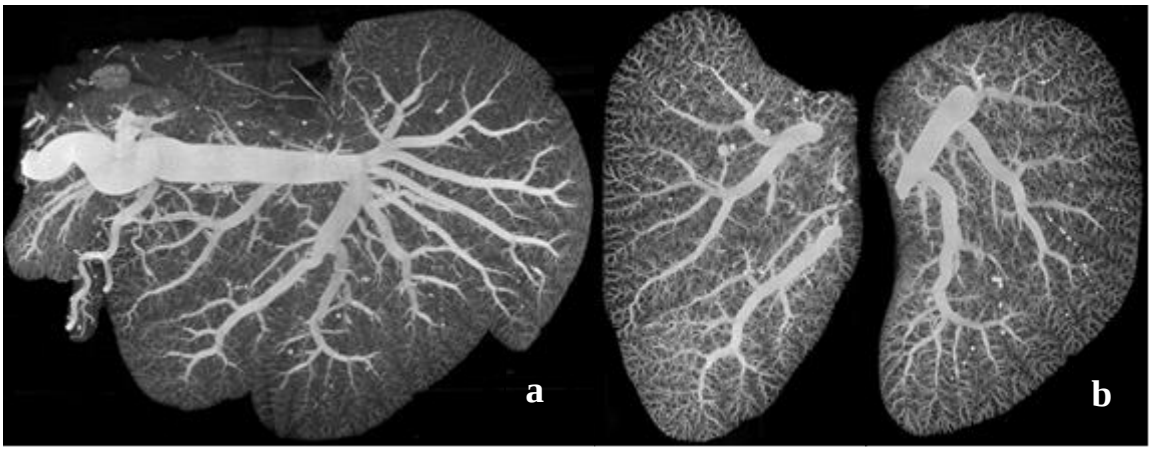

Figure 10. Maximum intensity projection views (a) on the entire liver sample from 195 μm micro-CT images and (b) on left and right individual lobes from 57.6 μm micro-CT images

The left and right lobes from liver sample 2 were scanned using 57.6 μm micro-CT scan. Scans with resolutions up to 19 μm were applied on the partial liver volume chosen from the top and bottom portions of the lobes to acquire the microvasculature detains.

The complete, intact liver for sample 2 scanned at a coarser resolution of 195 μm under micro-CT was chosen for the later 3D vascular reconstruction. The maximum intensity projection (MIP) view of the micro-CT images was generated shown in Figure 10 (a) as a reference of the vasculature at the physiological status. The major left and right lobes were scanned at a finer resolution 57.6 μm and the MIP views in Figure 10 (b) were generated from the corresponding micro-CT volumes. As the resolution is increased, the details of microvasculature are more visible.

Figure 11 shows the dynamic perfusion of Microfil® into the VX2 nodule. Based on the surface appearance of the liver with VX2 during the perfusion process, the Microfil® was observed to preferentially concentrate in the tumor first. The tumors show the tortuous arrangement of blood vessels on the surface. The micro-CT images clearly show that the peripheral aspect off the tumor is more hypervascular than its central portion. As shown in the sequence of images in Figure 11, the experimental observation can be interpreted as an analogue for embolization, i.e. the embolic agents after injection into the artery preferentially congregate to the tumor-feeding vessels due to the enhancement of blood perfusion.

The whole VX2 livers were scanned intact with a Siemens Inveon micro-CT scanner at a resolution of 97.9 μm. Scans at a higher resolution down to 35.8 μm were performed on lobes with tumors. Figure 12 shows a collection of 3D volume rendered views on the microvasculature of a VX2 nodule from the VX2 liver sample 2. The center of the nodule does not contain vessels indicating necrosis. The entire nodule is encompassed by the irregular and disordered vasculature.

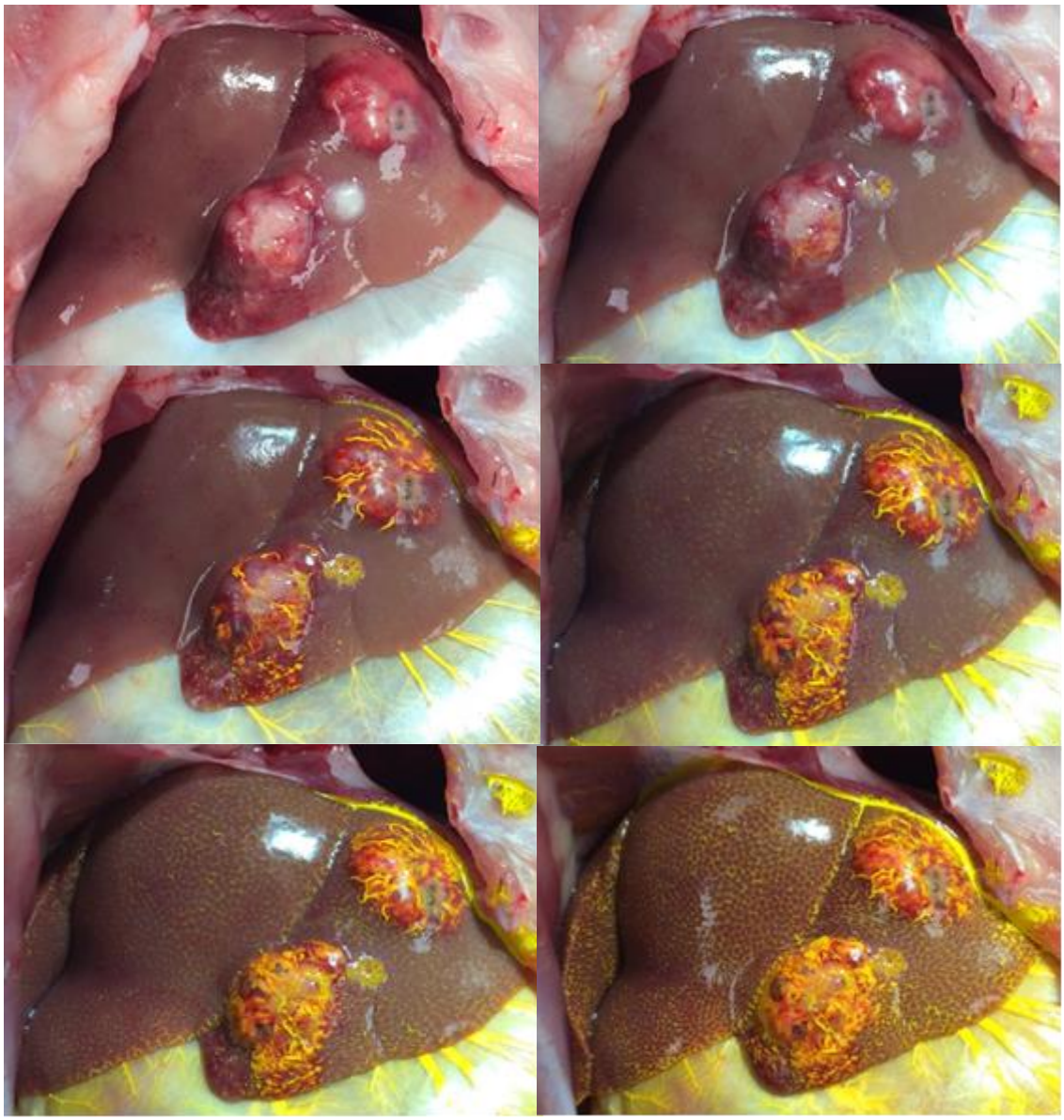

a	b
c	d
e	f

Figure 11. The VX2 liver surface appearance during Microfil® perfusion (a) after perfusing the cleaning solution 10 mins (b) after perfusing Microfil® 2 mins (c) after perfusing Microfil® 5 mins (d) after perfusing Microfil® 10 mins (e) after perfusing Microfil® 15 mins, and (f) after perfusion Microfil® 20 mins. A constant perfusion rate of ~20-30 ml/min is set on the pump

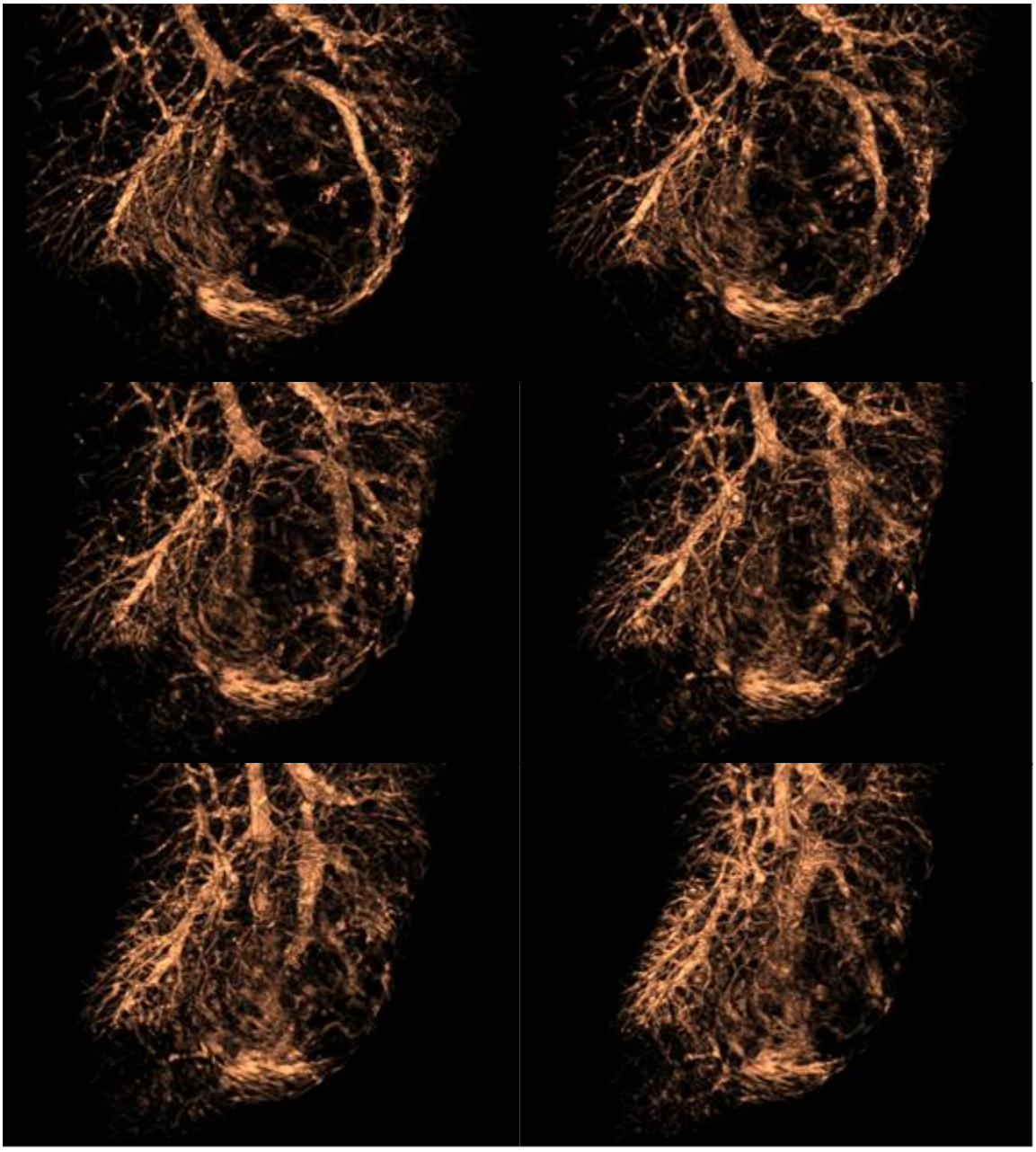

Figure 12. A collection of 3D volume rendered views on local tumor microvasculature

4 Discussion

Since the liver has dual blood supply, for the first object, Microfil® was perfused through the celiac artery by continuous syringe injection while simultaneously perfused via the portal vein by a peristaltic pump. Based on the blood proportion between the hepatic artery system and the portal vein system, the manual syringe injection was maintained at approximately 20 ml per minute and the pump through the portal vein was set to approximately 60 ml per minute. Only the portal vein system was perfused since the syringe encountered high pressure which stopped the perfusion. It may be due to the hepatic arterial buffer response (HABR) [72], a unique mechanism, or it may represent the ability of the hepatic artery to produce compensatory flow changes in response to changes in portal venous flow. If portal blood flow is reduced, the hepatic artery dilates, and the hepatic artery constricts if portal flow is increased [73]. One reason for this could be due to the pre-set proportion on the portal venous flow rate being higher than the hepatic artery flow rate, and this increased portal flow causes the hepatic artery to constrict. The viscosity of Microfil® makes it difficult to depress the syringe's plunger, which may be another reason for decreased flow within the hepatic artery. For the second and third objects, single perfusion through the aorta was performed via the pump with a constant flow rate. Note that the high viscosity of Microfil® causes it to build up within vessels and leads to resistance and breakage; therefore the Microfil® was perfused by a peristaltic pump with a constant, but much lower flow rate of approximately 30 ml per minute, rather than the normal rabbit aorta flow rate of approximately 70 ml per minute. Few areas in Figure 6 (a) and (c) show the leakage of Microfil® into the

parenchyma which may be due to the local resistance built up by the high viscosity of Microfil®. Figure 13 indicates the relation between the working window time of Microfil® and the percentage of MV-Curing Agent volume in the mixture, the MV-Compound and MV-Diluent, with 1:1 volume ratio. The test was conducted at room temperature. The dashed line is the polynomial curve fitting on the experimental data which was collected when the mixture turns from thin to nectar-like thickness.

Because our purpose is to establish a network of hepatic arteries with a coherent vascular structure and sufficient anatomical details of the blood vessels to characterize the efficacy of embolotherapy, we took a sample treatment method that preserved the tissue to maximize the physiological position of the vascular structure and at the same time fixed the vascular structure. We found that, using the fixing method provided by the Microfil® tool kit caused the overall size of the physical sample to shrink, thereby affecting the accuracy of the structure. We put the Microfil® cured sample into formalin to fix the tissue and scanned the whole liver to obtain a relatively low-resolution micro-CT image that was later used to register the left and right hepatic lobes back to the physiological status. Then, the left and right hepatic lobe were separately subjected to micro-CT scanning to obtain respective medium-high resolution images for further modeling.

It is noted that the degree of image-based reconstruction on the details of vasculature is limited by the size of the sample. Larger blood vessel networks can be directly captured from images via the imaging systems. Small-sized samples, such as samples from experimental mice or rats, can be reconstructed with focal microscope

images and can be reconstructed with very detailed structures. If keeping the sample intact to maintain the consistency of the sample structure, only certain vessels among the network can be reconstructed for the overall image reconstruction of the sample. Moreover, when reconstructing through imaging, the degree of reconstruction generally selects a cut-off of the degree of reconstruction is usually selected to ensure the accuracy of the measurement on objects, which limits the extent of the reconstruction of the network structure. The retention of blood vessel details also depends on the processing of the sample. Both the corrosion casting and the histological sections have the disadvantage of losing detail or causing inconsistency.

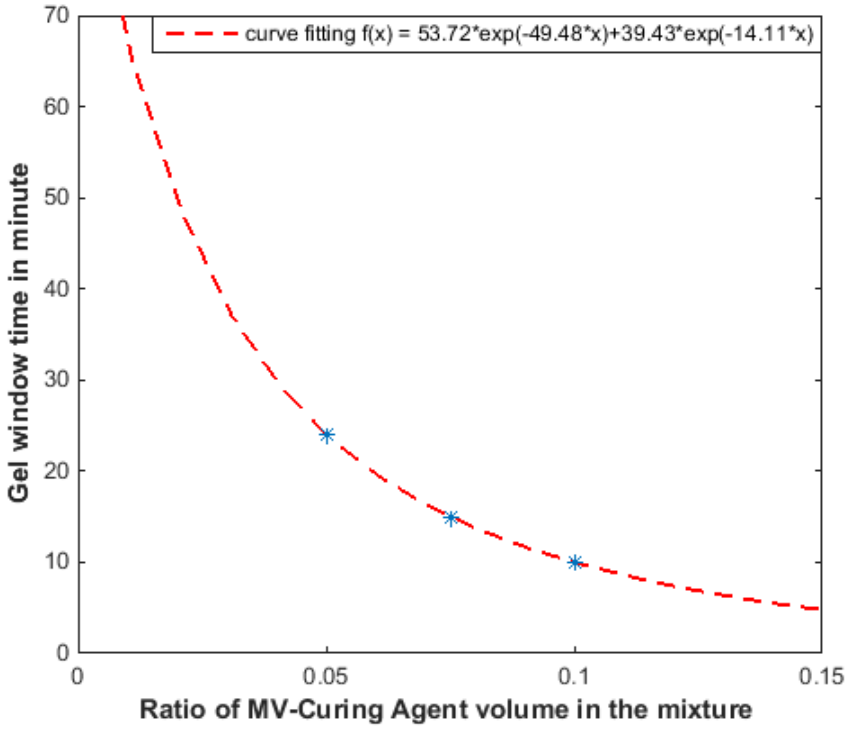

Figure 13. Microfil® working time plots on the volume percentage of MV-Curing Agent in the mixture

CHAPTER 3 THREE-DIMENSIONAL MODELING OF HEPATIC MICROVASCULATURE NETWORK BASED ON MICRO-CT IMAGES

1 Background

Embolotherapy plays an essential role in the management of unresectable hepatocellular carcinoma. Taking advantage of the hypervascular characteristics of HCC [74], embolotherapy is to introduce embolic agents into hepatic arteries via a catheter and attempt to block the tumor-feeding arteries and further allow chemoembolization or radioembolization to be delivered to the tumor locally. Targeted embolization is subject to the extent that embolic agents can be transported to the tumor-feeding arteries and lodged near the tumors. Due to the limitation on monitoring blood dynamics during embolization, the influence of embolic agents on local hemodynamics near tumors is not well-understood. Additionally, the avoidance and detection of non-targeting embolization [75] is also a big concern for radiologists. Non-target embolization may be unavoidable due to the complex vasculature and the uncontrollable blood flow near the tumor, resulting in serious complications [76].

During the procedure, the distribution of embolic agents in the arterial system is influenced by various factors that may be introduced either from contrived interference or the interaction among microspheres and blood flow resulting in altered local flow dynamics. Understanding the hemodynamic effects of these factors and how they interact

is the key to linking these complicated situations to treatment outcomes. Utilizing computational analysis and simulation of the particle-hemodynamics inside the hepatic vascular models is a feasible approach by which to investigate the hemodynamic influences by catheter placement [77,78,79,80,81,82,83,84,85,86], microsphere characteristics (type [77,87], size and quantity [83,85]), catheter type [88,89,90], microsphere injection techniques (injection timing [77,80], velocity [78,79,80,81,84,87,91], and interval [80,81]), and other factors. The simulation studies can be used to identify the impact of these factors on microsphere transport and distribution. Furthermore, it can reveal potentially the preferential settings on downstream targeting embolization.

One of the key components of reliable computational modeling for hemodynamic simulation is a geometric domain in which physiological boundary conditions can be applied to match the simulation-specified flow conditions. A geometric domain also called geometric configuration, computational domain, or mathematical model is defined as a three-dimensional (3D) vascular geometry. Basciano et al. [77] first created a representative hepatic artery system in which the arterial geometry represents the most common anatomical configuration from the averaged population. The model originates from a common hepatic artery (CHA) and bifurcates into a gastroduodenal artery and a proper hepatic artery which splits into a left and a right hepatic artery. The model ends one level further after the left and right hepatic artery with two daughter outlets for each. It has been deployed in investigating the optimal catheter positioning and controlled release toward liver tumor regions. Based on the definition of according to Couinaud's

hepatic segmentation, Aramburu et al. [85] who created a literature-based healthy liver model in which consists of the proper hepatic artery (PHA), which then divides into the right and left hepatic arteries (RHA and LHA), and further splits into 29 segmental and subsegmental branches, perfusing the 8 segments of the liver. It has been used for studying the effects of catheter type [88] and the role of the microcatheter distal direction and microsphere injection point and velocity [84]. In order to understand the microsphere distribution, it is necessary to include the downstream vascular structure while maintaining this geometry and detail. The patient-specific vascular model derived from images may provide the geometric information. Basciano et al. [78,80] used the patient-specific vascular model based on the CT images which originates from the SMA and has two downstream outlets LHA and RHA due to the limited image resolution of the imaging system. A vascular growth simulation [86] has been applied on a patient-specific model initialized from the main vessels extracted from angiography. The model simulates the growth of the hepatic arteries with the constraint of the liver contour acquired from arterial phase CT images. When a malignancy is present, the vasculature growth will be denser and more irregular. The vessel simulation assumes the vascular tree is a binary tree in which each vessel segments is represented as an ideal, rigid tube with fixed radius, wall thickness, length and position. A hepatic vascular model was built based on a healthy human liver discarded from a failed transplantation. Its vascular architecture was achieved by a combination of different techniques, namely, vascular corrosion casting, micro-CT scanning and image processing [92, 93]. A human liver vascular corrosion cast was obtained by simultaneous resin injection in the hepatic artery (HA) and portal vein

(PV). A high resolution (110 μm) micro-CT scan of the total cast allowed gathering detailed macrovascular data. Although this model of the human hepatic artery system is very rare and differs from the previous truncated arterial models, it is very difficult to obtain high-resolution vessel images covering the entire liver even using micro-CT.

These vascular models based on human hepatic vascular anatomy can better ensure clinical relevance. However, clinical imaging systems have the inherent limitation that if the objects are below the system's ability to be faithfully reproduced on an image, they are either not noticeable or blurred out [94]. Given the size and volume of a regular human liver, the dimension of the vessels covers a large range. When the vascular tree bifurcates, the size of the vessels decreases as the depth of the tree increases. That is, the reality is that the major vessels can be well detected through the clinical imaging systems and constructed into the vascular models but not the vessels that are near or below the system capability. The detailed morphologic information obtained from clinical images is only involved in the major structures and from which the vascular models derived are the truncated arterial structures to avoid the small and blurred structures with inaccurate measurements. Simulated vascular structures based on realistic structures have been employed to supplement the missing vascular structure that has not been captured by imaging systems. However, they are not a substitute for real vascular structures and there is no way to verify the actual liver measurements.

A computer model based on the hepatic vascular network is expected to study the computational flow dynamics within the vascular structures while the microspheres as embolic agents are transported through the arteries. The microspheres most used in a

clinical setting are compressible and range in size from 40-300 μm. Therefore, a 3D hepatic vascular network model with detailed structures derived from anatomic geometry is necessary for studying the dynamics of the blood flow through vascular structures with diameters ranging from several millimeters to 40-50 μm.

In this chapter, we propose to construct a 3D hepatic microvasculature model based on the Micro-CT images of a rabbit liver covering the intact hepatic arterial trees down to arterioles. First, a contrast-filled tissue sample is established by selecting the commonly used pre-clinical animal model to ensure faithful vascular structure, and the sample is processed to meet the requirement of a detailed and coherent vascular network. Then multi-resolution micro-CT images are used to describe the microvasculature, by handling the vasculature in each individual liver lobe and registering them back to the entire liver to achieve fidelity and detailed spatial vasculature under physiological conditions while overcoming the limitations of the imaging system. Finally, the vascular modeling method including vascular segmentation, vascular centerline extraction, is used to automatically generate the vascular network.

2 Materials and Methods

A micro-CT scan of the whole liver sample 2 acquired at 195.8 μm was used as the reference of the spatial vascular structures. The individual micro-CT scans at 57.6 μm on the left and right lobes were used to extract the vasculature and its radii for reconstructing the vascular model later.

2.1 Segmentation

A two-steps segmentation is proposed to segment the vessels with wide peak intensities. First, an intensity threshold at full width at half maximum (FWHM) of the main branches, ε, is adopted to ensure the dimension accuracy on moderate sized vessels. Secondly, in order to only capture the reduced peak vessels, a method based on the first derivative to find the local maxima among the intensity below ε is employed.

The intensity threshold ε at FWHM of the main branches is easy to determine by averaging the means of the liver and vessel intensity populations. All pixels above ε are grouped into 0. Pixels with intensity below ε and above a given threshold are grouped into a candidate pool marked as -1.

Before the segmentation is applied, the volume is convolved with a 3*3*3 window with the reverse of the distance as the weights to smooth the intensity noise in the following manner: $I = \frac{\sum_i \sum_j \sum_k W(i,j,k) I(i,j,k)}{\sum_i \sum_j \sum_k W(i,j,k)}$, where $w(i,j,k) = \frac{1}{||\, q(i,j,k)\, ||}$. w denotes the weight inside the convolution window, q denotes the position inside the window, and $||\, q(i,j,k)\, ||$ represents the relative distance to the window center.

The characteristic of vessels with intensity below FWHM is that there are not enough pixels to form a plateau on the cross-sectional profile. We assume that the intensities on the orthogonal cross-section of the vessel have the Gaussian profile, disperse from the center, and with the maximal intensity value at the center.

$S = \left\{ p \middle| argmax_{p,q}\big(I(p)M(q)\big), with\ q\ is\ center, p \in \mathbb{R}^3 \right\}$ where M is a mask at orthogonal cross-section plane, p is the 3D coordinates of the voxels, and q denotes the

corresponding location inside the mask. *S* denotes the 3D coordinates set of voxels that are the local intensity maxima at an arbitrary cross-section plane. Suppose the *S* is derived from the orthogonal cross-section planes, then the vessel should lay on the orthonormal plane of the orthogonal cross-section plane. To simplify the process on finding the orthogonal cross-section plane, we choose the three Cartesian planes to locate the mask. At the cross-section plane, the local intensity maximum is still detected as the intensities increasing from all directions to the peak at the center. However, there must have a deviation on the intensities along the corresponding orthonormal plane.

$\varphi = \{D_{xyz}I(p)|p \in S\}$ where D represents the derivative operators and φ represents the set of intensity derivatives from the voxels with the local intensity maxima along their orthonormal planes. The standard deviation of φ denotes as σ that is used to form the segmented voxels set τ.

$\tau = \{p|\ D_{xyz}^{-x}I >=0,\ D_{xyz}^{+x}I>=0,\ D_{xyz}^{-y}I>=0,\ D_{xyz}^{+y}I>=0,\ D_{xyz}^{-z}I >= -\sigma,\ D_{xyz}^{+z}I>= -\sigma\ \} \cup \{p|\ D_{xyz}^{-y}I >=0,\ D_{xyz}^{+y}I>=0,\ D_{xyz}^{-z}I>=0,\ D_{xyz}^{+z}I>=0,\ D_{xyz}^{-x}I >= -\sigma,\ D_{xyz}^{+x}I>= -\sigma\ \} \cup \{p|\ D_{xyz}^{-x}I >=0,\ D_{xyz}^{+x}I>=0,\ D_{xyz}^{-z}I>=0,\ D_{xyz}^{+z}I>=0,\ D_{xyz}^{-y}I >= -\sigma,\ D_{xyz}^{+y}I>= -\sigma\}$

where p denotes the 3D coordinators of voxels, $D_{xyz}I$ used here is the forward and backward derivative operators on the intensity at p. The backward and forward derivatives capture the local maxima in the given cross-section planes. τ denotes a 3D coordinator set of voxels that are the local maxima inside a cross-section plane with the derivative along the orthonormal plane within a threshold. That would give good segmentation estimation among the voxels below the FWHW threshold.

The segmentation function f is summarized in the following set:

$$f(p)\begin{cases} 0, & I(p) \geq \varepsilon \\ 1, & \delta \leq I(p) < \varepsilon \text{ and } p \in \tau \\ -1, & \delta \leq I(p) < \varepsilon \end{cases}$$

ε denotes the FWHW intensity of the major vessels, δ gives a much lower intensity threshold. Among the $[\delta, \varepsilon)$ intensity range, the voxels that belong to the τ set are marked as 1. All voxels that are categorized into 0 and 1 will be used for further process.

2.2 Center Point Extraction

To construct a 3D vascular model, the complex vascular structure needs to be represented into some simplified data structure. The centerline along the medial axis of the vessels can be sampled and structured into a series of medial points' positions in 3D with their corresponding radii. Along with the connectivity information among those centerlines, the centerlines can preserve the hierarchical vascular tree in a natural manner. A centerline extraction method is designed to fulfill these requirements through two functions, the arrival time function $T(v)$ and the distance potential function $P(v)$, applied on the segmented voxels. v denotes the voxel with 3D position variables.

The arrival time function $T(v)$ is a function to acquire the arrival time for each voxel v if a wave starts from the given root and travels inside the segmented vascular tree. Begun at a source, a voxel at the root of the vascular tree, a wave emanates in all directions and propagates inside the segmented volume set. Through the arrival time

function, the segmented vascular tree S can be represented by a collection of voxel sets given a certain time step Δt as the following set:

$S = \{V_i | T(v) \in [t_0 + i * \Delta t, t_0 + (i+1) * \Delta t),\ for\ i = 0,1 \ldots \max(T)\}$, where V_i is a voxel set with $T(v)$ within a certain time range $[t_0 + i * \Delta t, t_0 + (i+1) * \Delta t)$. t_0 is the arrival time at the root, usually is set to 0. The arrival time function remains the connectivity feature in the longitudinal aspect as a discrete manner stored inside each voxel. It can be considered for acquiring the connection relation among medial points and centerlines after their extraction.

The distance potential function $P(v)$ is a function to obtain the distance for a voxel to the closest segmented surface. Instead of a single voxel as the root in the arrival time function, the distance potential function $P(v)$ regards the segmented surface as the source collection. After the source emanates waves in all directions inside the segmented lumen, the distance potential function $P(v)$ preserves the transverse information that can be utilized to obtain the medial point position as well as its radius.

Given a set of voxels $V_i$within a time range $[t_0 + i * \Delta t, t_0 + (i+1) * \Delta t)$, V_i can be represented by a collection of voxel sets distinguished by the distance potential function as the following set:

$V_i = \left\{ V_i^k | P(V_i) \in [d_0 + k * \Delta d, d_0 + (k+1) * \Delta d),\ for\ k = 0,1 \ldots \max(P(V_i)) \right\}$.

Within a given V_i, several transverse vessel segments may be involved as the wave spreading to all direction in the arrival time function. The medial points existing in all of the transverse segments among V_i can be easily found through their local maxima $argmax_v(P(V_i^k))$.

The arrival time function $T(v)$ and the distance potential function $P(v)$ can be regarded as an isosurface evolves from the source to all directions of the surface normal. The isosurface, also called the front wave, can be represented by an Eikonal equation

$\|\nabla U\| = \frac{1}{F}$ where U is the minimal action function and F is the speed of the evolution function. The discrete solution to the Eikonal equation is found by solving the scheme

$$\left(\max\{u - U_{x-1,y,z}, u - U_{x+1,y,z}, 0\}\right)^2 +$$

$$\left(max\{u - U_{x,y-1,z}, u - U_{x,y+1,z}, 0\}\right)^2 +$$

$$\left(max\{u - U_{x,y,z-1}, u - U_{x,y,z+1}, 0\}\right)^2 = \frac{1}{F^2}$$

The numerical method for solving efficiently boundary value problems of the Eikonal equation can be found in [95，96].

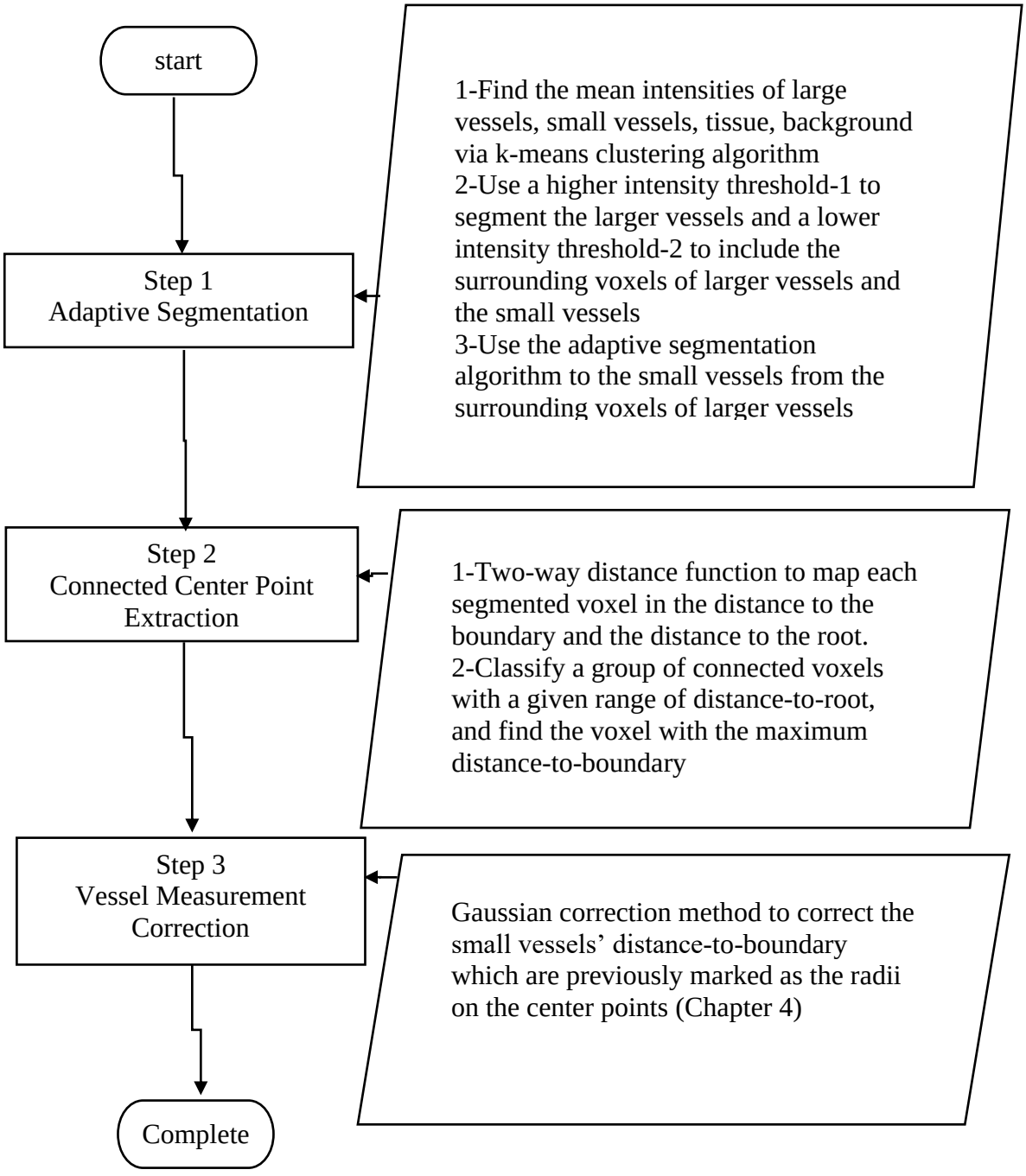

Figure 14. Flowchart of the development processes of the vascular model

3 Results

The vessel intensities at the edge of the larger vessels and on the small vessels are ambiguous and cannot be separated by a single threshold as seen in Figure 15 (b) marked in green color. As shown in Figure 15 (c) the pixels in blue color that fall in the intensity range between the half intensity threshold and the average intensity of liver tissue are segmented by the adaptive threshold. Figure 15 (d) displays the segmentation result on the vessels with a broad range of intensity. The vessels are well-segmented via the proposed adaptive segmentation method.

Displayed in Figure 16 are the numerical values of distance-to-boundary (top panel) and arrival time (bottom panel) over the left and right lobes. The values are calculated based on the segmented vasculature and represented in gray scale. The gray level shown in distance-to-boundary panel exhibits the ridge appearance that the vessel skeleton has the local maxima. In order to track the vessel skeleton, the arrival time in the bottom panel provides the sequence order of distance-to-boundary local maxima. The gray level in the bottom panel gets higher and brighter as the vessel segments approach the endpoints.

With the distance-to-boundary and arrival time functions, the centerlines are extracted and overlaid on the MIP views in Figure 17. The centerlines are well-centered on the major vessels. The details are shown in the zoom-in view of the partial area. The centerlines of complex microvasculature are superimposed intuitively on the MIP image.

Figure 18 shows the plot of the radii of center points extracted from the micro-CT images under 57.6 μm resolution on an individual lobe and their corresponding intensities. It displays that the intensity values of the center points cover a wide range. For a center point with a radius greater than 5 pixels, an obvious intensity watershed is shown, that is, the intensity value is approximately greater than 7500 arbitrary values above which all the center points with radii greater than 5 pixels can be separated. When the intensity values are less than this watershed, the radii of the center points are limited to 5 pixels or less.

In order to preserve the physiological spatial coherence, both the left and right lobes are registered back to the whole liver via the same bifurcation pairs in the individual lobe micro-CT volumes and the whole liver micro-CT volume. Figure 19 shows the registration result of the left and right lobes.

Based on the extracted centerlines, the major vessels inside both liver lobes were reconstructed individually in Figure 20 by given a unit radius for displaying the coherent vascular geometry. For the detailed microvasculature, two subtrees are reconstructed and displayed in Figure 21 using a unit radius. The radii as an important parameter in the vascular model are coded in colors and displayed on the vessels' surface at spatial locations as showed in Figure 22.

The color mapping of radii on vessel segments in Figure 22 utilizes the local maximum values of distance-to-boundary. The distance-to-boundary values are derived from the vascular segmentation. As the vessel getting narrower, the variance on the radius dimension turns unnoticeable through bifurcation.

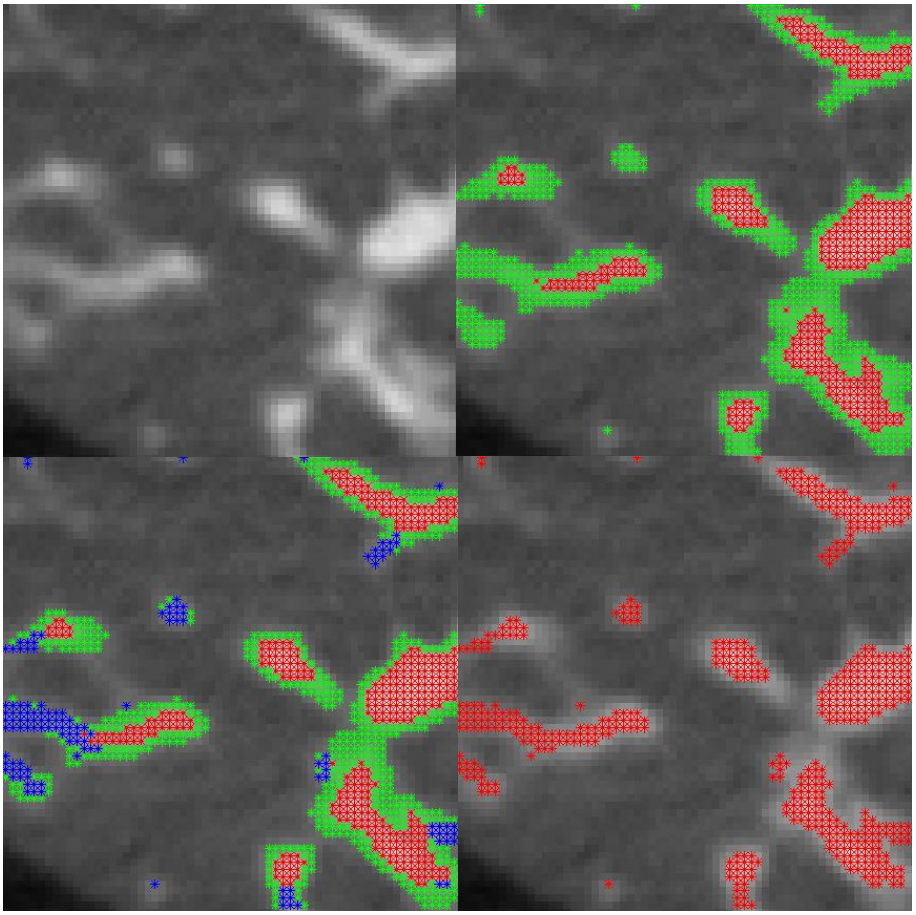

a | b

c | d

Figure 15. Illustration of the proposed adaptive segmentation. (a) original micro-CT image; (b) pixels in red color with intensities above half average intensity threshold and pixels marked in green color are between half intensity threshold and average intensity of liver tissue; (c) pixels in blue color are segmented by the adaptive threshold; (d) the final segmentation result of (a)

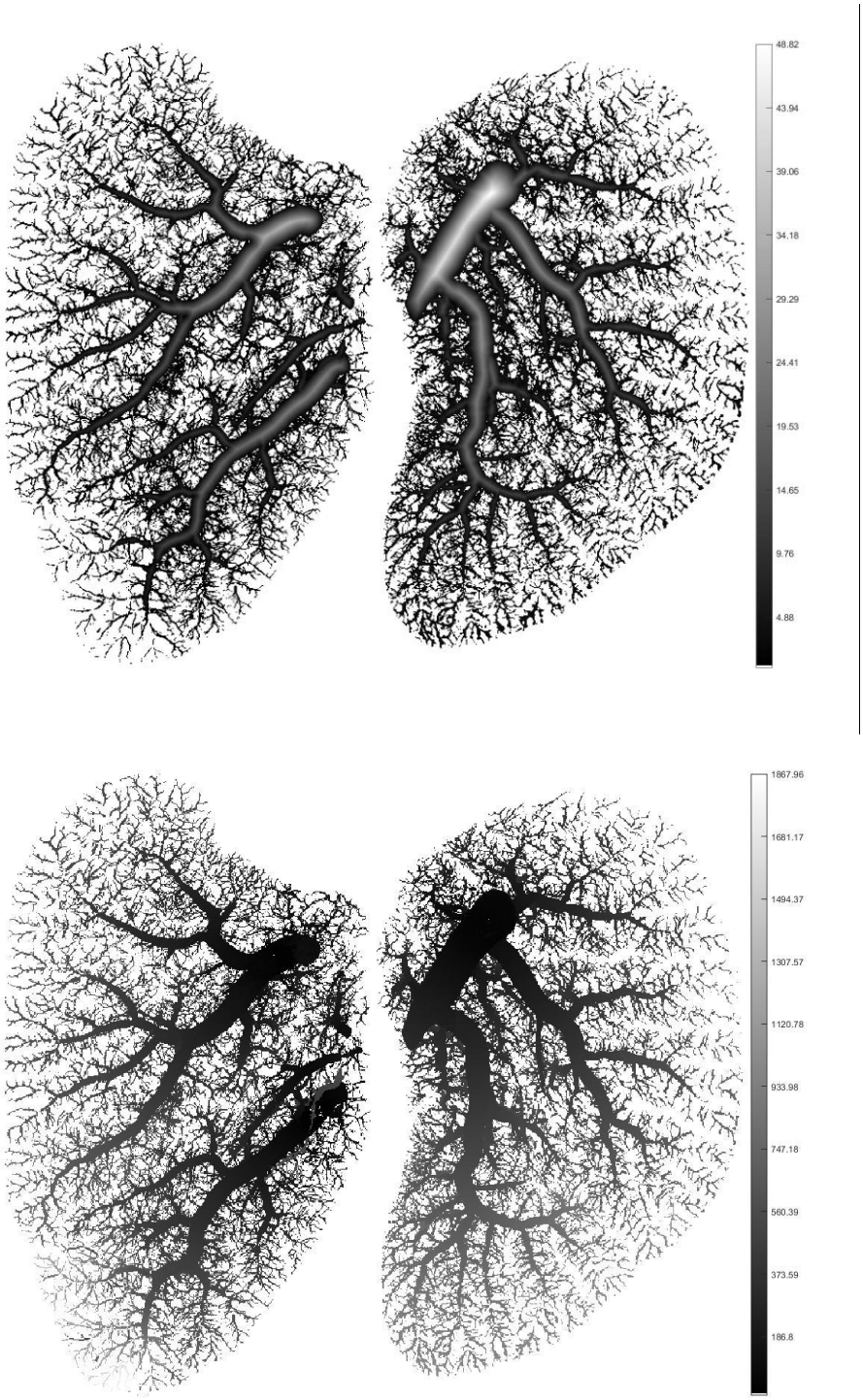

Figure 16. Illustration of the distance-to-boundary function and the wave time function

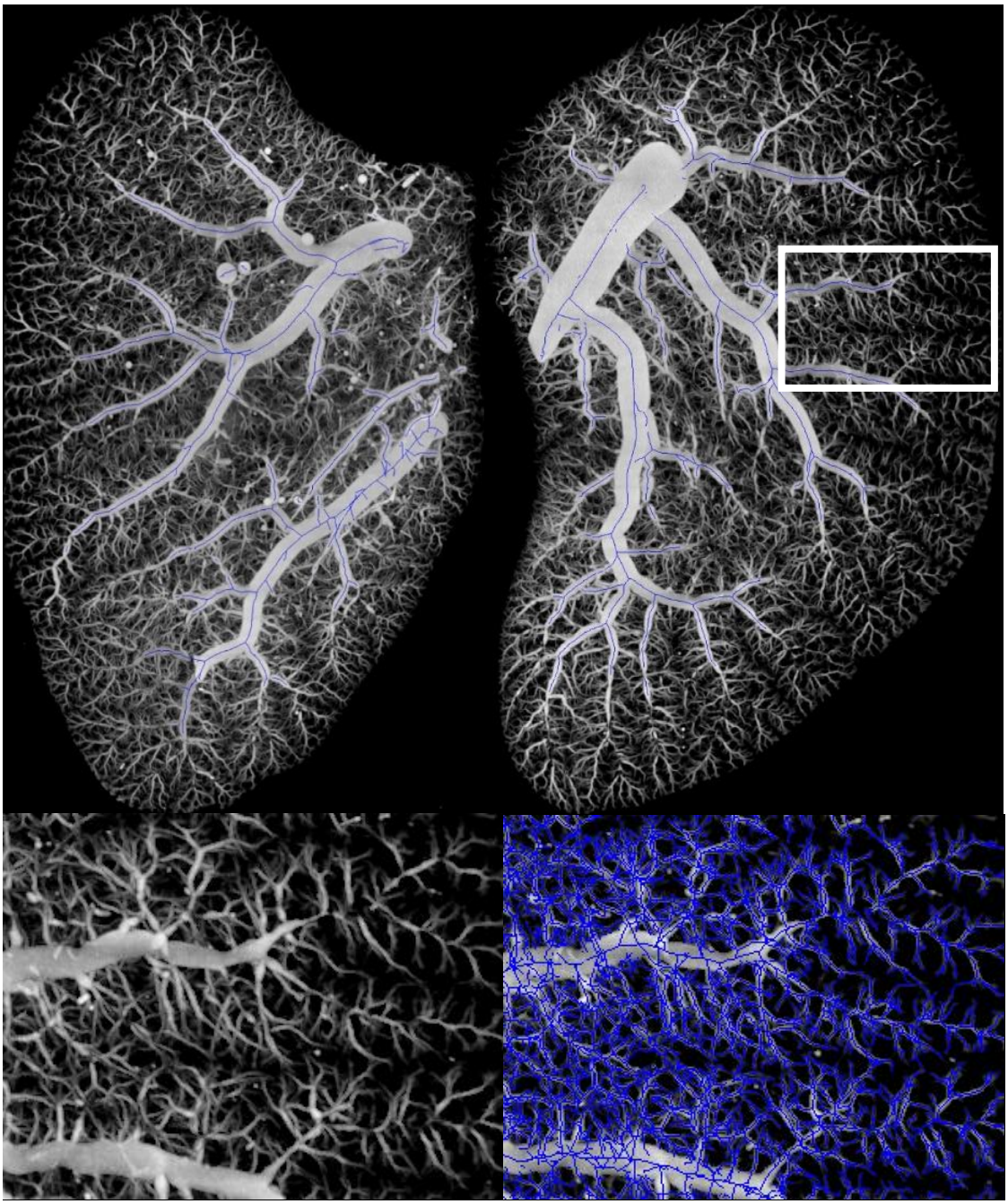

Figure 17. Illustration of the extracted centerlines superimposed on the MIP views from micro-CT volume

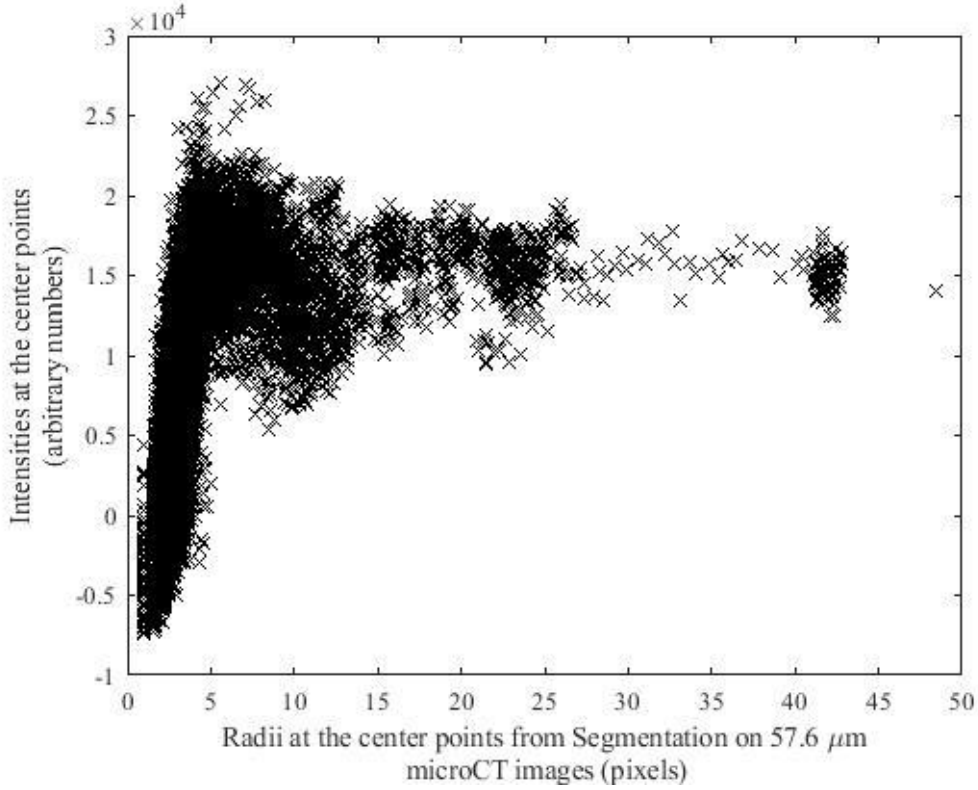

Figure 18. Intensity plots ofthe extracted center points and the corresponding radii in pixels

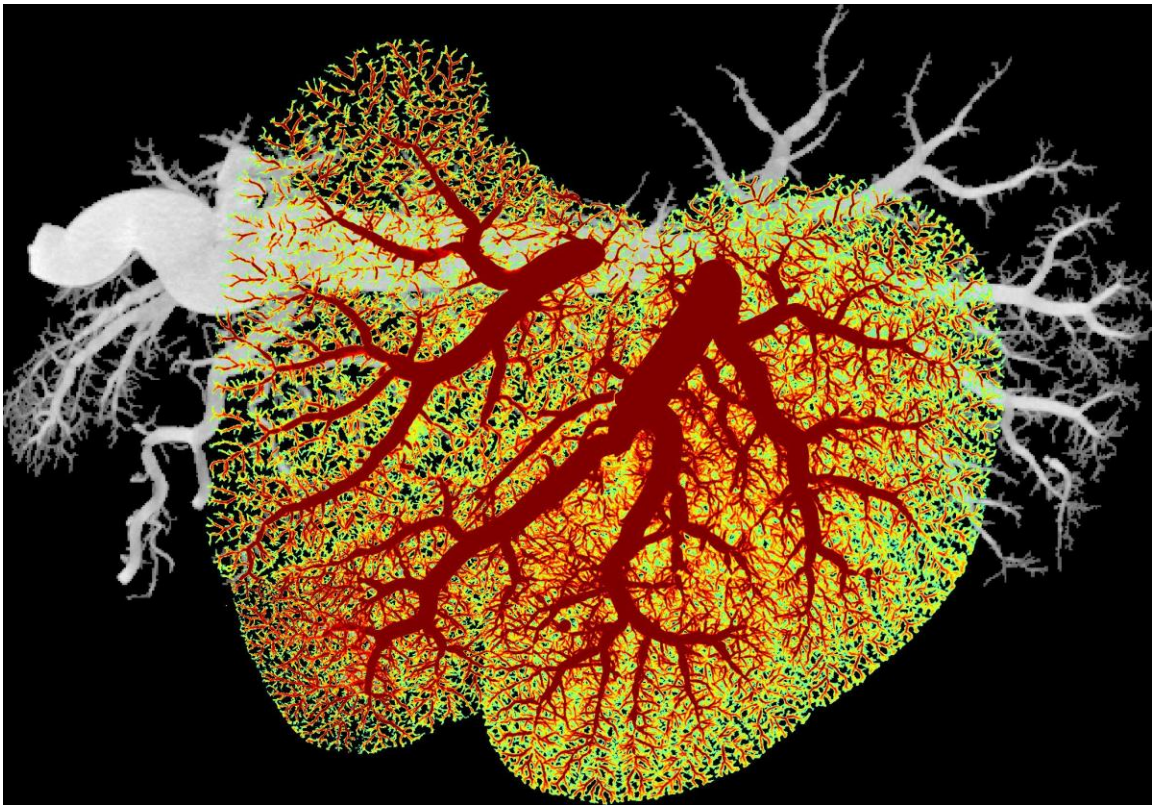

Figure 19. Illustration on registration of left and right lobes to the whole liver

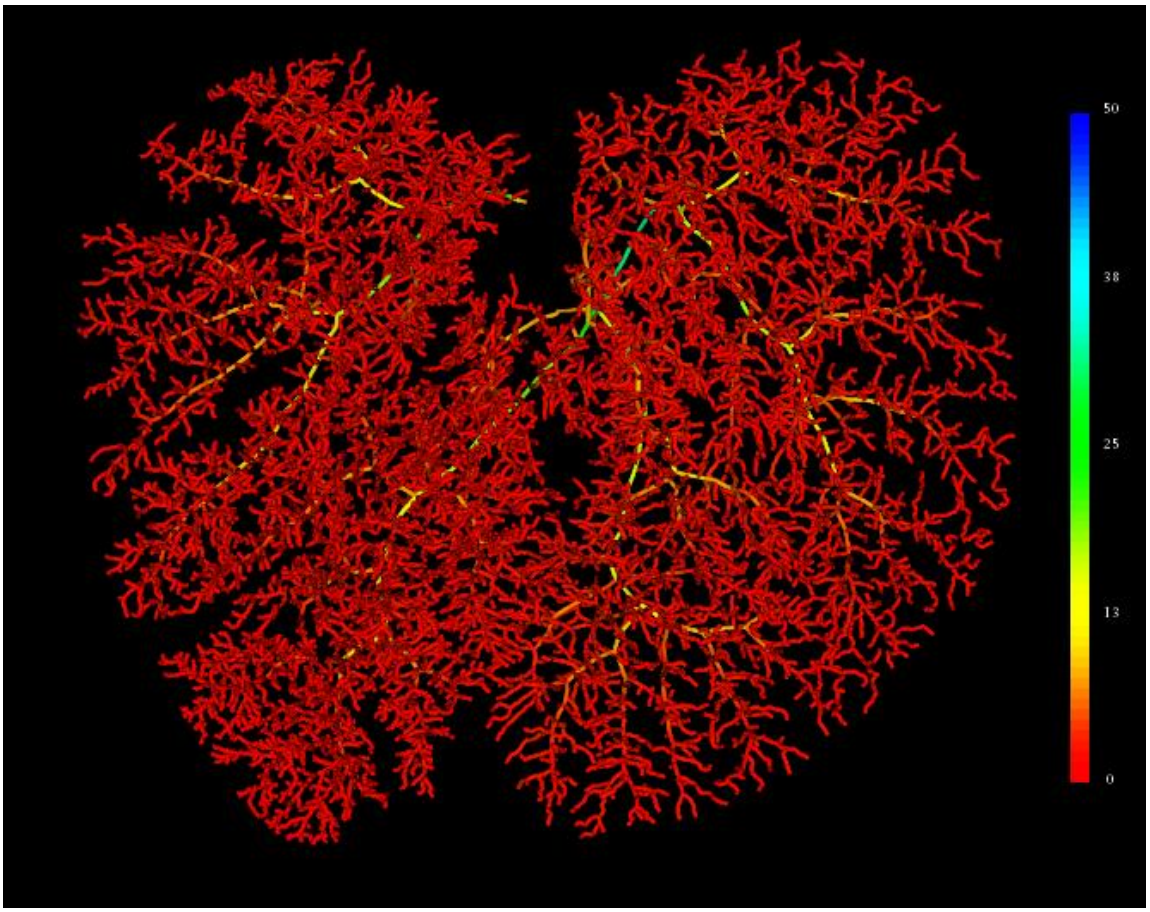

Figure 20. 3D vascular reconstruction based on the centerlines from Figure 17 using a unit radius

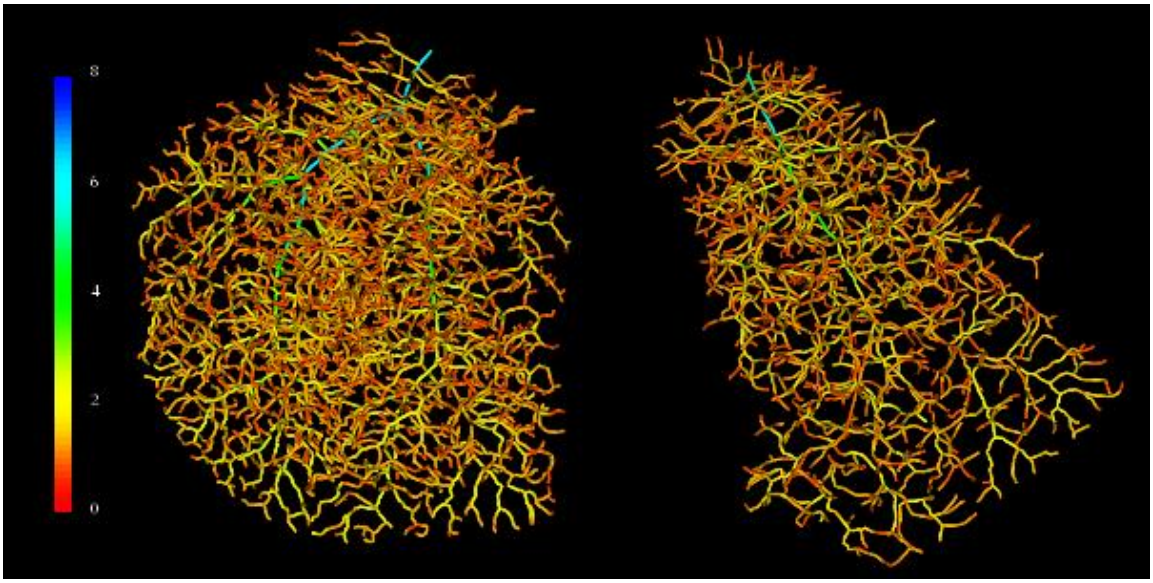

Figure 21. The reconstructed subtrees with detailed structure in a unit radius for display

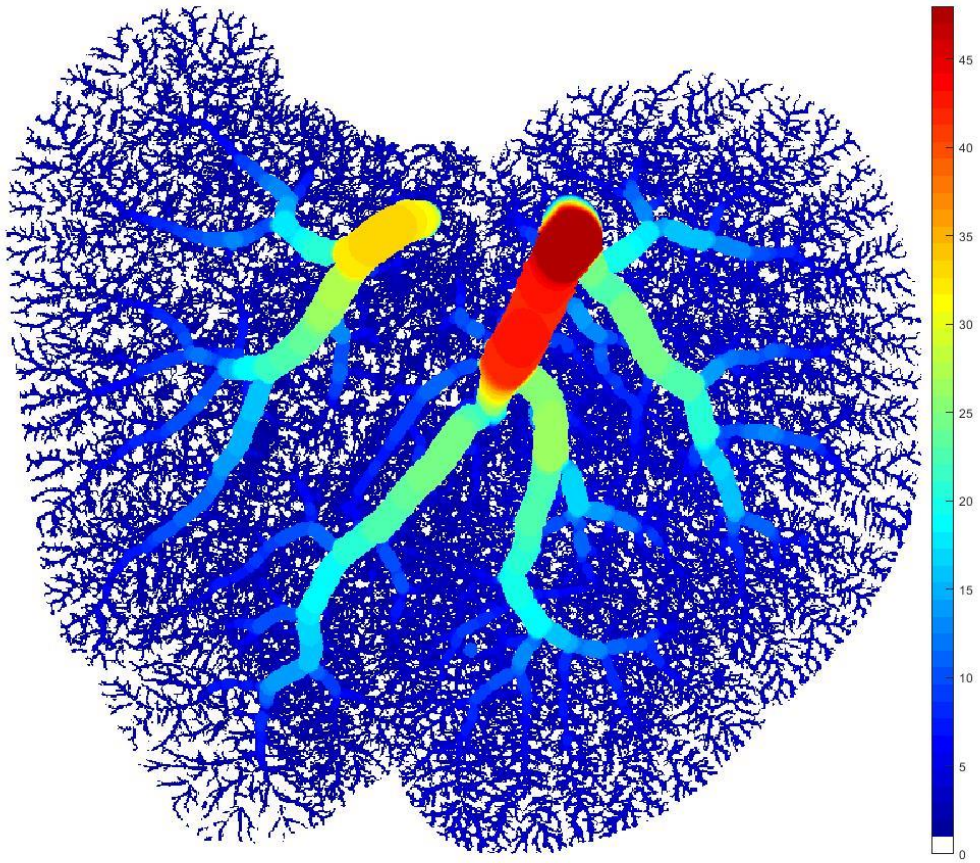

Figure 22. Color mapping on the extracted vessel radii superimposed on the MIP view of the liver lobes.

4 Discussion

For HCC patients, the extent of the retention of hepatic functionality after trans-arterial embolization plays a significant role in the prognosis. However, non-target embolization may be unavoidable due to the complex vasculature and the uncontrollable blood flow near the tumor, resulting in serious complications. Factors influencing the severity of complications related to non-target embolization include the amount of reflux material, the size and type of embolic material used, the anatomy of the organ involved (size, density and architecture of tumor micro-vessels, tumor size), and local hemodynamics (local flow, blood pressure).

The focus of this study is on constructing the 3D microvascular model for future use in blood flow analysis to assist in the administration of embolization therapy. Based on this computer model, the simulations would not only provide information regarding the blood flow dynamics within regular arteries but also the micro-flow dynamics around the tumor during embolization application. Information gathered from the simulations would help physicians understand the microspheres' transportation pattern of embolization and could lead to further development of methods to improve the outcome of embolization.

The 3D vascular domains based on human hepatic vascular anatomy that appear in the current studies of hemodynamic simulation can be subdivided into three categories according to the extent of vascular anatomic details. The first category is the synthetic vascular model in which the anatomical geometry is derived from the averaged population. The second category is the patient-specific hepatic vascular model. It only

covers the main branches based upon clinical imaging systems. It may be extended to include more details through vascular growth simulation. The hepatic vascular model based on patient-specific hepatic anatomy as the basis for flow simulation is desired. However, anatomic imaging modalities such as CT and MRI have the inherent capability on image resolution which limits the vessel down to certain dimension being imaged. Most of current hepatic vascular models used for simulating flow dynamics are truncated to the main branches. However, the vessels that microspheres are targeting may not be captured from CT images. The third category is the realistic hepatic vascular model obtained from a healthy human liver. This model of human hepatic artery system is very rare since it is very difficult to obtain high-resolution vessel images covering the entire liver even using micro-CT. In addition, the vessel branches are easily lost on the microvasculature due to the fragility of the casting material. With such high resolution, the architecture is complicated that introduces more difficulty to obtain the entire vascular model.

The vascular models used for studying perfusion distribution and flow simulation can be derived from animals [97,98]. A great deal of effort has gone into developing a method to model the vessel structure of an organ from animals. Kassab et al. [99] performed histological studies on 12 plugs of 4*4 mm in both cross sectional and stereo-dissecting microscope imaging on one polymer cast. The entire coronary arteries were reconstructed and sketched, and the morphometric measurements on the segments were made on the vascular tree cast. They claimed these data are the first complete set of the whole coronary arterial trees. Mittal et al. [100] developed a computer algorithm to

extrapolate the missing branches based on the measured tree structure in order to generate a full vascular coronary tree by using Kassab's [99] morphometric data on pig coronary arterial trees from solid cast of the coronary vasculature. The proximal branches are obtained while the micro-vessels are statistically reconstructed from the histological data. Based on previous data on porcine coronary arteries from pig objects, Wischgoll et al. [101] proposed a validated software tool and applied it on microfilm corrosion casts with a focus on the main trunks of the right coronary arteries. The major focus was the validation of diameter and length measurements for the trunks of the major coronary arteries. The method was validated on a series of CT scans with a resolution of 0.6*0.6*1.0 mm3, providing a root mean square (RMS) error of 0.27 voxels. Wischgoll and Kassab et al. [102] added two additional heart samples for analyzing the entire arterial tree under CT reachable resolution. The morphometry of large (≥1mm in diameter) coronary arteries was extracted from CT images using the validated segmentation algorithm. A hepatic portal vein model [103] from Jorn et al. was built using Microfil perfused rat liver. With two resolutions at 20 µm and 5.9 µm Mayo µ-CT system volume images, the morphology on rat hepatic portal tree was analyzed. Nordsletten et al. [104] reconstructed the rat renal arterial and venous tree by integrating two-tiered resolution micro-CT image sets. The model reconstructed the complete topology of the entire vascular tree including radial, length, and connectivity data. A mouse retina model using confocal microscopy was developed by Ganesan et al. [105]. The model provides the vascular morphometric information obtained from confocal images. The retina's microvasculature sample can be made 3D for confocal microscopy.

The confocal images of retinal flat-mounts were used to quantify retinal microvasculature. Yang et al. [106] developed the 3D microvasculature model on murine lung and placenta using micro-CT images and provided some comparisons of geometry information on both organs. Beard and Bassingthwaighte [107] built the coronary arterial network in a simplified three-dimensional representation of tissue geometry that satisfies the statistical morphometric data on segment lengths, diameters and connectivity reported for the real arterial networks.

Segmentation is a basic step prior to the performance of the centerline extraction, skeletonize, and 3D modeling [108,109,110,111,112,113,114,115]. Thresholding is the easiest way to segment the vessels from the background. If a line is crossing the vessel's center, the intensity profile of the line would be a square wave. The diameter of the vessel is accurately represented by its FWHM [116]. The intensity at half maximum, a general threshold, is well-defined to distinguish the object and divide it from the background in a straightforward mannerly. However, retaining the liver tissue enables numerous vessels to remain and be captured in the images. Due to the MTF of the scanner, the blurring effect on the small-sized vessels may cause their intensities at the centers to be lower than the general threshold thus producing a large spectrum of peak intensities at the centers [117]. The larger blood vessels and the smaller vessels cannot be directly distinguished by two-level intensity thresholds because the intensity values of the non-vascular regions surrounding the large blood vessels overlap with the small blood vessel intensity values. A lower threshold also includes more false pixels near the vessel margins which would influence the accuracy on the centerline extraction. If the interfering non-vascular tissue

is not segmented out, it will have a great impact on the subsequent vascular structure extraction. We found a gradient characteristic of non-vascular regions around the large vessels and small blood vessels that can be used to make this distinction. Figure 15 (d) shows the final segmentation results including the larger vessels and the small vessels with clean boundaries. This segmented result is ready for the next centerline extraction. Blood vessels greater than threshold 1 can be quickly segmented. For vessels between threshold 1 and threshold 2, they have radius-limiting characteristics, that is, the radii of the vessels are less than approximately 5 pixels. Using the first derivatives with different Δd is an easy and efficient means by which to extract these smaller vessels. Based on this separate processing of pixels within different thresholds, blood vessels with a wide range of radius changes can be effectively extracted.

The extraction of the centerline allows the definition of two distance functions. The first one is distance-to-boundary (DTB), which is to mark each voxel as the distance to the closest vessel boundary. It embodies the characteristics of vessels on the cross-section plane. The other is distance-to-root (DTR), which initiates from the root and propagates out until the endpoints of the segmented tree structures. DRT preserves the connectivity information because the distance from root to current location is in a sequential order. Choosing a distance interval, the voxels can be divided into groups of connected voxels on the long axis of vessels in a distance range. Then the local maximum DTB inside each of the divided groups is defined as the radius of the vessel segment.

Considering the blurring function of the micro-CT, the radii of small vessels derived from DTB are inaccurate. A Gaussian correction algorithm will be employed (in

the next chapter) to correct the radii for small vessels in order to keep the accuracy of the reconstructed model. However, this was not validated by comparing corrected radii with the actual radii. This issue requires further experimentation.

In summary, we utilized separated steps to reconstruct a detailed vascular model from micro-CT images containing details based on the real vascular structure while maintaining connectivity. With the vessels approaching the pre-capillary arterioles, a three-dimensional computational domain, including the catheter injection site and its downstream extension to the tumor region, was established for further hemodynamic studies.

CHAPTER 4 ACCURACY ANALYSIS OF RECONSTRUCTED MICROVASCULATURE

1 Background

The ability of an imaging system to fulfill the responsibility of faithfully reproducing an image of the apparent object is described by the modulation transfer function (MTF). That is, the MTF of an imaging system is a measure of how well sine waves that describe the transmission of x rays through an object are represented faithfully in the image [94]. An ideal MTF should be a straight line that means no matter how the size of objects varies the imaging system would modulate and deliver a faithful dimension of the object onto the image. However, MTF for a typical imaging system is a monotonically decreasing curve that represents a function of spatial frequency. The value of the MTF is unity (i.e., 100%) at low spatial frequencies, signifying that the imaging system reproduces low frequencies without distortion or loss of resolution. As the frequency increases (object size decreases), the MTF decreases until it reaches zero, signifying that the spatial frequencies are so high that the imaging system provides no reproduction at all. Differing from low frequency, high frequency indicates the size of the object is getting smaller compared to the relative resolution, showing low fidelity of the object. The MTF of any imaging system is a product of the MTFs of the individual components of the system. The MTF of the micro-CT scanner reflects a Gaussian blurring function in general. This blurring function is convolved with the object's true cross-sectional profile, resulting in the blurred output [117]. This is indicated on image

showing that the intensity profile through the object has a significant decrease in the intensity peak as well as a wider FWHM relative to the vessel diameter as shown in Figure 23.

In the previous reconstructed vascular model, the over-estimation of radii on smaller vessels was corrected by the Gaussian correction function. To evaluate the accuracy on the correction, registration of microvasculature among tired-resolution micro-CT images were studied to quantify the comparison of the vessel segment radius between the corrected size and the measurements from high resolution images.

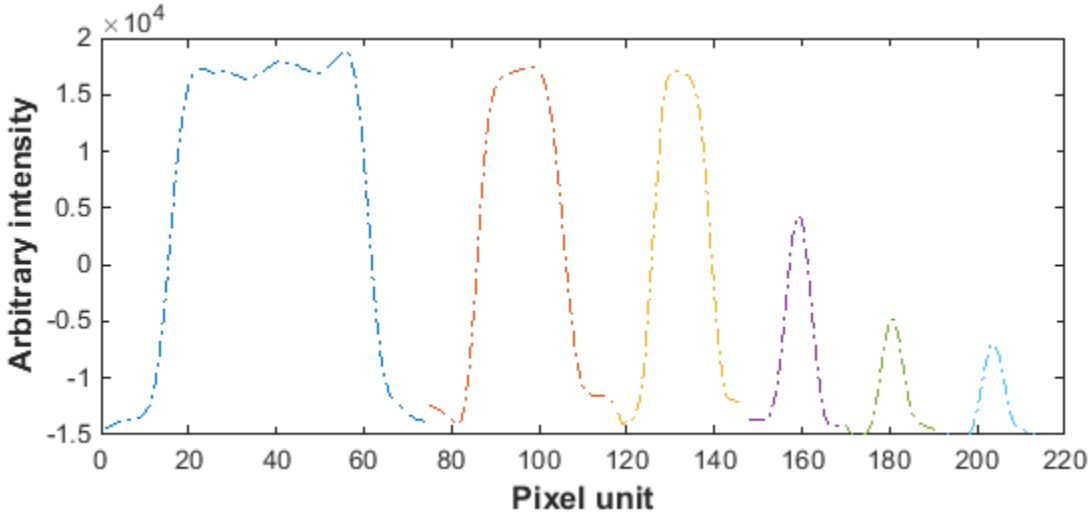

Figure 23. Plots of vessel cross-section profile plots show the decreased peak intensities as the vessel size decreases

2 Materials and Methods

Specimens were scanned intact by a Siemens Inveon micro-CT scanner on the whole livers. Multiple resolution scans were designed to produce accurate microvasculature by extending the detained vasculature from the tiered micro-CT

volumes. The whole liver sample was scanned under 195.8 µm in order to visualize the whole geometric vasculature. The left and right lobes were performed using 57.6 µm micro-CT scan. Scans with a higher resolution up to 19 µm were applied on the partial liver volume chosen from the top and bottom portions of the lobes to acquire the detailed microvasculature.

2.1 Vessel Registration among Multi-resolution Micro-CT Volumes

In order to obtain the data for accuracy comparison, 3D registration on paired-bifurcation points [118] from 57.6 µm and 19 µm resolution micro-CT volumes was applied through 3D translation, rotation and scale.

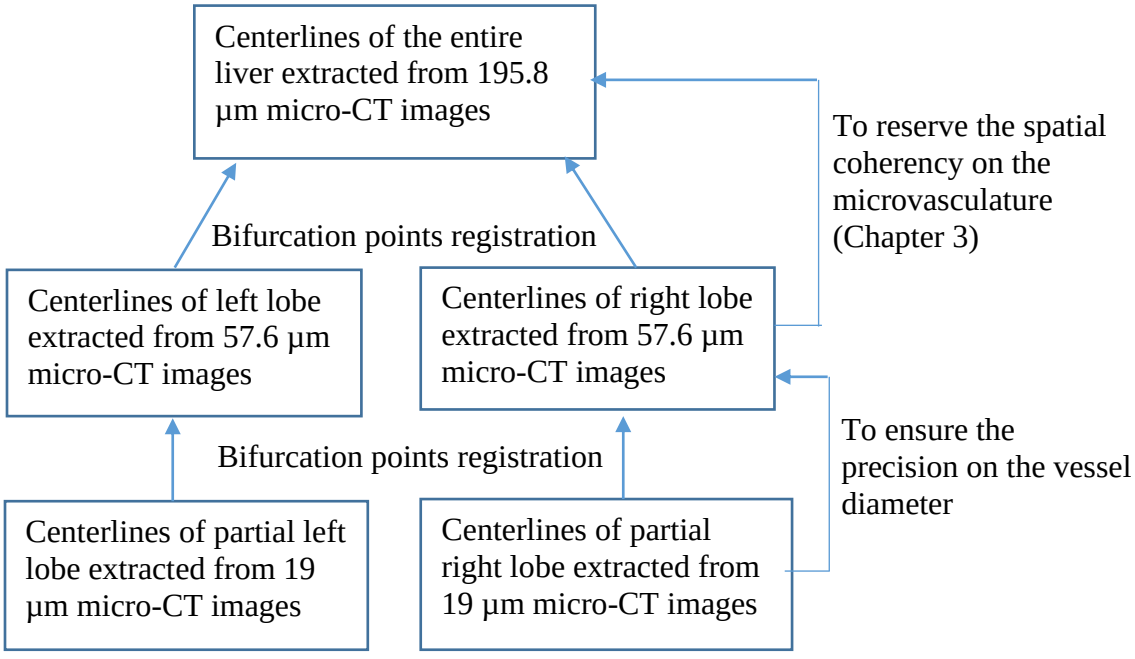

Figure 24. Schematic diagram of vessel registration among multi-resolution micro-CT volumes

2.2 Paired Center Points' Radius Measurements

After the 3D registration parameters are obtained, the two volumes were registered and paired center points with radii from both volumes are extracted for further comparison. Figure 24 illustrates the registration process.

2.3 Gaussian Blurring Correction

To correct the over-estimation on smaller objects, a Gaussian blurring correction can be employed. It utilizes the assumption that the area under the Gaussian distribution curve of the line profile is equivalent to the actual input square wave's area. A faster height-width (HW) method [119], instead of the calculus method that dividing the area into thin vertical rectangles, is used to calculate the area from the height and width of the peak where the peak is Gaussian in shape and a very good approximation for real cases where the peaks are slightly asymmetric and distorted. The correction procedure starts with using peak intensity and FWHM to estimate the area under the Gaussian curve. The estimated area under the curve is as following $A_1 = C * W_f * H_p$ where $C = 1.064\ with\ f = 0.5$. W_f, the width at 50% of peak height, is the full width at half maximum height (FWHM), and H_p is the peak height of the distribution that is the difference of the intensity between the vessel and the background. FWHM is easily acquired from the distance from the nearest non-segmented voxel though the vessel center to the other non-segmented voxel by segmenting micro-CT volume with the half intensity height on the line profile.

Then the ideal square wave profile area is calculated by using the ideal vessel's intensity peak, the square wave peak, found in large vascular lumens. The ideal area under the square wave profile is $A_2 = W_c * H_p^*$ where W_c denotes the corrected width from the vessel's true cross-sectional profile without blurring function, and H_p^* denotes the peak height of the ideal vessel's square wave profile which is represented by the average of the peak intensities derived from large diameter vascular segments.

Finally, based on the assumption that the area under the Gaussian curve is equivalent to the area of the actual square wave profile, the corrected width of the vessel lumen can be obtained through $W_c = \left(\frac{C * W_f * H_p}{H_p^*}\right)$.

2.4 Correction Validation under Multi-resolution Micro-CT Volumes

The correction can reach to sub-pixel level. To validate the accuracy of the correction, multi-resolution micro-CT scan is needed to extend the capabilities on capturing the vessel details. Since the FWHM can represent the larger vessel lumens accurately, the vessels' FWHM that are represented by higher resolution micro-CT volume can be used to compare with the same vessel corrected lumens from lower resolution micro-CT volume to provide quantitative comparison on the agreement on the correct measurement.

2.5 Quantitative Comparison on Dimension Accuracy

To quantify the vessel segment radius comparison, Bland-Altman comparison [120] was used in which it is extensively used to evaluate the agreement among two

measurements techniques with/without a gold standard. Consider a set of n center positions from vessel segments. The corresponding radii measurement under both resolution volumes are performed after the 3D registration, resulting in $2n$ data points. Each of the n radii is then represented on the graph by assigning the mean of the two measurements as the x-axis value, and the difference between the two values as the y-axis value. A given sample S with values of S_1 and S_2 determined by the two measurements is $(x, y) = \left(\frac{S_1+S_2}{2}, S_1 - S_2\right)$.

3 Results

With a higher resolution micro-CT images, more vessel segments with smaller radii were extracted as shown in the red line compared to the blue dash line in Figure 25. There is a high correlation between the probabilities of vessel segments in 195.8 µm and 57.6 µm until a certain point. Usually, a cut-off point is picked when performing the vessel segmentation to avoid the inaccuracy of vessel measurement.

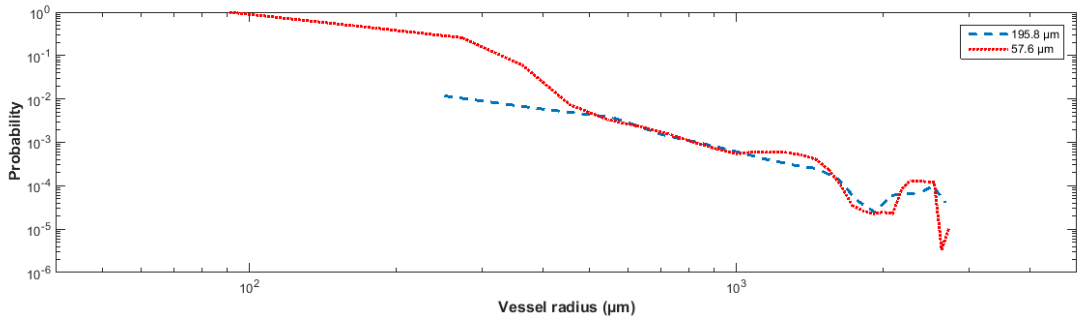

Figure 25. The probability plots of vessel radii extracted from 195.8 µm and 57.6 µm resolution micro-CT images.

To adapt to the complex vasculature, a two-step intensity-based vessel segmentation method described in the previous chapter was used to segment the vascular network in the first step. The radii of vessel segments were assigned based on the segmentation boundaries. Figure 26 shows the comparison on the radii extracted from the segmentation and the radii acquired by using the FWHM method. The results show a high correlation among the vessel segments with radii greater than 4 pixels.

To quantify the radius of individual vessel segments, the results from 35243 segments were plotted in a Bland-Altman comparison in Figure 27 which shows how well these two methods measure the vessels and does not have any assumption on any of them. For overall vessel segments, the mean radius difference between segmentation and FWHM is -0.0401 pixels with 95% confidence interval -0.3417 to +0.02615 pixels. The negative sign means the radii derived from segmentation is smaller than the radii measured from FWHM. For the vessel segments that have radii measuring greater than 4 pixels, the mean difference is -0.0276 pixels with 95% confidence interval -0.1133 to +0.1684 pixels. A high correlation is shown between segmentation and FWHM on segment radii that are greater than 4 pixels.

For the vessel segments with radii measuring less than 4 pixels, the regression plot comparison between segmentation and FWHM is shown in Figure 28. Because the radius from segmentation is the value of distance-to-boundary, the value is calculated based on the neighbors that makes the pixels discrete. The Bland-Altman comparison in Figure 29 shows the mean difference is -0.0408 pixels with 95% confidence interval -0.3432 to +0.2617 pixels. The FWHM results are over-estimated compared with the

segmented radii less than 4 pixels. It illustrates that the segmentation method extracts the pixels near the center of the small vessel.

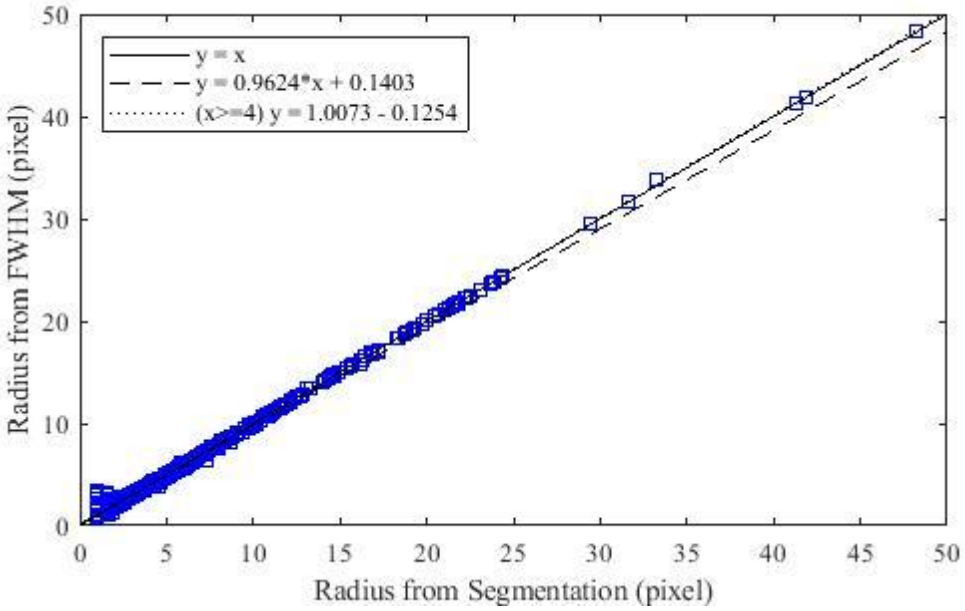

Figure 26. Radii comparison between segmentation and FWHM from 57.6 μm micro-CT images

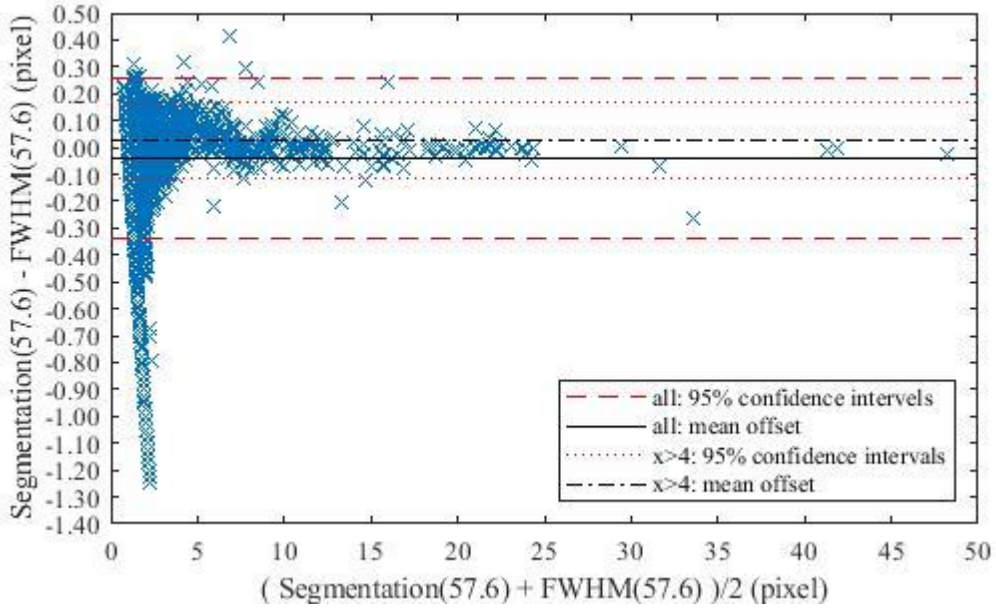

Figure 27. Bland-Altman comparison on the radii derived from segmentation and FWHM

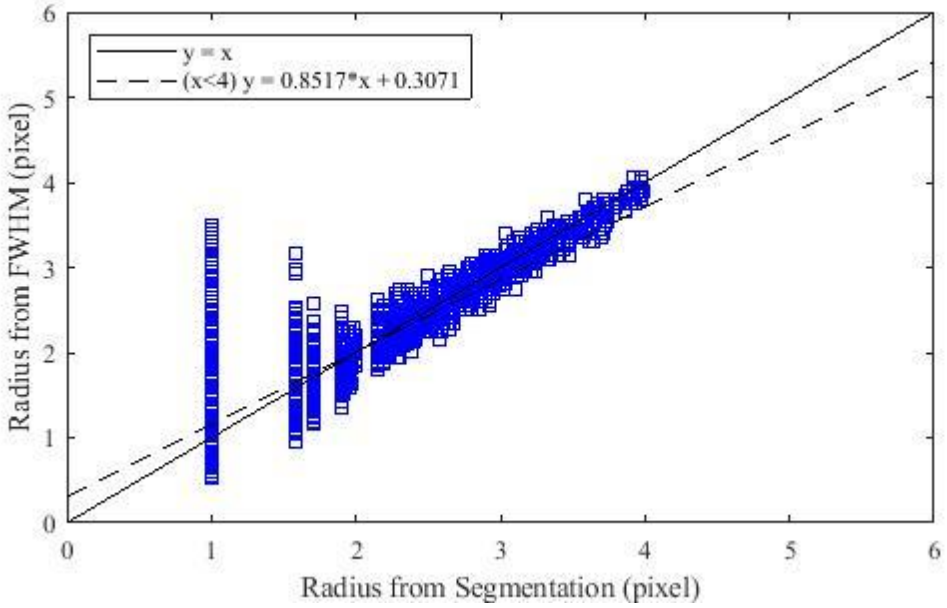

Figure 28. Radii comparison between segmentation and FWHM from 57.6 µm micro-CT images on vessel segment radii less than 4 pixels

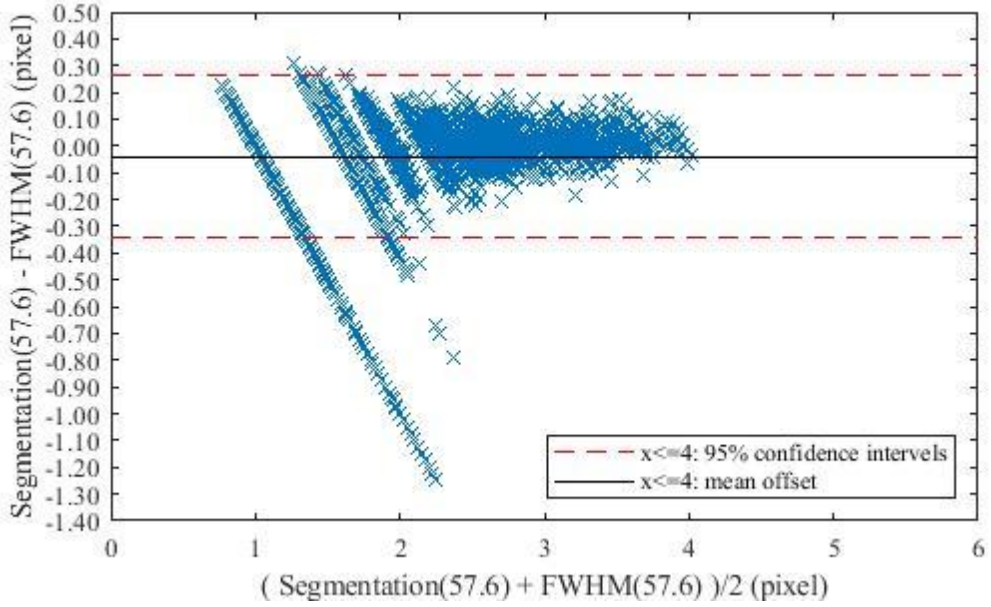

Figure 29. Bland-Altman comparison on the radii derived from segmentation and FWHM on vessel segment radii less than 4 pixels

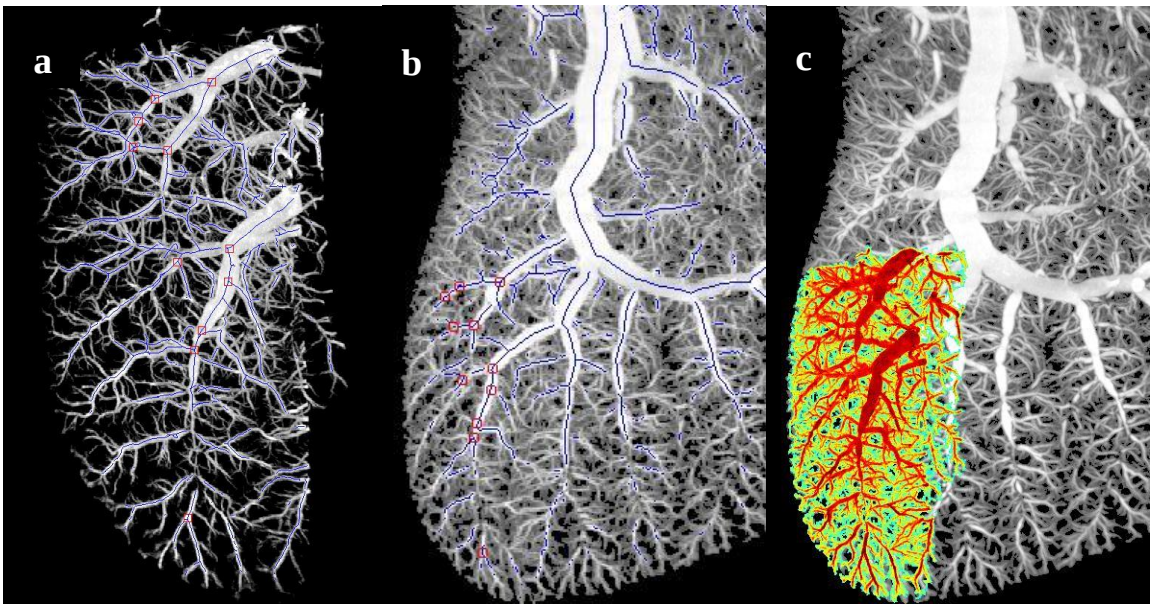

Figure 30. Registration of 19 µm micro-CT volume to 57.6 µm micro-CT volume via featured bifurcation points

Eleven featured bifurcation pairs were identified in 19 µm micro-CT volume in Figure 30(a) and 57.6 µm micro-CT volume in Figure 30(b). They were used to register the vessel skeleton extracted from 19 µm micro-CT volume to 57.6 µm micro-CT volume. Figure 30(c) displays the rigid registration result. Through one to one correspondence, the radii acquired from 19 µm micro-CT volume can be the reference to the radii obtained from 56.6 µm micro-CT volume.

In total, 1544 segments were taken into the comparison on the radii from FWHM. The registration for these segments pairs has a mean distance -1.4977 pixels and standard deviation -0.7453 pixels. The result of FWHM on 57.6 µm micro-CT volume agrees with our expectation, that small vessel diameters are over estimated as shown in Figure 31. The Bland-Altman comparison in Figure 32 exhibits the mean difference is +0.3438 pixels with 95% confidence interval -0.0658 to +0.7534 pixels.

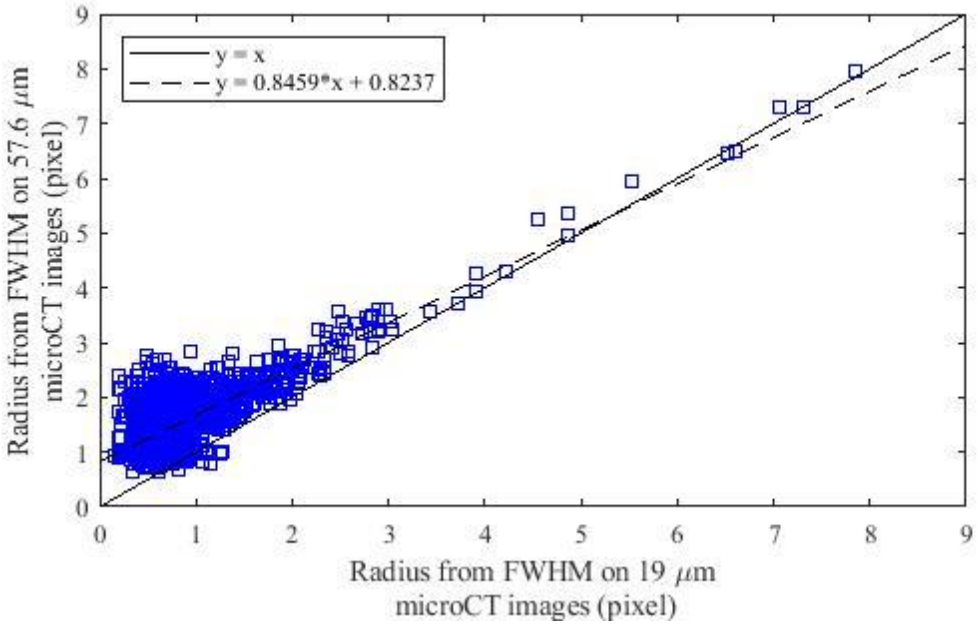

Figure 31. FWHM Radius comparison from 57.6 µm and 19 µm micro-CT images

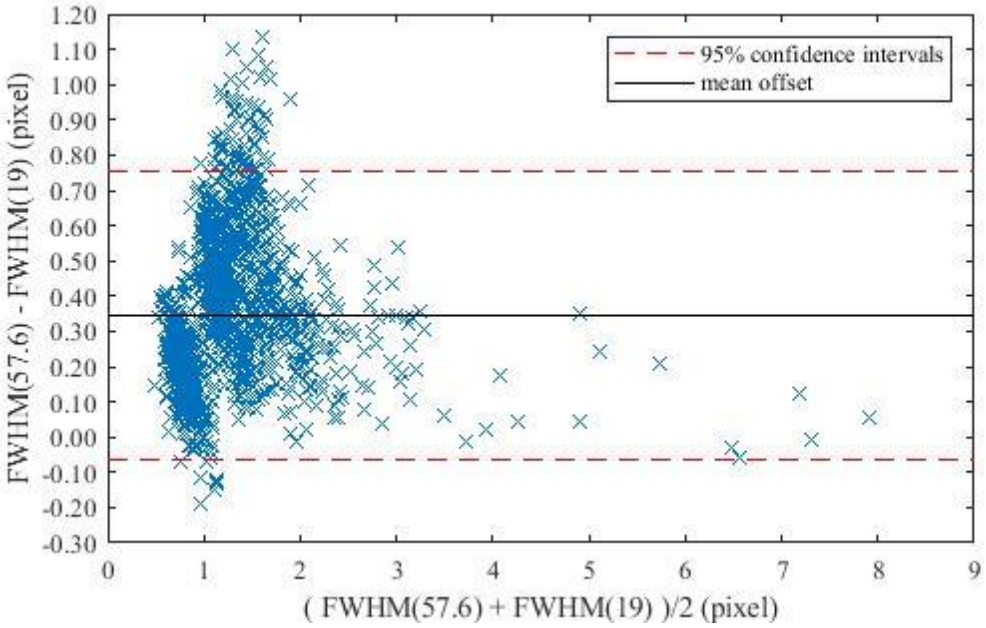

Figure 32. Bland-Altman comparison on the FWHM Radius from 57.6 µm and 19 µm micro-CT images

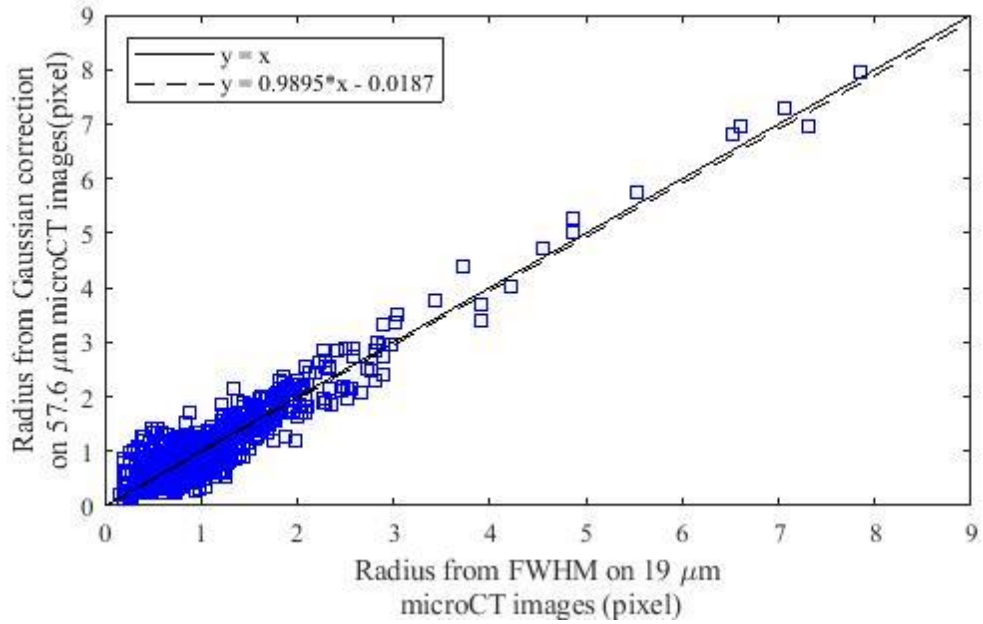

Figure 33. Regression plots for vessel segments radii from Gaussian correction 57.6 μm micro-CT images and FWHM on 19 μm micro-CT images

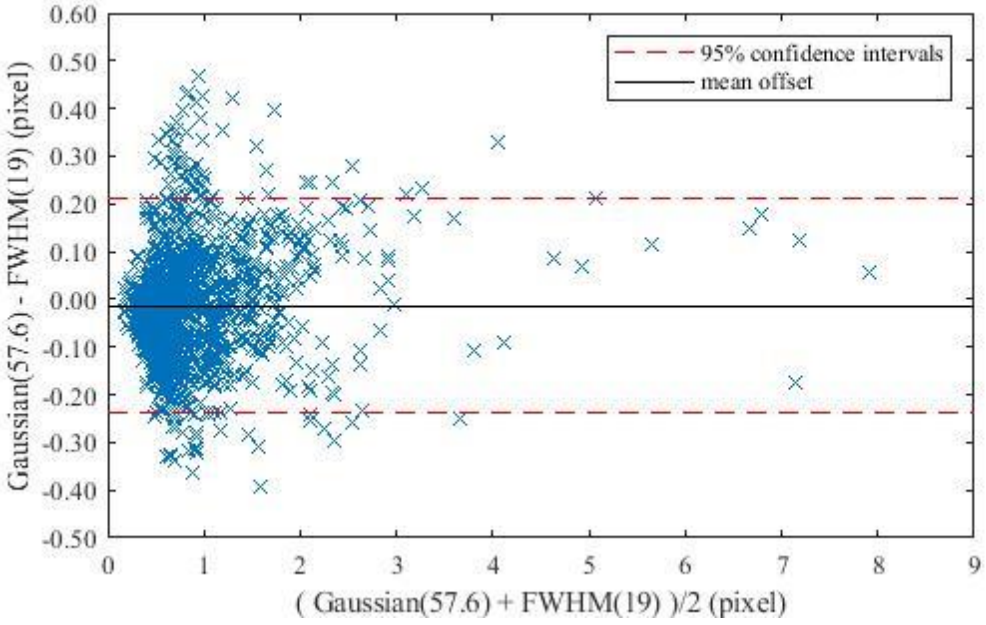

Figure 34. Bland-Altman comparison on the Gaussian corrected radii from 57.6 μm micro-CT images and the FWHM radii from 19 μm micro-CT images

By using the Gaussian correction method to correct the over-estimated segment radius, an improved regression result is obtained in Figure 33. The closer to ideal relationship shows that the Gaussian correction method is eligible to apply on the radius from FWHM that is less than 3 pixels. The Bland-Altman comparison in Figure 34 shows the mean difference is -0.0149 pixels with 95% confidence interval -0.2396 to +0.2116 pixels on the Gaussian corrected radii from 57.6 μm micro-CT images and the FWHM radii from 19 μm micro-CT images.

The intensities of the center points from 57.6 μm micro-CT volume exhibit linear regression for the Gaussian corrected radii less than 2.5 pixels in Figure 35. It can be a reference for correcting the radii of the rest lobe.

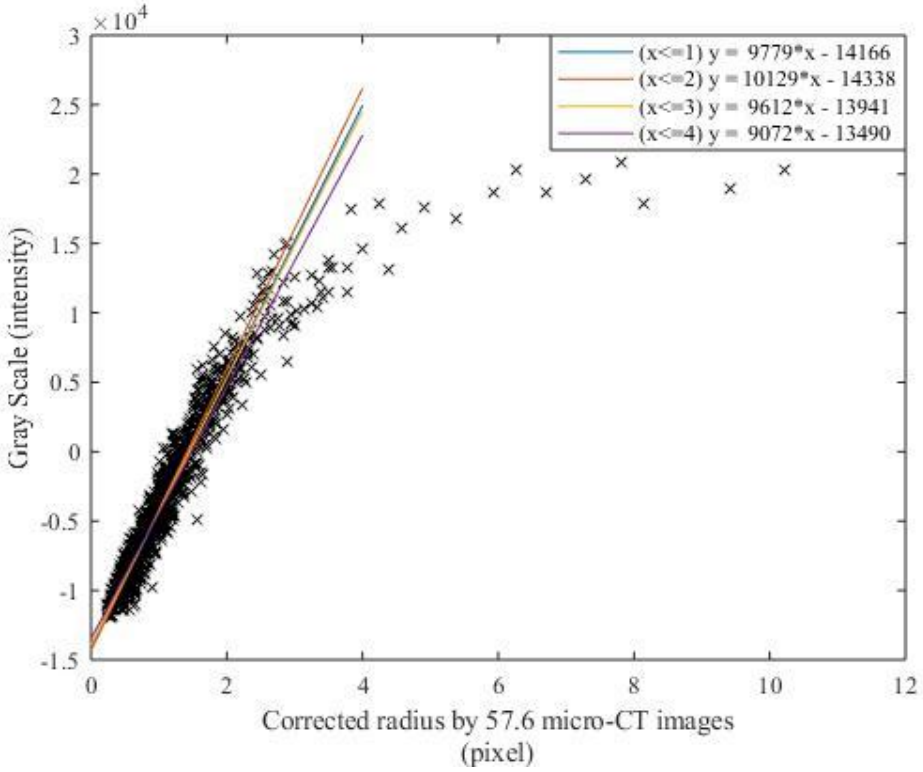

Figure 35. Intensity plots of center points with the Gaussian corrected radii from 57.6 μm micro-CT images

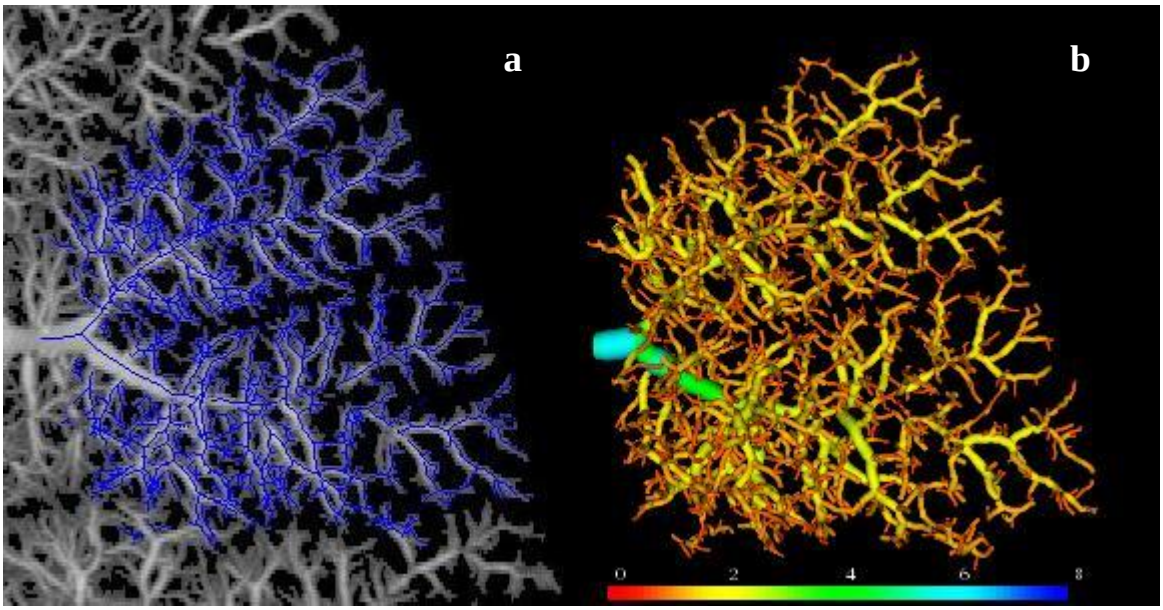

Figure 36. Illustration of a subtree with segmented radii less than 8 pixels from 57.6 μm micro-CT volume with (a) the extracted centerlines overlaid on MIP view and (b) 3D surface rendered subtree with segmented radii color mapping

A subtree from the left lobe is selected to analyze the radius correction. It is the 3D surface rendered in Figure 36 (b) with segmented radii color mapping on the vessel surface. The segment counts plot of length and radius extracted from the subtree is displayed in Figure 37. This subtree covers the vessel segments that their radii are from 1 pixel to 8 pixels and most of them are less than 3 pixels. The length of each vessel segment clusters in less than 5 pixels.

Figure 38 shows the plots of vessel segment radii measured from FWHM and Gaussian correction for the selected subtree. The count peak of radius measured by FWHM is around 2.2 pixels. The count peak of the subtree radii shifts to below 1 pixel that is sub-pixel after the Gaussian correction.

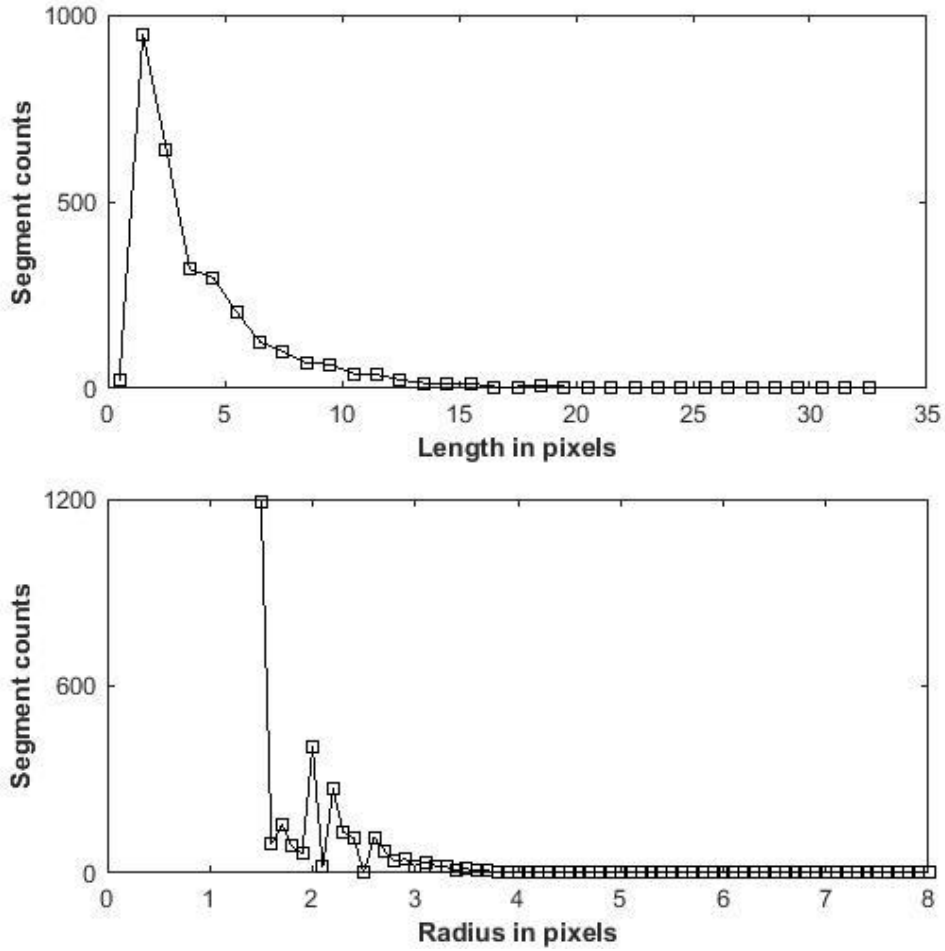

Figure 37. Plots of segment counts on the length and radius extracted from the selected subtree in Figure 36

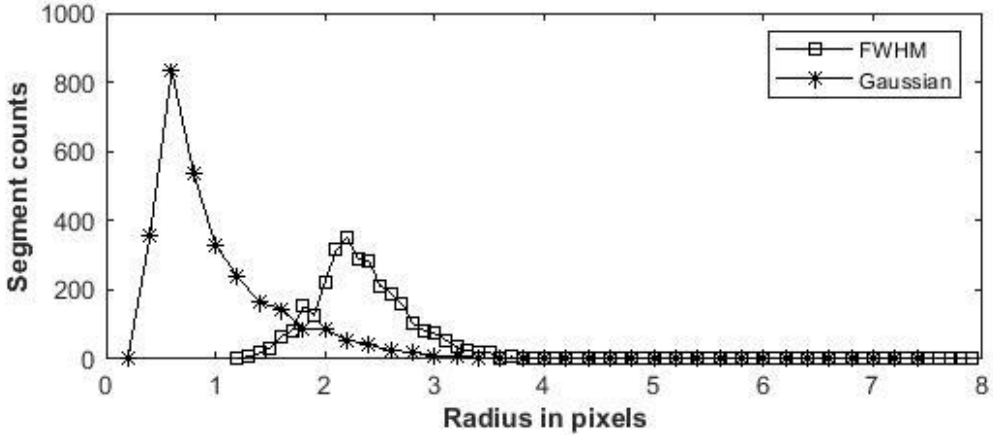

Figure 38. Plots of vessel segment radii measured from FWHM and Gaussian correction for the selected subtree in Figure 36

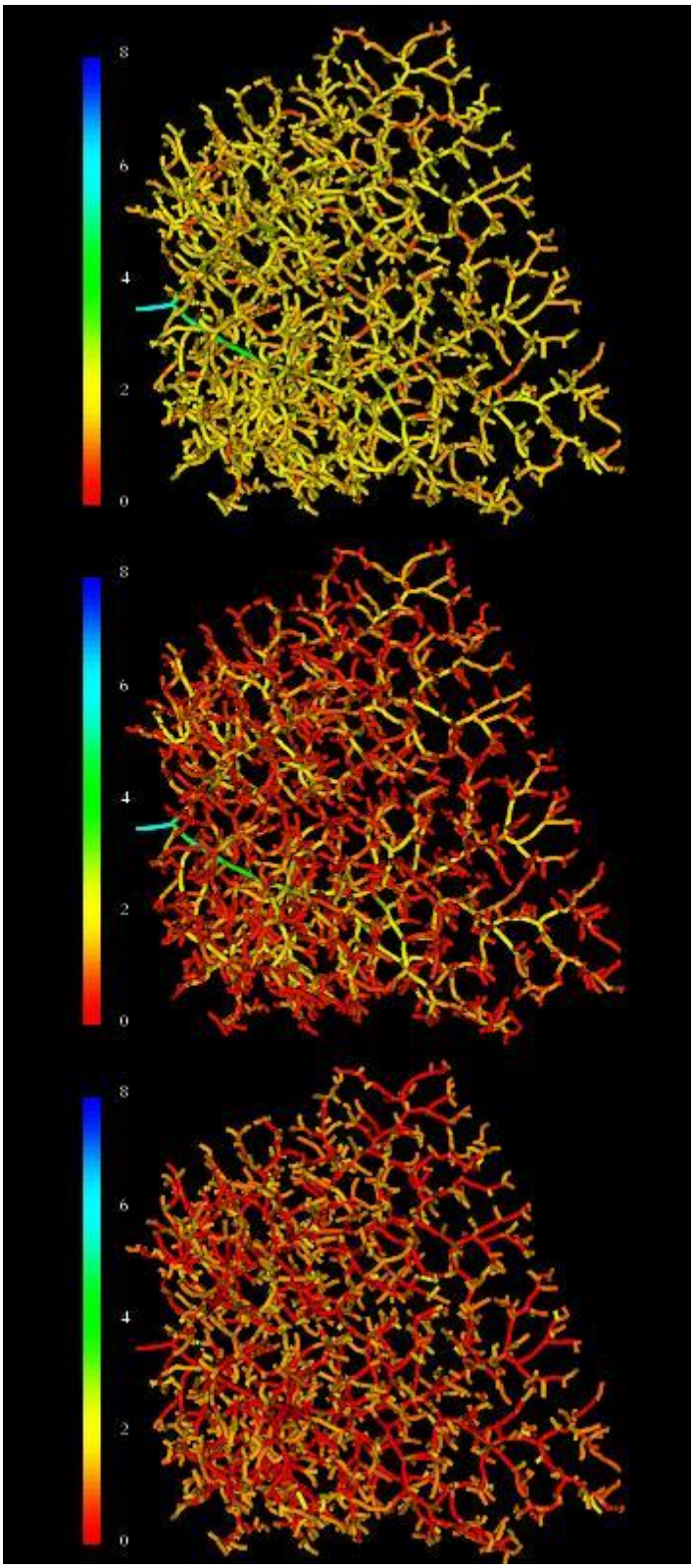

Figure 39. 3D surface rendered subtree with unit radius
(a) top panel: color mapping on the FWHM radii (b) middle panel: color mapping on the radii from Gaussian correction (c) bottom panel: color mapping on the difference between FWHM and Gaussian correction

The FWHM radii from the subtree are basically gathered near 2 pixels shown in the top panel of Figure 39. With the correction, most of the end segments are significantly changed as shown in the middle panel of Figure 39. In the bottom panel, the bigger vessel segments show few differences between FWHM and Gaussian correction while more variances are shown in the end segments.

Figure 40 (b) is the 3D reconstruction of the selected subtree after Gaussian correction on radius. Further, Figure 41 gives the 3D surface rendering on the registered left and right liver lobes with color mapping on the Gaussian corrected radii.

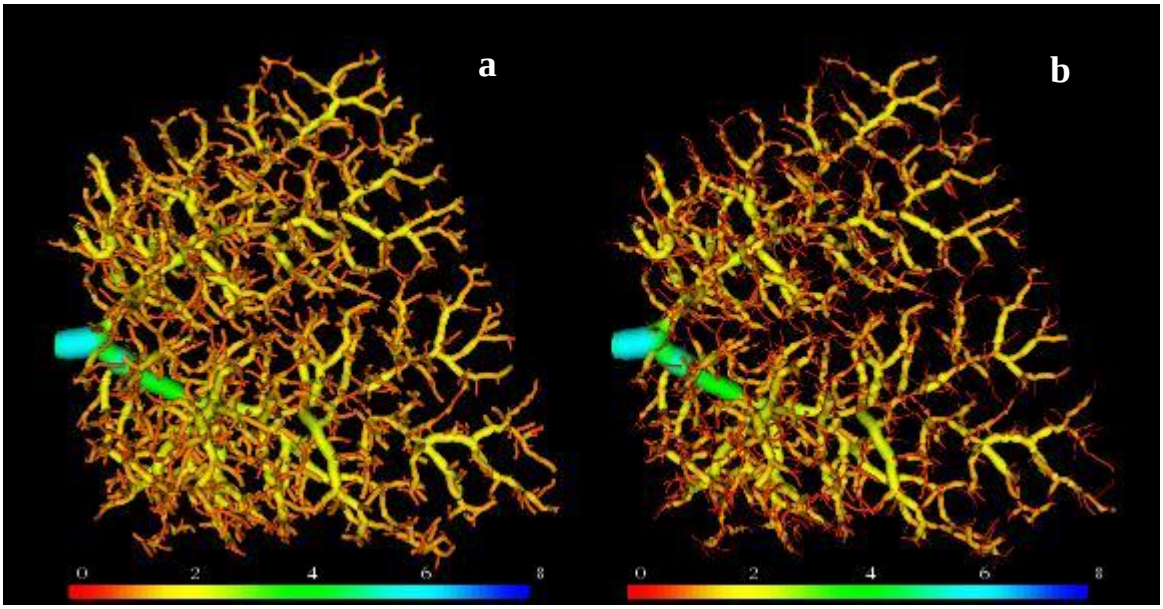

Figure 40. 3D surface rendered subtree with (a) color mapping on the segmented radii, and (b) color mapping on the Gaussian corrected radii

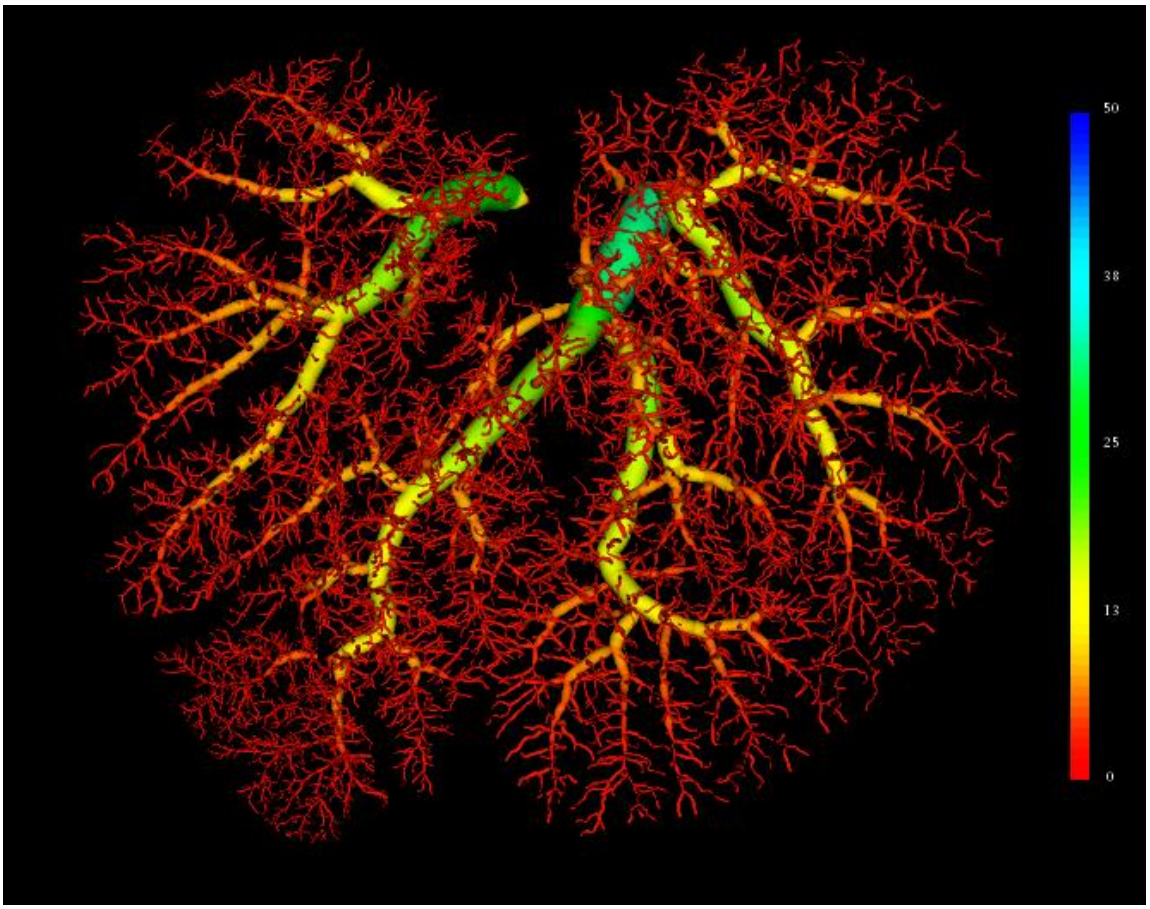

Figure 41. 3D surface rendered liver with color mapping on the Gaussian corrected radii

4 Discussion

In order to build an image-based model that has accurate vascular anatomy and covers detailed vasculature to simulate embolization, the chosen animal model, flexible imaging modality, image analysis software are key factors to ensure its success. Over a decade, the techniques in imaging capabilities advance the qualitative and quantitative studies on anatomical structures. Micro-computed tomography (micro-CT) has been recognized and applied as a high-resolution imaging modality to capture the fine structures in 3D [66,67,68,69,70,71]. Especially, resolutions down to several microns can be achieved in ex-vivo without the consideration of radiation exposure.

Due to the complexity of liver vasculature, it is essential to visualize the liver sample with high spatial resolution and over a large field of view. However, there is a trade-off between resolution and sample size which makes it difficult to acquire entire organ anatomical vasculature with desirable resolutions suitable for geometric modeling. The magnification in micro-CT can be adjusted by moving both the X-ray source and detector transaxially. As the specimen is positioned closer to the source, the anatomical structure is further magnified. Meanwhile, the field of view size is reduced. The effective space of the field of view at a high level of magnification extremely limits the sample size. It is unlikely to acquire high-resolution micro-CT images on a whole rabbit liver of moderate size that provides the detailed microvasculature. In addition, the generated file size also expands dramatically which increases the difficulty of post-processing on the micro-CT images. Table 3 summarizes the sample sizes with the resolution scanned by micro-CT and corresponding image datasets. It has a tremendous processing workload if

applying individual high-resolution micro-CT scans on dissected liver samples. Missing tissue and extra efforts to connect the segments also need to be considered.

Table 3. Summary of sample size, micro-CT resolution and data size

Sample	Sample Size	Micro-CT resolution	File Size
Whole liver	~ 15*10*8 cm^3	195.8 μm	1.0 GB
Left lobe	~ 10*8*4 cm^3	57.6 μm	3.0 GB
Right lobe	~ 10*8*4 cm^3	57.6 μm	3.24 GB
Partial left lobe – Top	~ 2*1*1 cm^3	19 μm	16.0 GB
Partial left lobe – Bottom	~ 2*1*1 cm^3	19 μm	16.8 GB
Partial right lobe – Top	~ 2*1*1 cm^3	19 μm	15.9 GB

We sought to reconstruct the microvasculature from micro-CT images acquired through high-resolution imaging over the entire liver tissue. Partial volume effect [121] is one of the image quality problems in an imaging system that produces errors on an object's dimension measurement. Though the true dimension of small vessels is not reflected in the micro-CT images, it is still noticeable in the images for the vessels when the lumen sizes are lower than the resolution compared to the background tissue. Since to scanning the entire liver under high-resolution setup is not applicable, tissue handling before imaging was developed that enabled the acquisition of high-resolution micro-CT data on reasonable dissected sub-samples and were correlated with their structures into the whole organ vasculature in multilevel resolution micro-CT images. The dimension correction on the sub-samples also can further extend the capability of micro-CT for providing the spectrum of hepatic vasculature possibly down to the size of precapillary.

Hoffmann et al. [122] studied diameter measurements of vascular segments by

comparing various techniques to determine vessel diameters. The techniques were categorized into derivative-based, threshold-based, densitometric, and model-based methods. No technique was found to accurately measure vessels with a wide size range. FWHM via the width of profile crossing vessels could reflect the larger vessel segments' diameters accurately [116]. As we studied in this chapter, the radii of vessel segments that are greater than 4 pixels obtained from segmentation have high correlation with the radii measured via FWHM. It illustrates that the larger vessel segment of the vascular model can be built via the segmentation method directly. The distance-to-boundary based on the segmentation can be used as the vessel radius for each segment. Since our modeling method is fully automated, the vascular geometry for each lobe can be directly generated on the 57.6 μm micro-CT images and with accurate radius scalar on the larger vessels.

The gold standard of the vessel dimension measurement is the optical measurements of individual vessel segments cast. However, it is not realistic for a sample with the tissue. Besides, we mentioned previously that the process for casting the Microfil® filled sample shrinks it dramatically and the vasculature does not maintain its physiological status [123]. To deal with the problems of small vessel measurements, a higher resolution micro-CT scan was applied to the partial tissue dissected from a lobe and used as a reference. The same model extraction method can be applied to a 19 um micro-CT scan on the partial sample. Through the featured bifurcation pairs manually chosen from 19 μm and 57.6 μm micro-CT images, the two micro-CT volumes can be registered. Then the segments' radii from different measurements can be compared

directly.

Consider the segment radius measured via FWHM from 19 um micro-CT images to be the standard, the same segment measured via FWHM on 57.6 um micro-CT images agrees with the assumption that over-estimation on the small segments with a radius less than 3 pixels. That meets the criteria used for other researchers to pick a cut-off radius on vessel segments for their vascular modes where 2 or 3 pixels were chosen to eliminate the potential introduced error [106,124,125]. Apply a Gaussian correction method on the vessel segments extracted from 57.6 um micro-CT images reflects a high correlation on the same segment measured from 19 um micro-CT images via FWHM showing an intuitive method to improve the model accuracy.

By comparing multi-resolution micro-CT images on the vessel segments from a partial lobe sample, we evaluated the accuracy of our reconstructed vascular model. To solve the issue of overestimation of the small blood vessels, the Gaussian correction method was proofread, and the accuracy evaluated, thereby extending the range of blood vessels to which our vascular model is applicable. In this way, we have produced a large-span vascular model while preserving the spatial relation of the liver in its physiological status. Such a blood vessel model can be applied to future simulation models.

CHAPTER 5 HEPATIC TUMOR MICROVASCULATURE

1 Background

Assa [126] in 1970 had investigated the vasculature of VX2 tumor deposits in the rabbit liver under angiography that confirms the assumption that portal supply is insufficient, and the arterial supply is the dominant supply route to the tumor. By using radioisotope and microspheres, Gray BN et al. also proved that hepatic tumors as their early stage already have an established internal vasculature perfused predominantly by the hepatic artery [127]. However, Wu H. et al. investigated the changing blood flow characteristics of VX2 tumors implanted in rabbit livers with contrast-enhanced multidetector computed tomography to establish a predictable pattern of vascular evolution over an extended 28-day growth period [128]. They found that consistent growth, appearance, and vascular changes over the 4-week observation period and the rabbit VX2 liver tumor is a hypovascular tumor with perilesional enhancement over its lifespan as imaged by MDCT. There are many studies during the past two decades on that investigate the effects of drugs, therapies, and blood supply origin based on VX2 model. Recently, Qi et al. used MR imaging and micro-CT to assess the microcirculation in a VX2 tumor model in rabbit hind leg muscle. Two parameters, relative blood volume fraction in the tumor rim and blood vessel density over the whole tumor, were studied to determine the characteristics of vascular growth in VX2 tumor [129]. VX2 rabbit liver model is used extensively for studying the treatment of HCC. The purpose of this study is to investigate hepatic VX2 tumor microvasculature via micro-CT images on the

feasibility of modeling the vascular network for a tumor vascular model that can be used for blood flow simulation in the future to aid embolization.

2 Materials and Methods

2.1 VX2 Liver Sample and Micro-CT Acquisition

VX2 tumors were implanted into the left lobe of New-Zealand White rabbits. After the VX2 tumors grew to an appropriate size of ~1 to 1.5 cm, the livers were excised after Microfil® was perfused. Whole livers were scanned intact with a Siemens Inveon micro-CT scanner at a resolution of 97.9 μm. Scans at a higher resolution down to 35.8 μm were performed on the lobe with tumors.

2.2 3D Modeling

The segmentation method mentioned previously was first applied to the micro-CT volumes. Then the distance-to-boundary function and arrival time function were calculated in order to model the VX2 nodules.

2.3 3D Volume Rendering

Volume rendering has been used for three-dimensional display of medical imaging data for over thirty years [130,131]. As a generic term referring to a three-

dimensional volume reconstruction method, it embraces all voxels in the volume to contribute in the resultant two-dimensional visualization image in which each pixel is a combination of different tissues along the view via the pixel through the volume. Given the intricate hepatic microvascular network, three-dimensional volume rendering provides a comprehensive perspective on the microstructure with spatial relation coded in the view. Ray casting, as a numerical method, is iterative computation of discretized volumetric ray integration to solve the compositing of various tissues blended inside a pixel, traces the parallel rays emitting from the viewer towards the volume and accumulates the opacity of tissue on each voxel along the corresponding ray. Besides the simplest parameters, window settings (window center and width), other parameters like color, degree of opacity or transparency, and shading are all adjustable to achieve the best visualization.

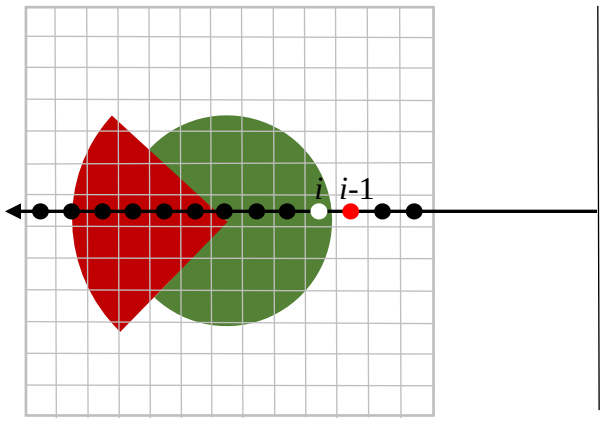

$$C_{out} = C_{in}(1 - \alpha_i) + C$$

$$C(i)_{in} = C(i-1)_{out}$$

Figure 42. Schematic diagram of 3D volume rendering. The Compositing equations where α_i denotes the opacity of the ith voxel along the ray.

3 Results

Figure 43 shows that the VX2 tumors appeared moderately hypervascular and were localized near the lobe surface. The tumor blood supply consistently appeared to be arterial. The appearance of a less dense perfusion of Microfil® within the tumor indicates necrosis without blood supply. The extracted information shows that the tumor is supplied by a hepatic artery branch and has uneven angiogenesis. The vessels do not show gradual branching. The flow can be discontinued at larger size vessels.

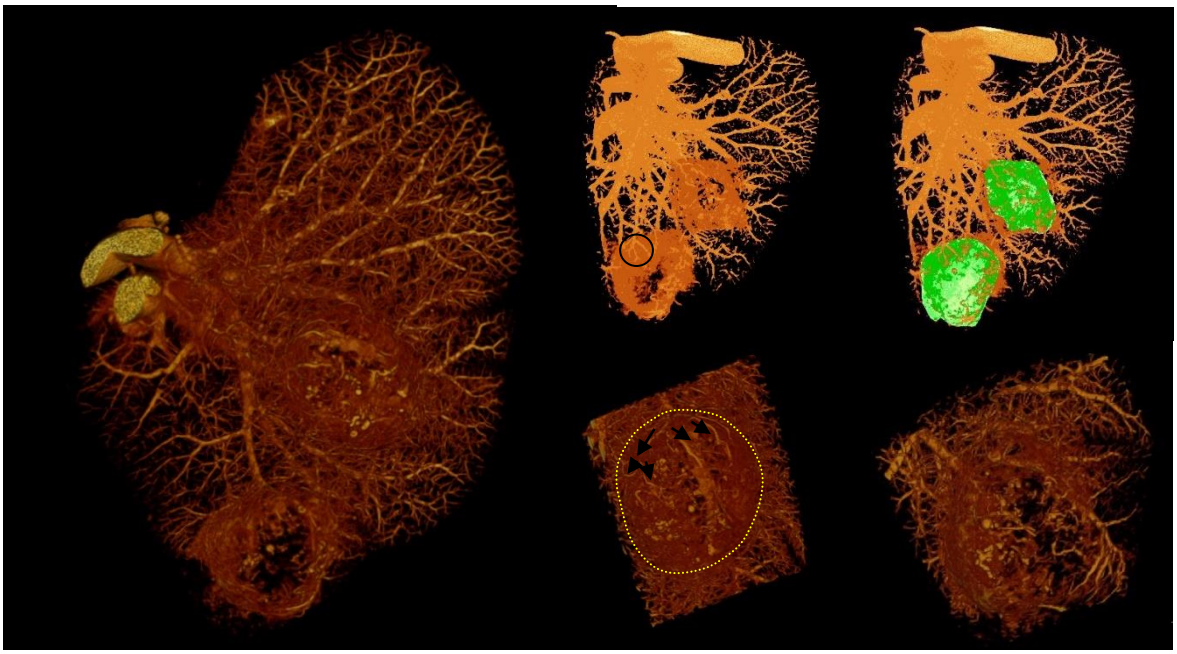

a | b | c | d | e

Figure 43. (a) 3D visualization on the VX2 implanted rabbit liver lobe. (b) 3D direct volume rendering on 97.9 µm micro-CT images; (c) with VX2 tumor surface highlight superposed on 3D micro-CT volume; (d) 3D volume rendering on the bottom VX2 using 35.8 µm micro-CT images; the black arrows pattern matches the vessel pattern in (b); (e) 3D volume rendering on the middle VX2 on 35.8 µm micro-CT images.

Table 4 shows the volume of the two VX2 masses in the above images. The feeding arterioles do not evenly surround the main mass with various vessel sizes. The sizes are reflected by the remains of Microfil® inside the vessels. The VX2 nodule located at the middle of the lobe has approximately 1.980 cm^3 mass volume measured from the micro-CT volume images and has seven feeding arteries with a diameter size range of 345.87 ± 78.12 μm. The nodule at the edge of the lobe has approximately 1.385 cm^3 mass volume and five feeding arteries with a diameter size range of 275.85 ± 26.5 μm.

Table 4. Summary of two VX2 tumor capsules on mass volume, feeding arterioles and their size

	Mass volume	Feeding arterioles	Size of feeding arterioles (d)
Middle	1.980 cm^3	7	345.87 ± 78.12 μm
Bottom	1.385 cm^3	5	275.85 ± 26.5 μm

One VX2 nodule was selected. The distance-to-boundary values were calculated based on the segmentation result and color-mapped on the 3D volume rendered VX2 microvasculature and shown in Figure 44.

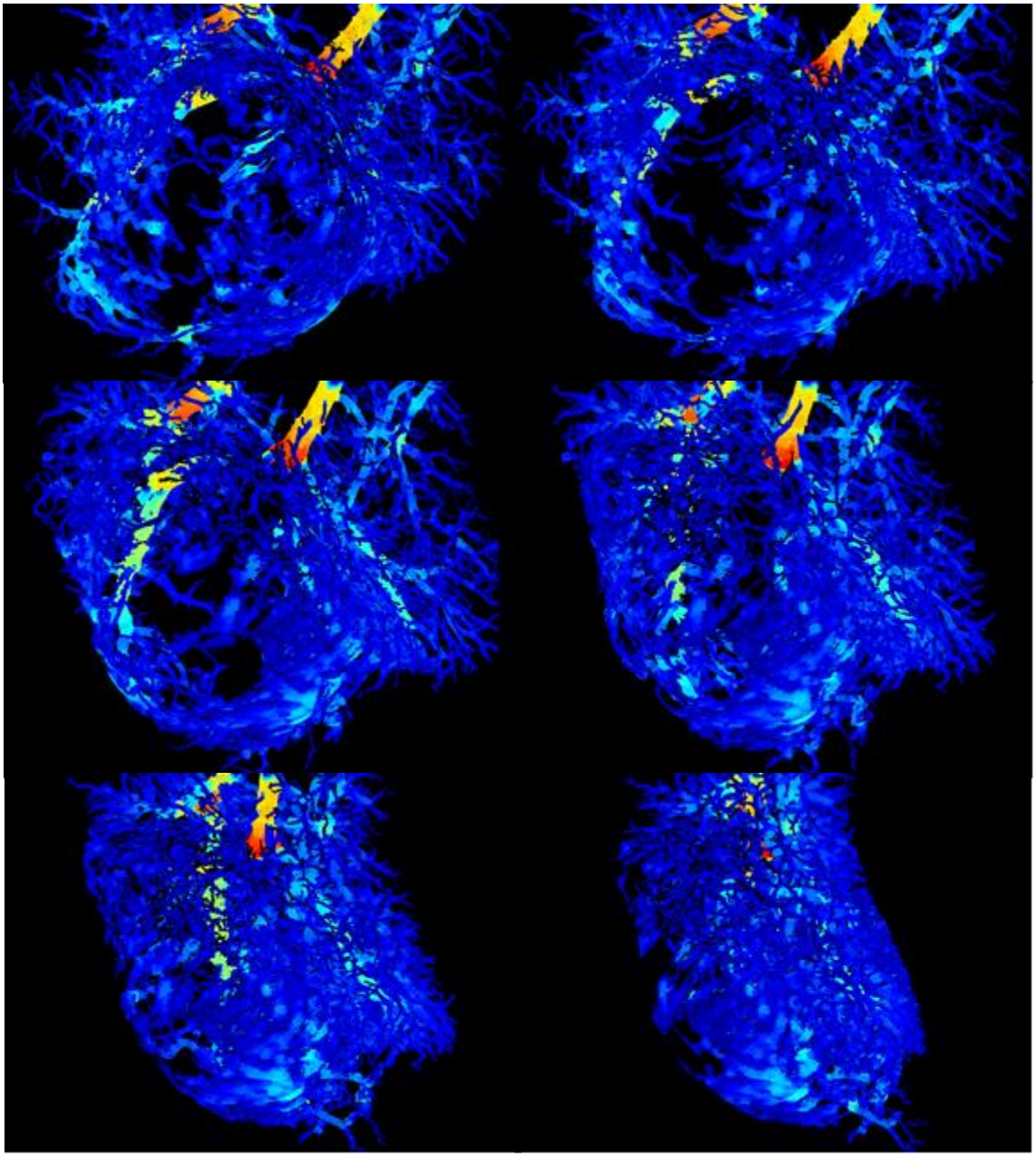

Figure 44. 3D volume rendered views on local tumor microvasculature with color mapping of measured distance-to-boundary values

4 Discussion

Rous et al. [132,133] developed the VX2 tumor model back in 1930–1940. It has been commonly used for translational research into hepatocellular carcinoma within the preclinical field of Interventional Radiology. This model uses an anaplastic squamous cell carcinoma that is easily and reliably propagated in the donor rabbit's skeletal muscle for eventual harvest and allograft implantation into the recipient's liver. This tumor graft rapidly grows into an angiographically identifiable tumor within the liver of recipient rabbits, characterized by a necrotic core that is surrounded by a viable hypervascular capsule. The inherent hypervascularity of VX2 tumors together with the moderate-sized rabbit vasculature enables technical investigation of transarterial treatments for liver tumors [134,135,136,137]. Using micro-CT to explore VX2 tumor microvasculature provides a fast and effective method to better understand tumor blood vessels that can be modeled into the computational model for flow simulation application [138,139].

From the micro-CT images, the appearance of VX2 tumor nodules is that the tumors are mainly composed of tumor blood vessels that surround the nodules. Tumor blood vessels are more abundant at the nodule interface than in central regions which has less dense perfusion of Microfil® highly indicating necrosis without blood supply. It can be explained that vascular density tends to decrease as tumors grow, leading to ischemia and ultimately necrosis as tumors outgrow their blood supply. Tumor microvasculature exhibits structurally abnormal, unevenly distributed and chaotic, and irregular branches [140,141,142,143]. The tortuosity of the VX2 surrounding vessels is observed. Tortuosity has generally been attributed to a restriction on lengthening, which is imposed by vessel

anchoring at fixed points upstream and downstream. As a result, growing tumor vessels cannot extend linearly and so they coil.

As the tumor invades larger vessels, the tumor directly intrudes into the vessel lumen making the lumen shape irregular. The vessel extraction and modeling methods used previously are not applicable to tumor vasculature. Instead of clustered local maxima of distance-to-boundary showing on the vessel cross-sections, line-like or tree-like local maxima of distance-to-boundary are found on tumor affected vessels. The tumor affected vessels cannot be modeled directly to cylinder shape vessel segments. Furthermore, via the arrival time function vessel loop is detected. Blood flow through tumors does not follow a constant, unidirectional path. Not all open vessels are perfused continuously, blood flow may follow different paths and even proceed in alternating directions through the same vessel. The tumor affected vessels cannot be simply modeled as a tree model that has no loop.

Considering the morphology of the VX2 tumor and the characteristics of blood vessel distribution, the tumor model can be considered as a spherical body distributed on the surface of the blood vessel. The blood vessels can be simulated by using normal liver blood vessels and simulating the coil. Vessels with irregular lumens can be modeled by modeling the vessel surface instead of the vessel centerlines. These could be studies in the future.

CHAPTER 6 VISUALIZATION MODEL OF EMBOLIZATION SIMULATION

1 Background

Anderson et al. [144] had investigated the relationship between regional microsphere distribution and hepatic arterial blood flow using the rat tumor model and found that blood flow reduction was considerably greater in tumors compared with normal liver after liver embolization. It implies that the embolic agents went to the tumor and blocked the blood supply. The distribution of the embolic agents during embolization can be indirectly visualized via DSA when the embolic agents block the contrast's access to the tumor. The decreased blood flow near the tumor caused by the accumulation of the embolic agents may further cause them to go into normal tissue. However, tracing the trajectory of those agents is very difficult using current imaging techniques due to the resolution capability of imaging systems and the non-radiopaque embolic agents.

To understand the factors controlling the embolic agents' distribution, the assessment of hemodynamics during embolization is important. Since dynamic flow is not visible using imaging, it can be simulated using a structural model with predefined parameters. To visualize the distribution of embolic agents, we can use flow-simulation models to study the effects of blood flow changes on them during embolization.

Current simulation models focus on investigating the factors that influence hemodynamics during embolization, such as catheter placement [77,78,79,80,81,82,83,84,85,86], microsphere characteristics (type [77,87], size and

quantity [83,85]), catheter type [88,89,90], microsphere injection techniques (injection timing [77,80], velocity [78,79,80,81,84,87,91], and interval [80,81]). The simulation and visualization of the embolic agents along with blood flow inside a vascular tree is desirable for physicians to better understand the effect of therapy and promote more effective operation planning.

Physics-based animation has been implemented widely in medical visualization for blood flow and vessel wall interactions in virtual surgery [145], and blood flow simulation [146,147]. Using the smooth particle hydrodynamics (SPH) method for flow simulation is not new but has not been extended to microsphere embolization. This chapter presents a framework to visualize the simulated embolization. The first part of the framework uses the SPH method for modeling the motion of microspheres inside a vascular model to simulate the process of embolization. The second part uses computer graphic techniques to visualize the microspheres' delivery.

2 Methods

2.1 Boundaries of Vascular Model

To build the boundary for microsphere simulation, the vessel surface of the vascular model is parameterized into mesh structures. We used the centerlines of the vessels extracted from methods described in previous chapters, via the VTK package [148] to generate vascular surface mesh structures. Surface meshes consist of vertices, edges, and faces. The purpose of the surface mesh in the final simulation is to provide

visualization of the boundaries.

2.2 Microsphere Modeling

Microspheres are modeled as spheres that are given an identical radius. The physical property of clustering among microspheres is controlled by a given limit on density within a certain spatial range. This density control also controls the incompressible property of the microspheres. If the number of microspheres within a certain space creates a higher density, then the result is repellent force causing them to be dispersed to lower the density.

2.3 Particle-based Simulation

Smoothed particle hydrodynamics (SPH) is a mesh-free, low order, discrete method to simulate fluids [149]. The SPH method [150] was adopted to explore microsphere simulation in a subset from our vascular tree network. As a meshless Lagrangian method, SPH only considers a group of neighbors given a particle point to compute the fluid quantities. It provides two solvers constant density and divergence free velocity to ensure incompressible fluid. The pseudo code of the algorithm is listed in Figure 45. The predefined velocity field distributed in the vascular domain acts as the external force which pushes the microspheres to move forward.

2.4 Visualization via web application

The web application is built with a user interface which provides the visualization window for the simulation. The framework of the simulation and visualization that we used is an open-source WebGL application [151]. WebGL is a JavaScript API that can render interactive 2D and 3D graphics. The web application is hosted on a Windows Server via Internet Information Services (IIS).

Algorithm 1 Simulation

```
function PERFORMSIMULATION
    for all particles i do                          // init neighborhoods
        find neighborhoods N_i(0)
    for all particles i do                          // init ρ_i and α_i
        compute densities ρ_i(0)
        compute factors α_i(0)
    while (t < t_max) do                            // start simulation loop
        for all particles i do
            compute non-pressure forces F_i^adv(t)
        adapt time step size Δt according to CFL condition
        for all particles i do                      // predict velocities v_i^*
            v_i^* = v_i + Δt F_i^adv / m_i
        correctDensityError(α, v^*)                 // fulfill ρ^* − ρ_0 = 0
        for all particles i do                      // update positions
            x_i(t + Δt) = x_i(t) + Δt v_i^*
        for all particles i do                      // update neighborhoods
            find neighborhoods N_i(t + Δt)
        for all particles i do                      // update ρ_i and α_i
            compute densities ρ_i(t + Δt)
            compute factors α_i(t + Δt)
        correctDivergenceError(α, v^*)              // fulfill Dρ/Dt = 0
        for all particles i do                      // update velocities
            v_i(t + Δt) = v_i^*
```

Figure 45. The pseudo code of smoothed particle hydrodynamics simulation [150]

3 Results

A subtree from the entire vascular model was extracted. The corresponding centerlines of each vessel segment together with the radius had been used to generate the surface mesh structures via VTK. The resulting mesh displayed in the upper panel of Figure 46 illustrates dense distributed meshes that includes 12960 edges. In order to decrease the computational cost, a reduced surface mesh in the lower panel of Figure 46 was generated by decreased the number of sampled points in the cross-section of each vessel segments and less sampled center points in the centerlines of each segments. The reduced density mesh includes 3510 edges.

The user-friendly interface is displayed in the upper panel of Figure 47. The surface mesh of the vascular model is displayed in the view box to define the boundaries for visualization. The microspheres are represented in cubes located inside the vascular model. The number of microspheres is generated by the volume of the cubes. In the simulation mode, the microspheres are visualized as spheres while they are moving along the vessels (shown in the following panels of Figure 47). Based on the boundaries of the vascular model and the velocity field, the microspheres are finally directed to different branches.

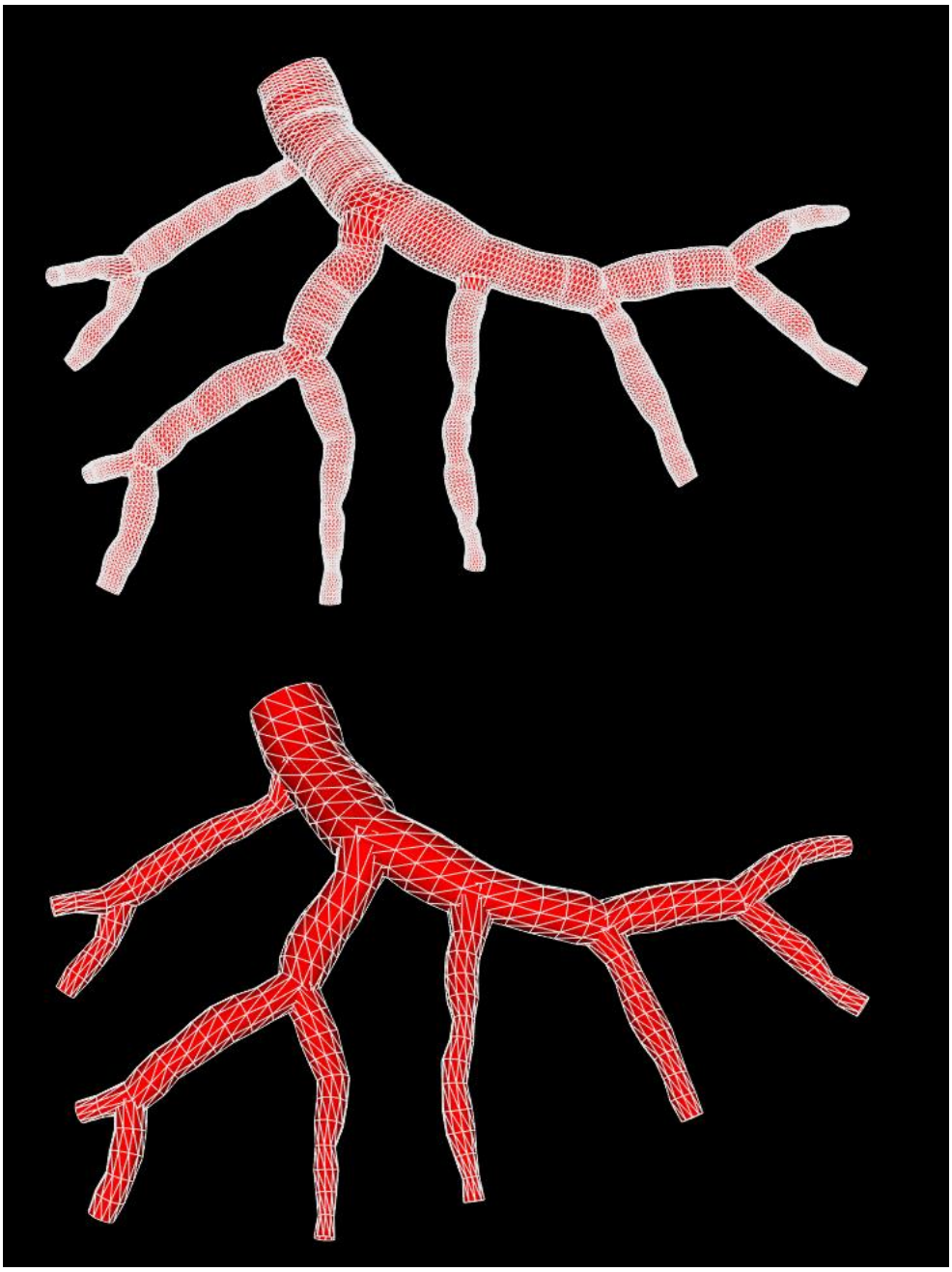

Figure 46. Surface mesh on a reconstructed vascular model. The upper panel displays the surface mesh generated with 20 sampled points on the cross-section of each vessel segment; the lower panel displays the surface mesh generated by 10 sampled points on the cross-section of each vessel segment and has fewer sampled points on the centerlines.

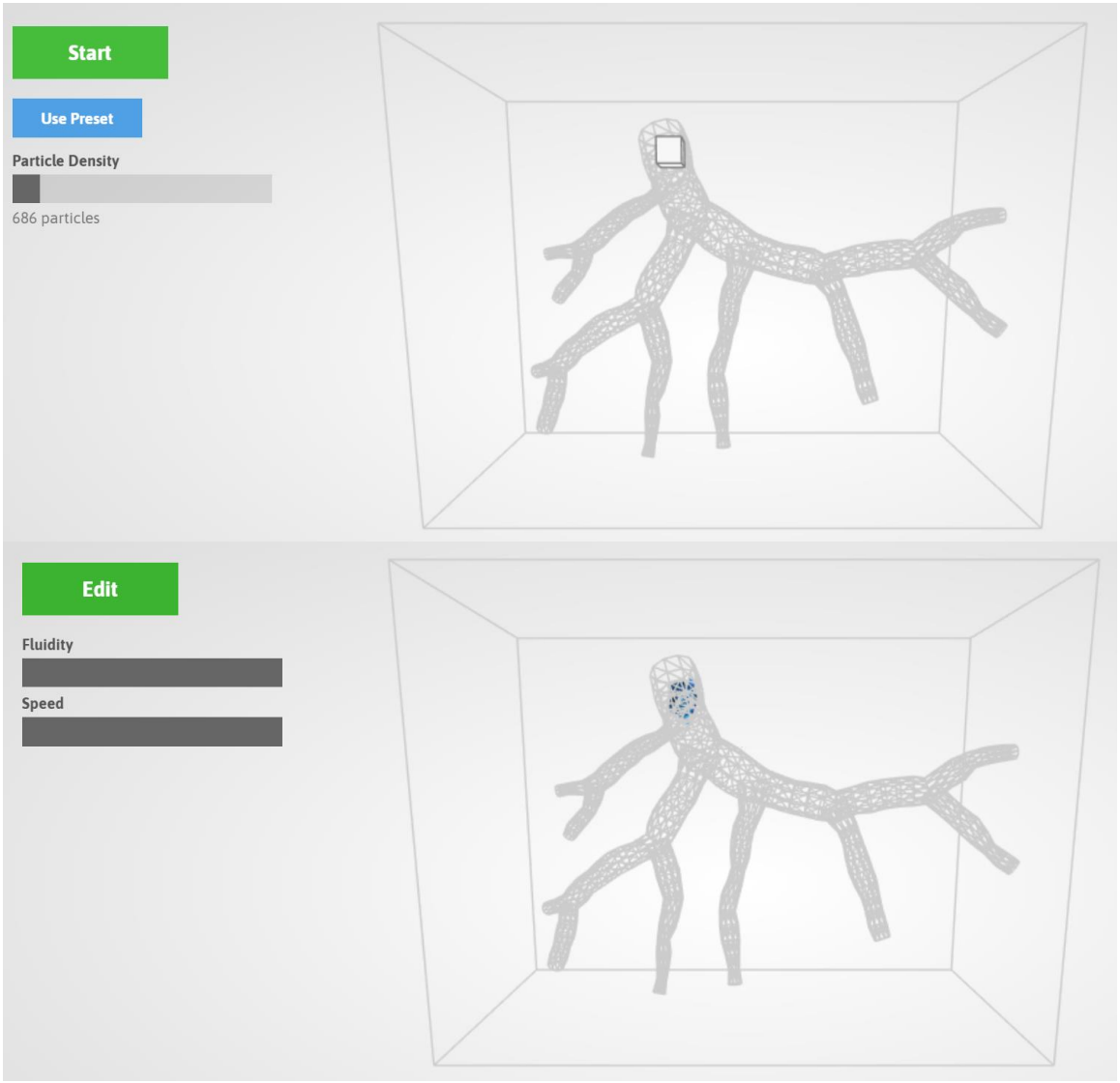

Figure 47. The demonstration of microsphere simulation via the web application interface. The initial status is shown in the upper panel. The simulation and visualization modes are shown in the following panels.

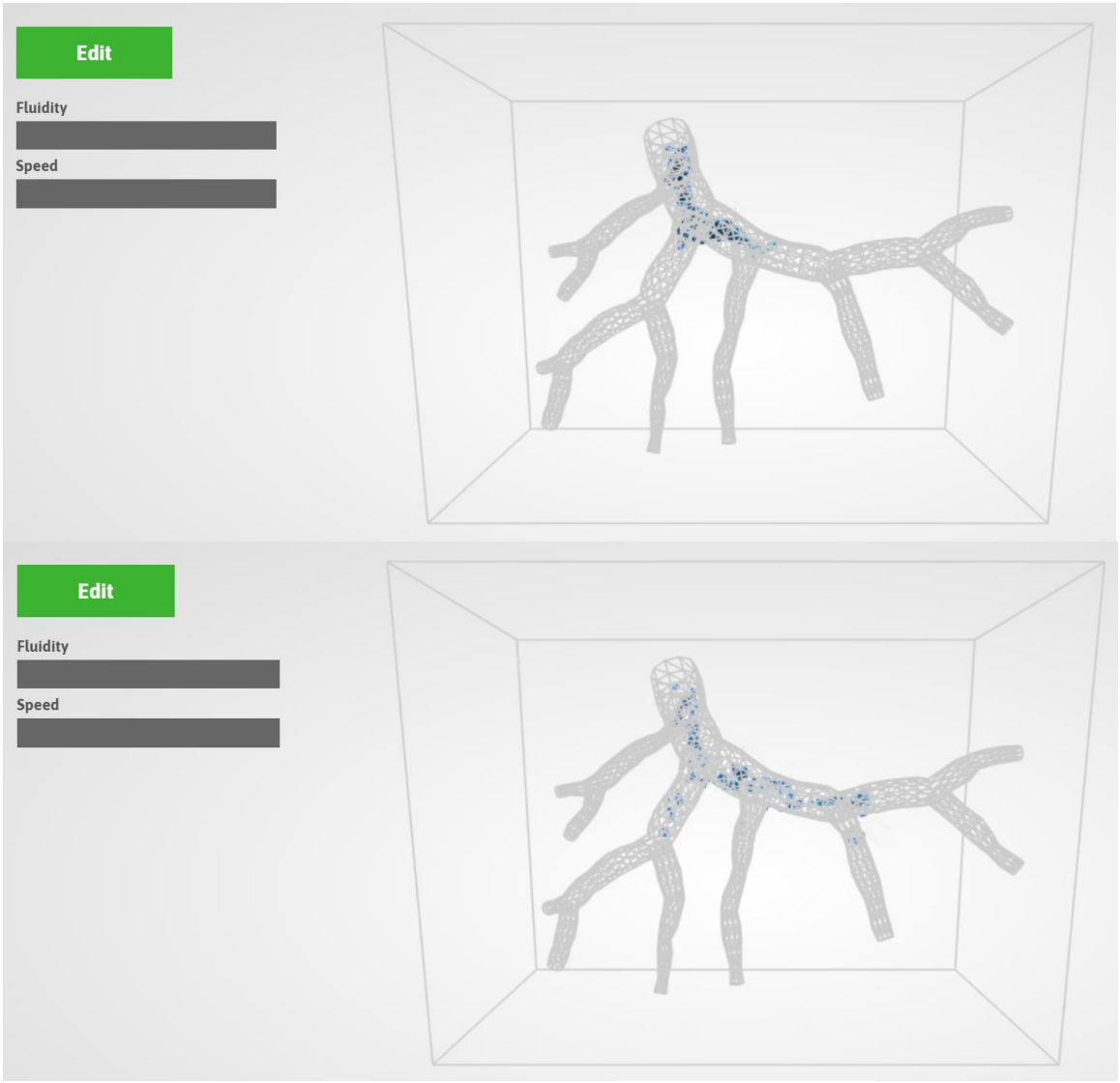

Figure 47 (con't). The demonstration of microsphere simulation via the web application interface. The initial status is shown in the upper panel. The simulation and visualization modes are shown in the following panels.

4 Discussion

Compared to computational fluid dynamics (CFD) that cannot be directly applied to computer graphics, Smoothed Particle Hydrodynamics (SPH) handles the simulation on complex fluid effects and is applicable in computer graphics [149,152]. The Navier-Stokes equations that SPH uses to solving the fluid motion are discretized using moving particles and their interactions. The advantage of the particle method is that it is stable, requires fewer iterations, can use larger time steps, and is easier to implement. With respect to the user-interaction interface, it is easy and intuitive to control the simulation. The introduction of a particle-based method in computer graphics to deal with the motion of microspheres in the vascular model is an ongoing challenge to simulate the embolization process.

A surface mesh was generated for visualization purposes only since the simulation of SPH is a mesh-free method. Though the surface mesh was not used for the simulation, it still needed to be loaded into the browser buffer and be rendered during the simulation of each frame. Even with a reduced density surface mesh, it still takes a few seconds to load the mesh each time the browser is refreshed to run a new simulation. Generating the surface mesh representing the vascular domain is sufficient to give the viewer an intuitive feel for the vascular domain.

When the microspheres are released, the initial velocities are obtained by their location in the velocity field. To calculate the velocities of the microspheres at the next time point, all the neighbors need to be considered and weighted for each microsphere. According to the location of microspheres, the velocity of the microspheres needs to be

adjusted if they hit the boundaries of the model to keep them inside the vascular domain. The velocities from each location are added as the external force on the microspheres. The neighbors of each microsphere are needed to compute the divergence for the pressure projection. The weighted velocity is used to calculate the temporal divergence which is the sum of the weighted velocities. The density of the unit area is evaluated. If the surrounding neighbors affect the current microsphere, the divergence is adjusted according to the weights of neighbors. This is to keep a unit cell from being too crowded. Via a Jacobi iteration, the new pressure is obtained which considers the interaction of the neighbors. The final pressure combines the environment velocity and the divergence. All the microspheres are pushed to the new locations via this final pressure. Finally, the new locations are evaluated to ensure every microsphere is within the vascular domain and ready to simulate for the next time frame.

The advantage of using WebGL is that it is not only capable of implementing computer graphics tasks but also that it is easy to apply within any compatible web browser without the use of plug-ins. WebGL allows the GPU to accelerate the use of physics and image processing and to render effects on the web page. The model can be easily expanded and generalized compared to traditional software.

The simulation model we use is based on an open-source WebGL application by David Li [151] to simulate fluid flowing inside a cube. Importing the vascular model into the simulation coordinate and mapping the parameters into textures to process in the vertex and fragment shader in the graphics processing unit (GPU) is extremely difficult. The complexity of the simulation model depends on the model's resolution. The vascular

model needs to be transferred from world coordinates into graphics coordinates. The resolution of the vascular model may be decreased to lower the computational cost. The overall mechanical properties on microspheres were calculated by the SPH method.

Only one fluid, microspheres, was simulated in this model. The local velocity at each location was kept constant during the simulation. The local velocity change caused by the accumulation of the microsphere was not considered in the simulation model and only a simplified velocity field was applied in this study.

In summary, a computer simulation model for simulating and visualizing the motion of the microsphere during embolization was designed and built successfully. This model can be used to investigate the microspheres' interaction within the vessel using realistic conditions. The obtained numerical results from this model can be directly visualized and give radiologists an intuitive means to understand the behaviors of microspheres during embolotherapy. Further, the vascular model used in the SPH method can be replaced by a patient-specific vascular model to predict the effect of embolotherapy.

CHAPTER 7 CONCLUSION

The present study is part of a long-term project targeting the development of a hemodynamic model capable of simulating embolization inside the hepatic microvasculature. A realistic three-dimensional description of the vascular network is the basis of the model. The microvascular model can be obtained by three-dimensional reconstruction from micro-CT images. An adaptive segmentation method is needed to extract vessels over a large range of different vessel radii. Through registration, detailed microvasculature can be acquired from separately reconstructed structures on higher resolution images. A vascular network model based on real vascular structure with details and continuity was established for further embolization studies.

The chosen cut-off radius on the vascular model should be considered if the model is directly used on vessels without dimensional corrections. By comparing multi-resolution micro-CT images on the vessel segments from a partial lobe sample, we evaluated the accuracy of our reconstructed vascular model. To overcome the limitations of the imaging system on capturing accurate microvasculature, the vessel correction method provides a good approach to dealing with this challenge. The Gaussian correction method is applicable to the problem of overestimation of the small blood vessels thereby extending the range of blood vessels to the final vascular model. In this way, we have produced a large-span vascular model while preserving the spatial relation of the liver in its physiological form.

The morphology of microvasculature for VX2 tumors has tremendous variation compared to normal hepatic vasculature. The microvasculature cannot be reconstructed

directly due to the irregular vessel cross-sectional shape and loss of vessel structure. The tumor model may be considered as a spherical body distributed on the surface of the blood vessels derived from the normal state.

A web-based application based upon modeled hepatic microvasculature was built to visualize the transmission of emboli. This application can be used not only to directly visualize the embolization process but also to analyze hemodynamics in different situations, providing a reference for actual clinical operations. The work presented here is intended to provide a basis for building visual simulation models for the unique vascular structures of individual human patient at some point in the future.

REFERENCES

1. Bray, F., J. Ferlay, I. Soerjomataram, R. L. Siegel, L. A. Torre, and A. Jemal. Global cancer statistics 2018: GLOBOCAN estimates of incidence and mortality worldwide for 36 cancers in 185 countries. *CA: A Cancer Journal for Clinicians* 68(6):394–424, 2018.

2. Llovet, J. M., J. Fuster, and J. Bruix. The Barcelona approach: Diagnosis, staging, and treatment of hepatocellular carcinoma. *Liver Transplantation* 10(2 suppl 1):S115-20, 2004.

3. Bruix, J., M. Reig, and M. Sherman. Evidence-Based Diagnosis, Staging, and Treatment of Patients With Hepatocellular Carcinoma.*Gastroenterology* 150(4):835–853, 2016.

4. Lautt, W. W. Hepatic Circulation. Colloquium Series on Integrated Systems Physiology: From Molecule to Function 1:1–174, 2009.

5. Choi, J.-Y., J.-M. Lee, and C. B. Sirlin. CT and MR Imaging Diagnosis and Staging of Hepatocellular Carcinoma: Part I. Development, Growth, and Spread: Key Pathologic and Imaging Aspects. *Radiology* 272(3):635–654, 2014.

6. Marelli, L., R. Stigliano, C. Triantos, M. Senzolo, E. Cholongitas, N. Davies, J. Tibballs, T. Meyer, D. W. Patch, and A. K. Burroughs. Transarterial Therapy for Hepatocellular Carcinoma: Which Technique Is More Effective? A Systematic Review of Cohort and Randomized Studies. *CardioVascular and Interventional Radiology* 30(1):6–25, 2006.

7. Young, S., P. Craig, and J. Golzarian. Current trends in the treatment of hepatocellular carcinoma with transarterial embolization: a cross-sectional survey of techniques. *European Radiology* 29(2):3287–3295, 2018.

8. Gaba, R. C. Chemoembolization Practice Patterns and Technical Methods Among Interventional Radiologists: Results of an Online Survey. *American Journal of Roentgenology* 198(3):692–699, 2012.

9. Sieghart, W., F. Hucke, and M. Peck-Radosavljevic. Transarterial chemoembolization: Modalities, indication, and patient selection. *Journal of Hepatology* 62(5):1187–1195, 2015.

10. Gaba, R. C., R. P. Lokken, R. M. Hickey, A. J. Lipnik, R. J. Lewandowski, R. Salem, D. B. Brown, T. G. Walker, J. E. Silberzweig, M. O. Baerlocher, A. M. Echenique, M. Midia, J. W. Mitchell, S. A. Padia, S. Ganguli, T. J. Ward, J. L. Weinstein, B. Nikolic, and S. R. Dariushnia. Quality Improvement Guidelines for

Transarterial Chemoembolization and Embolization of Hepatic Malignancy. *Journal of Vascular and Interventional Radiology* 28(9):1210–1223, 2017.

11. Piscaglia, F., and S. Ogasawara. Patient Selection for Transarterial Chemoembolization in Hepatocellular Carcinoma: Importance of Benefit/Risk Assessment. *Liver Cancer* 7(1):104–119, 2018.

12. Lee, K.-H., K.-B. Sung, D.-Y. Lee, S. J. Park, K. W. Kim, and J.-S. Yu. Transcatheter Arterial Chemoembolization for Hepatocellular Carcinoma: Anatomic and Hemodynamic Considerations in the Hepatic Artery and Portal Vein. *RadioGraphics* 22(5):1077–1091, 2002.

13. Rose, S. C., S. G. Kikolski, and J. E. Chomas. Downstream Hepatic Arterial Blood Pressure Changes Caused by Deployment of the Surefire AntiReflux Expandable Tip. *CardioVascular and Interventional Radiology* 36(5):1262–1269, 2012.

14. Bilbao, J. I., P. Garrastachu, M. J. Herráiz, M. Rodríguez, M. Iñarrairaegui, J. Rodríguez, C. Hernández, A. M. D. L. Cuesta, J. Arbizu, and B. Sangro. Safety and Efficacy Assessment of Flow Redistribution by Occlusion of Intrahepatic Vessels Prior to Radioembolization in the Treatment of Liver Tumors. *CardioVascular and Interventional Radiology* 33(3):523–531, 2009.

15. M. Tal, E. Miller, N. Holtzman, Y. Zipory, T. Dagan, O. Harbater. Reduced Non-Target Embolization and Increased Targeted Delivery of Embolization Particles in an Anatomical Arterial Flow Model Using a Novel Microcatheter, *Society of Interventional Oncology*, Boston, poster 81 2018

16. M. Tal, E. Miller, N. Holtzman, Y. Zipory, T. Dagan, O. Harbater. Usability, Safety and Efficacy of a Novel Microcatheter for Reducing Non-Target Embolization, *Society of Interventional Oncology*, Boston, poster 85, 2018

17. Rose, S. C., K. H. Narsinh, A. J. Isaacson, A. M. Fischman, and J. Golzarian. The Beauty and Bane of Pressure-Directed Embolotherapy: Hemodynamic Principles and Preliminary Clinical Evidence. *American Journal of Roentgenology* 212(3):686–695, 2019.

18. Xu, Z., S. Jernigan, C. Kleinstreuer, and G. D. Buckner. Solid Tumor Embolotherapy in Hepatic Arteries with an Anti-reflux Catheter System. *Annals of Biomedical Engineering* 44(4):1036–1046, 2015.

19. Rose, S. C., G. D. Halstead, and K. H. Narsinh. Pressure-Directed Embolization of Hepatic Arteries in a Porcine Model Using a Temporary Occlusion Balloon Microcatheter: Proof of Concept. *CardioVascular and Interventional Radiology* 40(11):1769–1776, 2017.

20. Matsumoto, T., J. Endo, K. Hashida, H. Mizukami, J. Nagata, H. Ichikawa, S. Kojima, S. Takashimizu, T. Yamagami, N. Watanabe, and T. Hasebe. Balloon-occluded arterial stump pressure before balloon-occluded transarterial chemoembolization. *Minimally Invasive Therapy & Allied Technologies* 25(1):22–28, 2015.

21. Kakuta, A., K. Shibutani, S. Ono, H. Miura, F. Tsushima, S. Kakehata, K. Basaki, H. Fujita, H. Seino, T. Fujita, and Y. Takai. Temporal variations in stump pressure and assessment of images obtained from cone-beam computed tomography during balloon-occluded transarterial chemoembolization. *Hepatology Research* 46(5):468–476, 2015.

22. Irie, T., M. Kuramochi, and N. Takahashi. Dense Accumulation of Lipiodol Emulsion in Hepatocellular Carcinoma Nodule during Selective Balloon-occluded Transarterial Chemoembolization: Measurement of Balloon-occluded Arterial Stump Pressure. *CardioVascular and Interventional Radiology* 36(3):706–713, 2013.

23. Ishikawa, T., S. Abe, R. Inoue, T. Sugano, Y. Watanabe, A. Iwanaga, K. Seki, T. Honma, T. Nemoto, K. Takeda, and T. Yoshida. Predictive Factor of Local Recurrence after Balloon-Occluded TACE with Miriplatin (MPT) in Hepatocellular Carcinoma. *PLoS ONE* 9(7): e103009, 2014.

24. Pasciak, A. S., J. H. Mcelmurray, A. C. Bourgeois, R. E. Heidel, and Y. C. Bradley. The Impact of an Antireflux Catheter on Target Volume Particulate Distribution in Liver-Directed Embolotherapy: A Pilot Study. *Journal of Vascular and Interventional Radiology* 26(5):660–669, 2015.

25. Asayama, Y., A. Nishie, K. Ishigami, Y. Ushijima, Y. Takayama, D. Okamoto, N. Fujita, K. Morita, and H. Honda. Hemodynamic changes under balloon occlusion of hepatic artery: predictor of the short-term therapeutic effect of balloon-occluded transcatheter arterial chemolipiodolization using miriplatin for hepatocellular carcinoma. *SpringerPlus* 5:157, 2016.

26. Hatanaka, T., H. Arai, and S. Kakizaki. Balloon-occluded transcatheter arterial chemoembolization for hepatocellular carcinoma. *World Journal of Hepatology* 10(7):485–495, 2018.

27. Howe, J. H., and A. J. Isaacson. Preprocedural Imaging for Prostatic Artery Embolization. *Prostatic Artery Embolization* 101–109, 2019.

28. Caine, M., D. Carugo, X. Zhang, M. Hill, M. R. Dreher, and A. L. Lewis. Review of the development of methods for characterization of microspheres for use in embolotherapy: Translating bench to cathlab. *Advanced Healthcare Materials* 6(9):1601291, 2017.

29. Tam, K. Y., K. C.-F. Leung, and Y.-X. J. Wang. Chemoembolization agents for cancer treatment. *European Journal of Pharmaceutical Sciences* 44(1-2):1–10, 2011.

30. Li, M. Progress in research and application of PLGA embolic microspheres. *Frontiers in Bioscience* 21:931–940, 2016.

31. Giunchedi, P., M. Maestri, E. Gavini, P. Dionigi, and G. Rassu. Transarterial chemoembolization of hepatocellular carcinoma – agents and drugs: an overview. Part 2. *Expert Opinion on Drug Delivery* 10(6):799–810, 2013.

32. Giunchedi, P., M. Maestri, E. Gavini, P. Dionigi, and G. Rassu. Transarterial chemoembolization of hepatocellular carcinoma. Agents and drugs: an overview. Part 1. *Expert Opinion on Drug Delivery* 10(5):679–690, 2013.

33. Osuga, K., N. Maeda, H. Higashihara, S. Hori, T. Nakazawa, K. Tanaka, M. Nakamura, K. Kishimoto, Y. Ono, and N. Tomiyama. Current status of embolic agents for liver tumor embolization. *International Journal of Clinical Oncology* 17:306–315, 2012.

34. Lee, K.-H., E. Liapi, J. A. Vossen, M. Buijs, V. P. Ventura, C. Georgiades, K. Hong, I. Kamel, M. S. Torbenson, and J.-F. H. Geschwind. Distribution of Iron Oxide–containing Embosphere Particles after Transcatheter Arterial Embolization in an Animal Model of Liver Cancer: Evaluation with MR Imaging and Implication for Therapy. *Journal of Vascular and Interventional Radiology* 19(10):1490–1496, 2008.

35. Rose, S. C., K. H. Narsinh, and I. G. Newton. Quantification of Blood Pressure Changes in the Vascular Compartment When Using an Anti-Reflux Catheter during Chemoembolization versus Radioembolization: A Retrospective Case Series. *Journal of Vascular and Interventional Radiology* 28(1):103–110, 2017.

36. Choi, J.-Y., J.-M. Lee, and C. B. Sirlin. CT and MR Imaging Diagnosis and Staging of Hepatocellular Carcinoma: Part II. Extracellular Agents, Hepatobiliary Agents, and Ancillary Imaging Features. *Radiology* 273(1):30–50, 2014.

37. Idée, J.-M., and B. Guiu. Use of Lipiodol as a drug-delivery system for transcatheter arterial chemoembolization of hepatocellular carcinoma: A review. *Critical Reviews in Oncology/Hematology* 88(3):530–549, 2013.

38. Garcia, A. C. Larson, and R. A. Omary. Ethiodized Oil Uptake Does Not Predict Doxorubicin Drug Delivery after Chemoembolization in VX2 Liver Tumors. *Journal of Vascular and Interventional Radiology* 23(2):265–273, 2012.

39. Sharma, K. V., M. R. Dreher, Y. Tang, W. Pritchard, O. A. Chiesa, J. Karanian, J. Peregoy, B. Orandi, D. Woods, D. Donahue, J. Esparza, G. Jones, S. L. Willis, A. L. Lewis, and B. J. Wood. Development of “Imageable” Beads for Transcatheter

Embolotherapy. *Journal of Vascular and Interventional Radiology* 21(6):865–876, 2010.

40. Dreher, M. R., K. V. Sharma, D. L. Woods, G. Reddy, Y. Tang, W. F. Pritchard, O. A. Chiesa, J. W. Karanian, J. A. Esparza, D. Donahue, E. B. Levy, S. L. Willis, A. L. Lewis, and B. J. Wood. Radiopaque Drug-Eluting Beads for Transcatheter Embolotherapy: Experimental Study of Drug Penetration and Coverage in Swine. *Journal of Vascular and Interventional Radiology* 23(2):257–264, 2012.

41. Johnson, C. G., Y. Tang, A. Beck, M. R. Dreher, D. L. Woods, A. H. Negussie, D. Donahue, E. B. Levy, S. L. Willis, A. L. Lewis, B. J. Wood, and K. V. Sharma. Preparation of Radiopaque Drug-Eluting Beads for Transcatheter Chemoembolization. *Journal of Vascular and Interventional Radiology* 27(1):117–126, 2016.

42. Duran, R., K. Sharma, M. R. Dreher, K. Ashrafi, S. Mirpour, M. Lin, R. E. Schernthaner, T. R. Schlachter, V. Tacher, A. L. Lewis, S. Willis, M. D. Hartog, A. Radaelli, A. H. Negussie, B. J. Wood, and J.-F. H. Geschwind. A Novel Inherently Radiopaque Bead for Transarterial Embolization to Treat Liver Cancer - A Pre-clinical Study. *Theranostics* 6(1):28–39, 2016.

43. Levy, E. B., V. P. Krishnasamy, A. L. Lewis, S. Willis, C. Macfarlane, V. Anderson, I. M. V. D. Bom, A. Radaelli, M. R. Dreher, K. V. Sharma, A. Negussie, A. S. Mikhail, J.-F. H. Geschwind, and B. J. Wood. First Human Experience with Directly Image-able Iodinated Embolization Microbeads. *CardioVascular and Interventional Radiology* 39(8):1177–1186, 2016.

44. Aliberti, C., R. Carandina, D. Sarti, E. Pizzirani, G. Ramondo, U. Cillo, S. Guadagni, and G. Fiorentini. Transarterial chemoembolization with DC Bead LUMI™ radiopaque beads for primary liver cancer treatment: preliminary experience. *Future Oncology* 13(25):2243–2252, 2017.

45. Thompson, J. G., W. V. D. Sterren, I. Bakhutashvili, I. M. V. D. Bom, A. G. Radaelli, J. W. Karanian, J. Esparza-Trujillo, D. L. Woods, A. L. Lewis, B. J. Wood, and W. F. Pritchard. Distribution and Detection of Radiopaque Beads after Hepatic Transarterial Embolization in Swine: Cone-Beam CT versus MicroCT. *Journal of Vascular and Interventional Radiology* 29(4):568–574, 2018.

46. Jin, B., D. Wang, R. J. Lewandowski, A. Riaz, R. K. Ryu, K. T. Sato, A. C. Larson, R. Salem, and R. A. Omary. Chemoembolization Endpoints: Effect on Survival Among Patients With Hepatocellular Carcinoma. *American Journal of Roentgenology* 196(4):919–928, 2011.

47. Ilhan, H., A. Goritschan, P. Paprottka, T. F. Jakobs, W. P. Fendler, A. Todica, P. Bartenstein, M. Hacker, and A. R. Haug. Predictive Value of 99mTc-MAA SPECT for 90Y-Labeled Resin Microsphere Distribution in Radioembolization of Primary

and Secondary Hepatic Tumors. *Journal of Nuclear Medicine* 56(11):1654–1660, 2015.

48. Wang, D., R. C. Gaba, B. Jin, R. J. Lewandowski, A. Riaz, K. Memon, R. K. Ryu, K. T. Sato, L. M. Kulik, M. F. Mulcahy, A. C. Larson, R. Salem, and R. A. Omary. Perfusion Reduction at Transcatheter Intraarterial Perfusion MR Imaging: A Promising Intraprocedural Biomarker to Predict Transplant-Free Survival during Chemoembolization of Hepatocellular Carcinoma. *Radiology* 272(2):587–597, 2014.

49. Morsbach, F., T. Pfammatter, C. S. Reiner, M. A. Fischer, B.-R. Sah, S. Winklhofer, E. Klotz, T. Frauenfelder, A. Knuth, B. Seifert, N. Schaefer, and H. Alkadhi. Computed Tomographic Perfusion Imaging for the Prediction of Response and Survival to Transarterial Radioembolization of Liver Metastases. *Investigative Radiology* 48(11):787–794, 2013.

50. Reiner, C. S., S. Gordic, G. Puippe, F. Morsbach, M. Wurnig, N. Schaefer, P. Veit-Haibach, T. Pfammatter, and H. Alkadhi. Histogram Analysis of CT Perfusion of Hepatocellular Carcinoma for Predicting Response to Transarterial Radioembolization: Value of Tumor Heterogeneity Assessment. *CardioVascular and Interventional Radiology* 39(3):400–408, 2015.

51. Aravalli, R. N., J. Golzarian, and E. N. K. Cressman. Animal models of cancer in interventional radiology. *European Radiology* 19(5):1049–1053, 2009.

52. Moreira, P. L., and Y. H. An. Animal Models for Therapeutic Embolization. *CardioVascular and Interventional Radiology* 26(2):100–110, 2003.

53. Cressman, E. N. Animal Models in Hepatocellular Carcinoma: Another Step in the Right Direction. *Journal of Vascular and Interventional Radiology* 23(3):395–396, 2012.

54. Acuna, A., A. G. Berman, F. W. Damen, B. A. Meyers, A. R. Adelsperger, K. C. Bayer, M. C. Brindise, B. Bungart, A. M. Kiel, R. A. Morrison, J. C. Muskat, K. M. Wasilczuk, Y. Wen, J. Zhang, P. Zito, and C. J. Goergen. Computational Fluid Dynamics of Vascular Disease in Animal Models. *Journal of Biomechanical Engineering* 140(8):0808011–08080114, 2018.

55. Obeid, M., R. C. Khabbaz, K. D. Garcia, K. M. Schachtschneider, and R. C. Gaba. Translational Animal Models for Liver Cancer. American Journal of Interventional Radiology 2:2, 2018.

56. Sun, F., F. M. Sánchez, V. Crisóstomo, I. Díaz-Güemes, C. López-Sánchez, J. Usón, and M. Maynar. Transarterial Prostatic Embolization: Initial Experience in a Canine Model. *American Journal of Roentgenology* 197(2):495–501, 2011.

57. Heindryckx, F., I. Colle, and H. V. Vlierberghe. Experimental mouse models for hepatocellular carcinoma research. *International Journal of Experimental Pathology* 90(4):367–386, 2009.

58. Parvinian, L., and R. Casadaban. Development, growth, propagation, and angiographic utilization of the rabbit VX2 model of liver cancer: a pictorial primer and "how to" guide. *Journal of Vascular and Interventional Radiology* 20(4):335–340, 2014.

59. Lowder, M. L., S. Li, P. H. Carnell, and R. P. Vito. Correction of distortion of histologic sections of arteries. *Journal of Biomechanics* 40(2):445–450, 2007.

60. Kartasalo, K., L. Latonen, J. Vihinen, T. Visakorpi, M. Nykter, and P. Ruusuvuori. Comparative analysis of tissue reconstruction algorithms for 3D histology. *Bioinformatics* 34(17):3013–3021, 2018.

61. Aharinejad, S. H., and A. Lametschwandtner. Principles and Fundamentals of Microvascular Corrosion Casting for SEM Studies. *Microvascular Corrosion Casting in Scanning Electron Microscopy* pp:12–43, 1992.doi:10.1007/978-3-7091-9230-6_2

62. Folarin, A., M. Konerding, J. Timonen, S. Nagl, and R. Pedley. Three-dimensional analysis of tumour vascular corrosion casts using stereoimaging and micro-computed tomography. *Microvascular Research* 80(1):89–98, 2010.

63. Ackermann, M., and M. A. Konerding. Vascular Casting for the Study of Vascular Morphogenesis. *Methods in Molecular Biology Vascular Morphogenesis* 1214:49–66, 2015.doi:10.1007/978-1-4939-1462-3_5

64. Allen, J., and K. Howell. Microvascular imaging: techniques and opportunities for clinical physiological measurements. *Physiological Measurement* 35(7): R91–R141, 2014.

65. Lal, C., and M. J. Leahy. An Updated Review of Methods and Advancements in Microvascular Blood Flow Imaging. *Microcirculation* 23(5):345–363, 2016.

66. Jorgensen, S. M., O. Demirkaya, and E. L. Ritman. Three-dimensional imaging of vasculature and parenchyma in intact rodent organs with X-ray micro-CT. *American Journal of Physiology-Heart and Circulatory Physiology* 275(3):H1103–H1114, 1998.

67. Mondy, W. L., D. Cameron, J.-P. Timmermans, N. D. Clerck, A. Sasov, C. Casteleyn, and L. A. Piegl. Micro-CT of Corrosion Casts for Use in the Computer-Aided Design of Microvasculature. *Tissue Engineering Part C: Methods* 15(4):729–738, 2009.

68. Zagorchev, L., P. Oses, Z. Zhuang, K. Moodie, M. J. Mulligan-Kehoe, M. Simons, and T. Couffinhal, Micro computed tomography for vascular exploration. *Journal of Angiogenesis Research* 2(7):1–11, 2010.

69. Kline, T. L., and E. L. Ritman. Studying Microcirculation with Micro-CT. *Microcirculation Imaging* 313–347, 2012.

70. Downey, C. M., A. K. Singla, M. L. Villemaire, H. R. Buie, S. K. Boyd, and F. R. Jirik. Quantitative Ex-Vivo Micro-Computed Tomographic Imaging of Blood Vessels and Necrotic Regions within Tumors. *PLoS ONE* 7(7):e41685, 2012.

71. Orhan, K. *Micro-Computed Tomography (micro-CT) in Medicine and Engineering*. Cham, Switzerland: Springer, 2020.

72. Eipel, C., K. Abshagen, and B. Vollmar. Regulation of hepatic blood flow: The hepatic arterial buffer response revisited. *World Journal of Gastroenterology* 16(48):6046–6057, 2010.

73. Lautt, W., D. J. Legare, and W. R. Ezzat. Quantitation of the hepatic arterial buffer response to graded changes in portal blood flow. *Gastroenterology* 98(4):1024–1028, 1990.

74. Hennedige, T., and S. K. Venkatesh. Imaging of hepatocellular carcinoma: diagnosis, staging and treatment monitoring. *Cancer Imaging* 12(3):530–547, 2012.

75. López-Benítez, R., G. M. Richter, H.-U. Kauczor, S. Stampfl, J. Kladeck, B. A. Radeleff, M. Neukamm, and P. J. Hallscheidt. Analysis of Nontarget Embolization Mechanisms During Embolization and Chemoembolization Procedures. *CardioVascular and Interventional Radiology* 32:615–622, 2009.

76. Ingraham, C., G. Johnson, A. Nair, and S. Padia. Nontarget Embolization Complicating Transarterial Chemoembolization in a Patient with Hepatocellular Carcinoma. *Seminars in Interventional Radiology* 28(2):202–206, 2011.

77. Basciano, C. A., C. Kleinstreuer, A. S. Kennedy, W. A. Dezarn, and E. Childress. Computer Modeling of Controlled Microsphere Release and Targeting in a Representative Hepatic Artery System. *Annals of Biomedical Engineering* 38(5):1862–1879, 2010.

78. Basciano, C. A., C. Kleinstreuer, and A. S. Kennedy. Computational Fluid Dynamics Modeling of 90Y Microspheres in Human Hepatic Tumors. *Journal of Nuclear Medicine & Radiation Therapy* 2:112, 2011.

79. Kleinstreuer, C., C. A. Basciano, E. M. Childress, and A. S. Kennedy. A New Catheter for Tumor Targeting With Radioactive Microspheres in Representative Hepatic Artery Systems. Part I: Impact of Catheter Presence on Local Blood Flow

and Microsphere Delivery. *Journal of Biomechanical Engineering* 134(5):051004, 2012.

80. Childress, E. M., C. Kleinstreuer, and A. S. Kennedy. A New Catheter for Tumor-Targeting With Radioactive Microspheres in Representative Hepatic Artery Systems—Part II: Solid Tumor-Targeting in a Patient-Inspired Hepatic Artery System. *Journal of Biomechanical Engineering* 134(5):051005, 2012.

81. Childress, E. M., and C. Kleinstreuer. Computationally Efficient Particle Release Map Determination for Direct Tumor-Targeting in a Representative Hepatic Artery System. *Journal of Biomechanical Engineering* 136(1):011012, 2013.

82. Childress, E. M., and C. Kleinstreuer. Impact of Fluid–Structure Interaction on Direct Tumor-Targeting in a Representative Hepatic Artery System. *Annals of Biomedical Engineering* 42(3):461–474, 2013.

83. Zhu, S. J., E. K. W. Poon, A. S. H. Ooi, and S. Moore. Enhanced Targeted Drug Delivery Through Controlled Release in a Three-Dimensional Vascular Tree. *Journal of Biomechanical Engineering* 137(3): 2015.

84. Aramburu, J., R. Antón, A. Rivas, J. C. Ramos, B. Sangro, and J. I. Bilbao. Numerical investigation of liver radioembolization via computational particle–hemodynamics: The role of the microcatheter distal direction and microsphere injection point and velocity. *Journal of Biomechanics* 49(15):3714–3721, 2016.

85. Aramburu, J., R. Antón, A. Rivas, J. C. Ramos, B. Sangro, and J. I. Bilbao. Computational particle-haemodynamics analysis of liver radioembolization pretreatment as an actual treatment surrogate. *International Journal for Numerical Methods in Biomedical Engineering* 33(2): 2017. doi:10.1002/cnm.2791

86. Simoncini, C., K. Jurczuk, D. Reska, S. Esneault, J.-C. Nunes, J.-J. Bellanger, H. Saint-Jalmes, Y. Rolland, P.-A. Eliat, J. Bézy-Wendling, and M. Kretowski. Towards a patient-specific hepatic arterial modeling for microspheres distribution optimization in SIRT protocol. *Medical & Biological Engineering & Computing* 56(3):515–529, 2017.

87. Caine, M., M. S. Mccafferty, S. Mcghee, P. Garcia, W. M. Mullett, X. Zhang, M. Hill, M. R. Dreher, and A. L. Lewis. Impact of Yttrium-90 Microsphere Density, Flow Dynamics, and Administration Technique on Spatial Distribution: Analysis Using an In Vitro Model. *Journal of Vascular and Interventional Radiology* 28(2): 260–268, 2017.

88. Aramburu, J., R. Antón, A. Rivas, J. C. Ramos, B. Sangro, and J. I. Bilbao. Computational assessment of the effects of the catheter type on particle–hemodynamics during liver radioembolization. *Journal of Biomechanics* 49(15):3705–3713, 2016.

89. Xu, Z., S. Jernigan, C. Kleinstreuer, and G. D. Buckner. Solid Tumor Embolotherapy in Hepatic Arteries with an Anti-reflux Catheter System. *Annals of Biomedical Engineering* 44(4):1036–1046, 2015.

90. Aramburu, J., R. Antón, A. Rivas, J. C. Ramos, G. S. Larraona, B. Sangro, and J. I. Bilbao. A methodology for numerically analysing the hepatic artery haemodynamics during B-TACE: a proof of concept. *Computer Methods in Biomechanics and Biomedical Engineering* 22(5):518–532, 2019.

91. Aramburu, J., R. Antón, A. Rivas, J. C. Ramos, B. Sangro, and J. I. Bilbao. The role of angled-tip microcatheter and microsphere injection velocity in liver radioembolization: A computational particle-hemodynamics study. *International Journal for Numerical Methods in Biomedical Engineering* 33(12): 2017.

92. Debbaut, C., D. Monbaliu, C. Casteleyn, P. Cornillie, D. V. Loo, B. Masschaele, J. Pirenne, P. Simoens, L. V. Hoorebeke, and P. Segers. From Vascular Corrosion Cast to Electrical Analog Model for the Study of Human Liver Hemodynamics and Perfusion. *IEEE Transactions on Biomedical Engineering* 58(1):25–35, 2011.

93. Debbaut, C., P. Segers, P. Cornillie, C. Casteleyn, M. Dierick, W. Laleman, and D. Monbaliu. Analyzing the human liver vascular architecture by combining vascular corrosion casting and micro-CT scanning: a feasibility study. *Journal of Anatomy* 224(4):509–517, 2014.

94. Hendee, W. R., and E. R. Ritenour. *Medical Imaging Physics*. Hoboken: Wiley, 2003.

95. Cohen, L., and R. Kimmel. Global minimum for active contour models: a minimal path approach. *International Journal of Computer Vision* 24:57–78, 1997.

96. Deschamps, T., and L. D. Cohen. Fast extraction of minimal paths in 3D images and applications to virtual endoscopy. *Medical Image Analysis* 5(4):281–299, 2001

97. Wijngaard, J. P. V. D., J. C. Schwarz, P. V. Horssen, M. G. V. Lier, J. G. Dobbe, J. A. Spaan, and M. Siebes. 3D Imaging of vascular networks for biophysical modeling of perfusion distribution within the heart. *Journal of Biomechanics* 46(2):229–239, 2013.

98. Marxen, M., J. G. Sled, L. X. Yu, C. Paget, and R. M. Henkelman. Comparing microsphere deposition and flow modeling in 3D vascular trees. *American Journal of Physiology-Heart and Circulatory Physiology* 291(5):H2136–H2141, 2006.

99. Aharinejad, S., W. Schreiner, and F. Neumann. Morphometry of human coronary arterial trees. *The Anatomical Record* 251(1):50–59, 1998.

100. Mittal, N., Y. Zhou, S. Ung, C. Linares, S. Molloi, and G. S. Kassab. A Computer Reconstruction of the Entire Coronary Arterial Tree Based on Detailed Morphometric Data. *Annals of Biomedical Engineering* 33(8):1015–1026, 2005.

101. Wischgoll, T., J. S. Choy, E. L. Ritman, and G. S. Kassab. Validation of Image-Based Method for Extraction of Coronary Morphometry. *Annals of Biomedical Engineering* 36(3):356–368, 2008.

102. Wischgoll, T., J. S. Choy, and G. S. Kassab. Extraction of morphometry and branching angles of porcine coronary arterial tree from CT images. *American Journal of Physiology-Heart and Circulatory Physiology* 297(5):H1949–H1955, 2009.

103. Buijs, J. O. D., Ž. Bajzer, and E. L. Ritman. Branching Morphology of the Rat Hepatic Portal Vein Tree: A Micro-CT Study. *Annals of Biomedical Engineering* 34(9):1420–1428, 2006.

104. Nordsletten, D. A., S. Blackett, M. D. Bentley, E. L. Ritman, and N. P. Smith. Structural morphology of renal vasculature. *American Journal of Physiology-Heart and Circulatory Physiology* 291(1):H296–H309, 2006.

105. Ganesan, P., S. He, and H. Xu. Development of an Image-Based Network Model of Retinal Vasculature. *Annals of Biomedical Engineering* 38(4):1566–1585, 2010.

106. Yang, J., L. X. Yu, M. Y. Rennie, J. G. Sled, and R. M. Henkelman. Comparative structural and hemodynamic analysis of vascular trees. *American Journal of Physiology-Heart and Circulatory Physiology* 298(4):H1249–H1259, 2010.

107. Beard, D. A., and J. B. Bassingthwaighte. The Fractal Nature of Myocardial Blood Flow Emerges from a Whole-Organ Model of Arterial Network. *Journal of Vascular Research* 37(4):282–296, 2000.

108. Zhao, F., Y. Chen, Y. Hou, and X. He. Segmentation of blood vessels using rule-based and machine-learning-based methods: a review. *Multimedia Systems* 25:109–118, 2017.

109. Lesage, D., E. D. Angelini, I. Bloch, and G. Funka-Lea. A review of 3D vessel lumen segmentation techniques: Models, features and extraction schemes. *Medical Image Analysis* 13(6):819–845, 2009.

110. Qureshi, K. A Systematic Survey and Evaluation of Blood Vessel Extraction Techniques. *International Journal of Medical Imaging* 5:63–69, 2017.

111. Moccia, S., E. D. Momi, S. E. Hadji, and L. S. Mattos. Blood vessel segmentation algorithms — Review of methods, datasets and evaluation metrics. *Computer Methods and Programs in Biomedicine* 158:71–91, 2018.

112. Kirbas, C., and F. Quek. A review of vessel extraction techniques and algorithms. *ACM Computing Surveys (CSUR)* 36(2):81–121, 2004.

113. Wan, S.-Y., E. L. Ritman, and W. E. Higgins. Multi-generational analysis and visualization of the vascular tree in 3D micro-CT images. *Computers in Biology and Medicine* 32(2):55–71, 2002.

114. Giachetti, A., and G. Zanetti. Vascular Modeling from Volumetric Diagnostic Data: A Review. *Current Medical Imaging Reviews* 2(4):415–423, 2006.

115. Yu, K.-C., E. L. Ritman, and W. E. Higgins. System for the analysis and visualization of large 3D anatomical trees. *Computers in Biology and Medicine* 37(12):1802–1820, 2007.

116. Merkx, M. A., J. O. Bescós, L. Geerts, E. M. H. Bosboom, F. N. V. D. Vosse, and M. Breeuwer. Accuracy and precision of vessel area assessment: Manual versus automatic lumen delineation based on full-width at half-maximum. *Journal of Magnetic Resonance Imaging* 36(5):1186–1193, 2012.

117. Marxen, M., M. M. Thornton, C. B. Chiarot, G. Klement, J. Koprivnikar, J. G. Sled, and R. M. Henkelman. MicroCT scanner performance and considerations for vascular specimen imaging. *Medical Physics* 31(2):305–313, 2004.

118. Matl, S., R. Brosig, M. Baust, N. Navab, and S. Demirci. Vascular image registration techniques: A living review. *Medical Image Analysis* 35:1–17, 2017.

119. Kline, T. L., M. Zamir, and E. L. Ritman. Accuracy of Microvascular Measurements Obtained From Micro-CT Images. *Annals of Biomedical Engineering* 38(9):2851–2864, 2010.

120. Giavarina, D. Understanding Bland Altman analysis. *Biochemia Medica* 25(2):141–151, 2015.

121. Stock, S. R. *Microcomputed tomography: methodology and applications*. Boca Raton, FL: CRC Press/Taylor and Francis, 2020.

122. Hoffmann, K. R., D. P. Nazareth, L. Miskolczi, A. Gopal, Z. Wang, S. Rudin, and D. R. Bednarek. Vessel size measurements in angiograms: A comparison of techniques. *Medical Physics* 29(7):1622–1633, 2002.

123. Ngo, J. P., B. Le, Z. Khan, M. M. Kett, B. S. Gardiner, D. W. Smith, M. M. Melhem, A. Maksimenko, J. T. Pearson, and R. G. Evans. Micro-computed tomographic analysis of the radial geometry of intrarenal artery-vein pairs in rats and rabbits: Comparison with light microscopy. *Clinical and Experimental Pharmacology and Physiology* 44(12):1241–1253, 2017.

124. Clark, D., and C. Badea. Micro-CT of rodents: State-of-the-art and future perspectives. *Physica Medica* 30(6):619–634, 2014.

125. Peters, J., L. Vest, M. Schuelke, S. P. Zustiak, A. F. Hall, and S. Mcbride‐Gagyi. MicroCT vascular network analysis program: Development, validation, and comparison to manufacturer software. *Journal of Orthopaedic Research* 38(6):1340–1350, 2019.

126. Assa, J. Differential Patterns of Vasculature to Liver Tumours. *British Journal of Cancer* 24:360–363, 1970.

127. Archer, S. G., and B. N. Gray. Vascularization of small liver metastases. *British Journal of Surgery* 76(6):545–548, 1989.

128. Wu, H., A. A. Exner, H. Shi, J. Bear, and J. R. Haaga. Dynamic Evolutionary Changes in Blood Flow Measured by MDCT in a Hepatic VX2 Tumor Implant over an Extended 28-day Growth Period: Time-Density Curve Analysis. *Academic Radiology* 16(12):1483–1492, 2009.

129. Qi, X.-L., J. Liu, P. N. Burns, and G. A. Wright. The Characteristics of Vascular Growth in VX2 Tumor Measured by MRI and Micro-CT. *Journal of Oncology* 2012:1–7, 2012.

130. Zhang, Q., R. Eagleson, and T. M. Peters. Volume Visualization: A Technical Overview with a Focus on Medical Applications. *Journal of Digital Imaging* 24():640–664, 2010.

131. Duran, A. H., M. N. Duran, I. Masood, L. M. Maciolek, and H. Hussain. The Additional Diagnostic Value of the Three-dimensional Volume Rendering Imaging in Routine Radiology Practice. *Cureus* 11(9):e5579, 2019

132. Rous, P., and J. W. Beard. The Progression To Carcinoma Of Virus-Induced Rabbit Papillomas (Shope). *The Journal of Experimental Medicine* 62(4):523–548, 1935.

133. Kidd, J. G., and P. Rous. A Transplantable Rabbit Carcinoma Originating In A Virus-Induced Papilloma And Containing The Virus In Masked Or Altered Form. *The Journal of Experimental Medicine* 71(6):813–838, 1940.

134. Rhee, T. K., R. K. Ryu, A. K. Bangash, D. Wang, B. Szolc-Kowalska, K. R. Harris, K. T. Sato, H. B. Chrisman, R. L. Vogelzang, T. Paunesku, G. E. Woloschak, A. C. Larson, and R. A. Omary. Rabbit VX2 Tumors as an Animal Model of Uterine Fibroids and for Uterine Artery Embolization. *Journal of Vascular and Interventional Radiology* 18(3):411–418, 2007.

135. Wang, D., A. K. Bangash, T. K. Rhee, G. E. Woloschak, T. Paunesku, R. Salem, R. A. Omary, and A. C. Larson. Liver Tumors: Monitoring Embolization in Rabbits

with VX2 Tumors—Transcatheter Intraarterial First-Pass Perfusion MR Imaging. *Radiology* 245(1):130–139, 2007.

136. Virmani, S., D. Wang, K. R. Harris, R. K. Ryu, K. T. Sato, R. J. Lewandowski, A. A. Nemcek, B. Szolc-Kowalska, G. Woloschak, R. Salem, A. C. Larson, and R. A. Omary. Comparison of Transcatheter Intraarterial Perfusion MR Imaging and Fluorescent Microsphere Perfusion Measurements during Transcatheter Arterial Embolization of Rabbit Liver Tumors. *Journal of Vascular and Interventional Radiology* 18(10):1280–1286, 2007.

137. Tacher, V., R. Duran, M. Lin, J. H. Sohn, K. V. Sharma, Z. Wang, J. Chapiro, C. G. Johnson, N. Bhagat, M. R. Dreher, D. Schäfer, D. L. Woods, A. L. Lewis, Y. Tang, M. Grass, B. J. Wood, and J.-F. Geschwind. Multimodality Imaging of Ethiodized Oil–loaded Radiopaque Microspheres during Transarterial Embolization of Rabbits with VX2 Liver Tumors. *Radiology* 279(3):741–753, 2016.

138. Maehara, N. Experimental microcomputed tomography study of the 3D microangioarchitecture of tumors. *European Radiology* 13(7):1559–1565, 2002.

139. Kim, E., S. Stamatelos, J. Cebulla, Z. M. Bhujwalla, A. S. Popel, and A. P. Pathak. Multiscale Imaging and Computational Modeling of Blood Flow in the Tumor Vasculature. *Annals of Biomedical Engineering* 40(11):2425–2441, 2012.

140. Gonda, T., H. Ishida, K. Yoshinaga, and K. Sugihara. Microvasculature of Small Liver Metastases in Rats. *Journal of Surgical Research* 94(1):43–48, 2000.

141. Nagy, J. A., S.-H. Chang, A. M. Dvorak, and H. F. Dvorak. Why are tumour blood vessels abnormal and why is it important to know? *British Journal of Cancer* 100(6):865–869, 2009.

142. Reitan, N. K., M. Thuen, Goa Pål Erik, and C. D. L. Davies. Characterization of tumor microvascular structure and permeability: comparison between magnetic resonance imaging and intravital confocal imaging. *Journal of Biomedical Optics* 15(3):036004, 2010.

143. Peterson, H.-I. *Tumor blood circulation: angiogenesis, vascular morphology, and blood flow of experimental and human tumors*. Boca Raton: CRC Press, 2019.

144. Anderson, J., W. Angerson, N. Willmott, D. Kerr, C. Mcardle, and T. Cooke. Is there a relationship between regional microsphere distribution and hepatic arterial blood flow? *British Journal of Cancer* 66(2):287–289, 1992.

145. M. Muller, S. Schirm, and M, Teschner, “Interactive blood simulation for virtual surgery based on smoothed particle hydrodynamics”, *Technology and Health Care*, 12(1):25–31, 2004.

146. S. Kulp, M. Gao, S. Zhang, Z. Qian, S. Voros, D. Metaxas and L. Axel, “Practical patient-specific cardiac blood flow simulations using SPH*”, IEEE 10th International Symposium on Biomedical Imaging: From Nano to Macro*, 2013.

147. Caballero, A., W. Mao, L. Liang, J. Oshinski, C. Primiano, R. Mckay, S. Kodali, and W. Sun. Modeling Left Ventricular Blood Flow Using Smoothed Particle Hydrodynamics. *Cardiovascular Engineering and Technology* 8(4):465–479, 2017.

148. Schroeder, W., K. Martin, B. Lorensen, L. S. Avila, R. Avila, and C. C. Law. *The visualization toolkit an object-oriented approach to 3D graphics*. Upper Saddle River, NJ: Pearson Education, Inc, 2006.

149. Liu, M. B., and G. R. Liu. Smoothed Particle Hydrodynamics (SPH): An overview and recent developments. *Archives of Computational Methods in Engineering* 17:25–76, 2010.

150. Jan Bender and Dan Koschier, Divergence-Free Smoothed Particle Hydrodynamics, In *Proceedings of ACM SIGGRAPH / EUROGRAPHICS Symposium on Computer Animation (SCA)*, 147–155, 2015

151. Li, D., Fluid Particles, 2016 at https://david.li/fluid/

152. M. Muller, D. Charypar, and M. Gross, “Particle-based fluid simulation for interactive applications”, *in Proceedings of Eurographics/SIGGRAPH Symposium on Computer Animation*, 2003.

Appendix A, B, and C are the protocols from Dr. Gupta's lab at MD Anderson Cancer Center.

APPENDIX A PREPARATION OF TUMOR FOR FROZEN STORAGE

Procedure - Preparation of Tumor for Frozen Storage

1. Spray gloves with 70% alcohol and wipe dry.
2. Turn on the outlet and light on hood. Spray the surface with the 70% alcohol and wipe dry with gauze.
3. Refer to ATB 1015 to prepare tumor for freezing. Tumor that has not been homogenized may be frozen. Note: Freeze back a minimum of 2 vials.
4. Prepare fresh freeze media and keep cold.
5. Prelabel the Nunc vials with the Tank #, Cannula #, tube letter and number. Add animal number, tumor type, date, and investigator's name. Example: T6, C2, A1, 97L102, VX2, 8/19/97, Wright.
6. Using a cell scraper, place the minced tumor (approximately a pea sized amount) into the appropriate number of 2 ml Nunc vials.
7. Pipet Freeze Media onto the tissue up to the 1.8 ml line.
8. Cap, mix, and place in Nalgene cryo freezing container.
9. Place in the -80˚C freezer for a minimum of 4 hours.
10. Label the cane with the tube letter.
11. Remove vials from freezer and place in a cane (5vials/cane).
12. Place the cane in the appropriate cannula in the liquid nitrogen tank.
13. Enter the date frozen, primary species, tumor ID #, tumor type, PCS, number of vials frozen, tank, cannula, tube letter and number for freezer location, Investigator, and Department in the TUMOR BANK file. To access the Tumor Bank file, click on the Departmental Network drive, PATH LABS, Clinical Pathology. Save to flash drive.
14. Place all tubes, cell scrapers, and serological pipettes in the red sharps container under the hood.

APPENDIX B PREPARATION OF TUMOR INOCULATION FROM FROZEN STOCK

Procedure - Preparation of the Inoculation

1. Spray gloves with 70% alcohol.
2. Turn on light and outlet on hood. Spray surface with 70% alcohol and wipe dry with gauze.
3. Place two all purpose wipers on working surface under hood.
4. Spray the tray and rack with 70% alcohol and wipe dry. Set the rack in the tray. Fill with ice from the ice machine located in TB.4041. Set the tray on the all purpose wiper under hood.
5. Label and add 10 ml D-MEM/F-12 with 10% FBS to a 50 ml conical tube. Then add 0.05 ml Gentamicin using a 21 gauge needle on a 1 ml syringe. Label with the animal #. Keep cold. Note: For every 4 vials thawed, use one 50 ml conical tube.
6. Label and fill a 50 ml conical tube with 40 mls 70% alcohol. Set in the rack under the hood. Place the homogenizer probe in the 50 ml tube containing 70% alcohol.
7. Label and add D-MEM/F-12 with 10% FBS to a sterile 12 x 75 mm tube. Keep cold.
8. Label and fill a 50 ml conical tube with 40 mls PBS. Set in rack under the hood.
9. Remove 18 gauge needles, syringes, and 12 x 75 mm tubes from their packaging. Place on the all purpose wiper under the hood. Place the cell scrapers and pipettor under the hood.
10. Set appropriate number of 12 x 75 mm tubes in the rack in the iced tray. Note: 2-3 tubes equal one needle.
11. Remove the appropriate vials from storage in the liquid nitrogen tanks.
12. Place the vials in the 37˚C dry bath to thaw. It will take around 5 minutes.
13. Spray outside of the vial with alcohol and place under the hood.
14. Transfer vial contents to the tube with D-MEM/F-12.

15. Centrifuge at 1000 rpm for 5 minutes.
16. After the spin is complete, place the conical tube under the hood. Shake out a 9 inch pipet and aspirate the supernatant using the vacuum knob on the hood.
17. Using a cell scraper, transfer tumor about the size of a pea into each of the 12 x 75 mm plastic tubes.
18. Add 150 μl D-MEM/F-12 with 10% FBS to each tube.
19. After the homogenizer probe has been soaked in the 50 ml tube containing 70% alcohol, connect the generator to the homogenizer probe. Rinse the homogenizer probe in 50 ml PBS tube for approximately 10 seconds.
20. Place the homogenizer probe into a 12 x 75 mm tube. Toggle to the ON position. Homogenize once for 1 second.
21. Rinse homogenizer probe in the 50 ml PBS tube before proceeding to the next tube. When finished pulsing, soak the homogenizer probe in the tube with alcohol.
22. Pull the tissue mix into a 1 ml syringe with an 18 gauge needle. Work out the air bubbles. Go from tube to tube until the syringe has 0.5 ml (or whatever amount the investigator requests) of tumor.
23. Place a clean 18 gauge needle on the syringe. Wipe syringe with gauze soaked with 70% alcohol. Label the syringe with the animal number and date.
24. Place the syringes in a bucket of ice until all syringes have been made and labeled. Place the bucket in the refrigerator and notify the investigator or appropriate personnel the syringes are ready for inoculation.
25. Place all needles, tubes, cell scrapers, pipet tips, vials and serological pipets in the red sharps container under the hood.
26. Disassemble the homogenizer probe. Rinse the parts in soapy water. Forcefully, dry with a stream of air until dry.
27. Reassemble the homogenizer probe. Place in an autoclave pouch. Autoclave on Wrapped goods cycle.
28. Place the autoclaved homogenizer probe in the top drawer in the hood room.

29. Update the TUMOR BANK file. To access the Tumor Bank, click on the Departmental Network drive, Veterinary Pathology, PATH LABS, Clinical Pathology folder to reflect the vials removed from liquid nitrogen storage. Save to flash drive.

APPENDIX C PREPARATION OF TUMOR INOCULATION

Procedure - Tumor Inoculation Procedure

2. Spray gloves with 70% alcohol and wipe dry.
3. Turn on the outlet and light on hood. Spray the surface with the 70% alcohol and wipe dry.
4. Fill the ice bucket with ice from ice machine located in TB.4041 if the investigator has not provided one.
5. Label and fill one 50 ml conical tube with 40 mls of 70% alcohol per animal. Set in the rack under the hood. Place a homogenizer probe in each tube.
6. Label and fill one 50 ml conical tube with 40 mls PBS per animal. Place in the rack under the hood.
7. Label and add 10 mls D-MEM/F-12 with 10% FBS into one 50 ml conical tube per animal. Then add 0.05 ml Gentamicin using a 21 gauge needle and 1 ml syringe. Label each tube with the animal number. Also, add D-MEM/F-12 with 10% FBS to a sterile 12 x 75 mm tube. Keep cold.
8. Remove the 18 gauge needles and syringes from their packaging. Place them on an all purpose wiper under the hood. Place the cell scrapers, Petri dishes, pipettor, and scalpels under the hood.
9. Place an all purpose wiper on the working surface area of the hood. Spray the tray and rack with 70% alcohol and wipe dry.
10. Place the rack in tray and fill with ice. Set the tray on an all purpose wiper. Place a sterile 4 inch x 4 inch gauze on rack to stabilize Petri dish.
11. Wipe the outside of the tumor specimen container with 70% alcohol and wipe to dry.
12. Place a sterile Petri dish in the center of the tray with rack. Place the tumor from the container into the Petri dish.

13. Clean up the tumor using two #21 scalpels. Remove fat, connective tissue, and muscle. Cut open tumor and remove any necrotic material. Place all debris into the tumor container cup.
14. Note: If requested by an Investigator or designated personnel, cut the appropriate size tumor chunks for inoculation. Place in a sterile container with enough D-MEM/F-12 with 10% FBS to cover the chunks. Place on ice.
15. Mince the remaining tumor with the scalpels using the cross-knife technique. Add the minced tumor to the D-MEM/F-12/Gentamicin conical tube.
16. Pour Lysol solution into the Petri dish and set aside.
17. Spin the tube for 5 minutes at 1000 rpm.
18. Place appropriate number of 12 x 75 mm tubes in the ice rack. NOTE: 2-3 tubes equal one needle.
19. After the spin is complete, place the conical tube under the hood. Shake out a 9 inch sterile Pasteur pipet and aspirate the supernatant.
20. Using a cell scraper, scrape tumor (about the size of a pea) into each of the 12 x 75 mm tubes.
21. Add 150 μl D-MEM/F-12 with 10% FBS to each tube.
22. Connect the generator to the homogenizer probe. Use the homogenizer probe to further mince the tissue.
23. Rinse the homogenizer probe in 50 ml PBS tube for approximately 10 seconds.
24. Place the homogenizer probe into a 12 x 75 mm tube. Toggle to the ON position. Homogenize once for one second. This should produce a cream-of-wheat appearance with some chunks still present.
25. Rinse the homogenizer probe in the 50 ml PBS tube before proceeding to the next tube.
26. Pull the homogenized tissue mix into a 1 ml syringe with an 18 gauge needle. Work out the air bubbles. Go from tube to tube until the syringe has the desired amount of tumor per needle (usually 0.5 ml).
27. Place a clean 18 gauge needle on the syringe. Wipe syringe with gauze soaked with 70% alcohol. Label the syringe with the rabbit number and date.

28. Place the syringe in the ice bucket until all syringes have been made. Place the bucket in the refrigerator.
29. Notify the researcher or appropriate personnel that their inoculums are ready for pick-up.
30. If all the tissue was not used to make the needles, ask the investigator if the remaining tissue should be frozen back. If the tissue is to be frozen, refer to the ATB 1017 procedure. Note: Tumor must be in chunks and not homogenized in order to be frozen back.
31. Place all specimen containers, tubes, needles, scalpels, cell scrapers, pipet tips, and serological pipets in the red sharps container under the hood.
32. Wash and clean the Petri dish in soapy water containing detergent and rinse with tap water. Place in the dishwasher. After the dishwashing is complete, wrap the petri dish with blue sterilization wrap and secure with autoclave tape.
33. Disassemble the homogenizer probe. Clean the parts in soapy water and rinse with tap water. Blot dry. Dry with a stream of air until dry.
34. Reassemble the homogenizer probe. Place in an autoclave pouch.
35. Autoclave the petri dish and homogenizer probe on the Wrapped Goods cycle.
36. Place the autoclaved homogenizer probe in the top drawer and the petri dish in the cabinet in the hood room.